UNIVERSITY OF NOVA GORICA
GRADUATE SCHOOL

COMBINED TLS AND MICROFLUIDIC-FIA DEVICES FOR HIGHLY SENSITIVE AND RAPID ENVIRONMENTAL ANALYSIS

DISSERTATION

Mingqiang Liu

Mentor: prof.dr. Mladen Franko

Nova Gorica, 2013

To my

     Mom Changgui Wang
             &
     Dad   Taijiang Liu

ACKNOWLEDGEMENTS

POVZETEK

V minulih letih je zaradi velike potrebe in potrošnje velikih količin hrane, zdravil in farmacevtskih izdelkov ter pesticidov v svetu nastalo veliko odpadkov in strupenih snovi. Nekatere snovi lahko v postopkih proizvodnje, uporabe ali odlaganja odpadkov pridejo direktno v okolje in predstavljajo veliko nevarnost za zdravje ljudi in okolje samo. Med take spadajo tako različna fitofarmacevtska sredstva, težke kovine in farmacevtske učinkovine, kot tudi različni alergeni in toksini.

Za kvantitativno ugotavljanje njihove prisotnosti v okolju, so bile razvite in uporabljene različne analizne tehnike, od splošno uveljavljenih kromatografskih in spektroskopskih tehnik, do bioanaliznih senzorjev in testov ter njihovih kombinacij oziroma tako imenovanih sklopljenih tehnik. V slednjih je bila za detekcijo analitov velikokrat uporabljena tudi spektrometrija s toplotnimi lečami (TLS), predvsem zaradi njene zelo visoke občutljivosti in hitre odzivnosti. Mejnik v nadaljnem razvoju TLS je bila uvedba mikroskopije s toplotnimi lečami (TLM). S tem je TLS postala uporabna za analize mikroskopskih vzorcev, kot je to primer v mikrofluidnih sistemih in kemijskih mikročipih. Številne raziskave so pomembno prispevale k boljši občutljivosti in specifičnosti TLS in TLM, kljub temu pa TLS na splošno še ni dosegla primerne stopnje razvoja in uporabnosti za rutinske kemijske analize. To lahko pripišemo dvem glavnim razlogom. Prvi je skupen vsem TLS metodam in je povezan z razpoložljivostjo primernih svetlobnih izvorov za TLS, ki zahteva Gaussovo radialno porazdelitev intenzitete vzbujevalne svetlobe, ki jo lahko zagotavljajo le laserji. Slednji pa so pogosto omejeni le na eno samo valovno dolžino ali v najboljšem primeru na zelo ozko spektralno območje emitirane svetlobe. To močno omejuje specifičnost tehnike TLS in posledično njeno uporabnost v praktični kemijski analizi. Drugi razlog je vezan izključno na TLM pri kateri analiza signala toplotne leče še vedno temelji na klasični teoriji TLS za makroskopske vzorce, ki neustrezno upošteva vpliv debeline vzorca in njegove okolice na velikost signala. Prav tem razlogom in odpravljanju njihovih posledic za TLS so posvečene raziskave predstavljene v tej disertaciji, s ciljem dodatnega razvoja te tehnike, ki bi omogočil širšo uporavnost TLS v kemijski analizi.

Za boljši pregled nad stopnjo razvoja tehnike TLS in razumevanje samega pojava toplotne leče, so v drugem poglavju podane teoretične osnove TLS in obsežen pregled aplikacij TLS v kombinaciji z različnimi separacijskimi tehnikami, biosenzorji, pretočno injekcijsko analizo FIA in mikrofluidnimi sistemi za detekcijo toksičnih in bioaktivnih snovi v okoljskih vzorcih.

Kot visoko občutljiva metoda, ki omogoča zaznavanje absorbanc velikosti 10^{-7}, je spektrometrija TLS v uporabi v kemijski analizi že preko 30 let. Del njenega razvoja je povezan z različnimi teoretičnimi modeli, ki so omogočili opisovanje in razumevanje pojava toplotne leče. Osnova različnih teoretičnih modelov TLS je lahko enostavna parabolična aproksimacija ali pa bolj kompleksna Fresnelova difrakcija. Razviti so bili za opisovanje signala toplotne leče tako v statičnih kot tudi v pretočnih vzorcih. Vzporedno z razvojem teorije je tekel tudi razvoj instrumentov za meritve v spektrometriji TLS. Ti so se razvijali preko prvotno enostavnih enožarkovnih instrumentov, do dvožarkovnih vzbujevalno-tipalnih spektrometrov TLS, pri katerih so za vzbujanje uporabljeni laserji ali tudi nekoherentni svetlobni viri. Kompleksnejši instrumenti vključujejo diferenčne in fazno konjugirane spektrometre TLS ter nenazadnje tudi TLM mikroskope s toplotnimi lečami.

Pregled praktičnih aplikacij TLS je usmerjen predvsem v kemijsko analizo s TLS v povezavi s separacijskimi tehnikami, kot sta tekočinska kromatografija visoke ločljivosti HPLC in kapilarna elektroforeza, ali bioanaliznimi testi v pretočni injekcijski analizi. Primeri vključujejo določevanje snovi kot so pesticidi, antioksidanti in amino kisline v vzorcih iz

okolja in hrani. Predstavljene metode omogočajo spodnjo mejo detekcije v koncentracijskih območjih okrog μg/L do 100 μg/L, odvisno od analita in tudi matriksa oziroma same narave vzorca. Za tehniko TLM v kombinaciji s kemijskimi mikročipi so podani primeri hitre detekcije različnih analitov (Co, Fe(II), pesticidi, farmacevtiki, interferon, askorbinska kislina) v mikroliterskih volumnih okoljskih in biloških vzorcev, s spodnjimi mejami detekcije v koncentacijskih območjih od nekaj μg/L do mg/L.

V eksperimentalnem delu sta predstavljena dva sisema TLS izdelana v okviru te disertacije. Podrobno so opisani njuni sestavni deli in princip delovanja. Za vzbujanje sta uporabljena dva izvora svetlobe: argonski laser in ksenonova žarnica kot vir nekoherentne svetlobe. Za različne namene eksperimentov in aplikacije so uporabljene različne celice za vzorce (pretočne, statične, kemijski mikročip) in tudi različni vzorci.

Glavni del in pomembni prispevki disertacije so opisani v poglavju Rezultati in razprava, kjer je uvodoma predstavljen razvoj novega teoretičnega modela TLS v mikroprostoru. Za to potrebne porazdelitve temperature v vzorcu in njegovi okolici so bile izračunane z upoštevanjem dejavnikov, kot so divergenca vzbujevalnega žarka, pretok vzorca in vplivov slojev nad in pod vzorcem ter sten merilne celice. Model postavljen na osnovi Fresnelove teorije difrakcije vključuje možnost vzbujanja z žarki, ki imajo Gaussovo radialno porazdelitev intenzitete, kot tudi z žarki, pri katerih je radialna porazdelitev intenzitete svetlobe v obliki klobuka (top-hat).

Numerične simulacije in testiranja so omogočila nekatere zanimive napovedi glede lastnosti toplotnih leč v mikroprostoru, ki v prejšnih teoretičnih modelih TLM niso bile upoštevane. Z razliko od dosedaj uveljavljenega principa maksimalnega možnega fokusiranja, model predvideva možnost izbire optimalnega (večjega) radija vzbujevalnega žarka v gorišču glede na debelino vzorca, s čimer dosežemo večjo občutljivost meritev TLM. Za doseganje boljših občutljivosti in širšega področja linearnosti lahko predvidimo tudi primeren zamik osi vzbujevalnega in tipalnega žarka v vzorcu glede na smer in hitrost pretoka. Teoretična analiza vplivov okolja vzorca pa je pokazala, da v primeru TLM z nekoherentnimi viri svetlobe lahko dosežemo do 10-kratno zvišanje občutljivosti če pod in nad analizirani vzorec (v smeri osi vzbujevalnega žarka) dodamo snovi z visokim temperaturnim koeficientom lomnega količnika ($\partial n/\partial T$) in nizko toplotno prevodnostjo (k).

V nadaljevanju je opisana izdelava in optimizacija TLM, ki omogoča vzbujanje z laserjem ali z nekoherentnim virom svetlobe. Optimizacija obeh sistemov je bila predvsem usmerjena v doseganje nižjih mej detekcije na podlagi numeričnih analiz. Na osnovi TLM meritev z laserskim vzbujanjem je bila predlagana empirična formula, ki za dano debelino vzorca omogoča določitev optimalnega radija vzbujevalega žarka v gorišču, za končno velikost toplotne leče v vzorcu pa lahko določimo tudi optimalne parametre tipalnega žarka (radij, položaj gorišča) za doseganje višje občutljivosti in intervala linearnosti meritev. Za pretočne vzorce je bil eksperimentalno določen zamik osi vzbujevalnega in tipalnega žarka v vzorcu za različne hitrosti pretokov. Tudi v tem primeru se eksperimentalni rezultati dobro ujemajo s teorijo in prispevajo k izboljšanju občutljivosti in območja linearnosti.

Opravljena je bila tudi podrobna analiza šuma meritev v statičnem in pretočnem načinu. Višja občutljivost in znižanje šuma zaradi točkovne nestabilnosti tipalnega žarka sta bila v statičnem načinu, kjer prevladuje zrnati šum (shot noise), dosežena s postavitvijo reže pred detektor. Najvišje razmerje signal/šum je bilo doseženo pri vrednosti razmerja reže in radija tipalnega žarka [$d_{ph}/(2w_2)$] 0,35. V pretočnem načinu je pri razmerju $d_{ph}/(2w_2)$ manjšem od 1 prevladoval šum zaradi pretoka vzorca, pri razmerjih $d_{ph}/(2w_2)$ večjih od 1,2 pa je prevladoval zrnati šum. Najvišje razmerje signal/šum smo v pretočnem načinu dosegli pri razmerjih premerov reže in tipalnega žarka med 0,1 in 0,4. Za raztopino feroina v statičnem vzorcu

debeline 100 μm je bila pri moči vzbujevalnega žarka 4 mW (514,5 nm) tako dosežena spodnja meja detekcije $9,6 \times 10^{-7}$ absorpcijskih enot, v pretočnem vzorcu pa le $3,5 \times 10^{-5}$ absorpcijskih enot.

Kot primer praktične aplikacije TLM meritev v pretočnem načinu je v disertaciji prikazana določitev Cr(VI) v mikrofluidnem FIA-TLM sistemu po barvni reakciji z difenilkarbazidom (DPC). Dosežena je bila spodnja meja detekcije 3,5 ng/mL Cr(VI) pri moči vzbujevalnega laserja 60 mW, kar je v primeru Cr(VI)-DPC enakovredno $1,85 \times 10^{-5}$ absorpcijskih enot pri valovni dolžini argonskega laserja 514,5 nm. Glavne prednosti metode so primerljiva občutljivost s spektrofotometrijo kljub 100 krat krajši optični poti. V primerjavi s FIA-TLS pa omogoča metoda TLM 100 krat manjšo porabo vzorca in reagentov. Poleg tega tudi ni potrebno dodajanje topil, ki dodatno razredči vzorec in zviša mejo detekcije ko želimo izenačiti optotermične lastnosti nosilne tekočine in vzorca, saj prevelika razlika teh lastnosti moti ali celo onemogoča meritev.

Pri TLM meritvah z nekoherentnimi svetlobnimi izvori smo potrdili teoretično napovedano optimalno razdaljo med goriščem tipalnega žarka in vzorcem. Pri goriščnem radiju vzbujevalnega žarka 100 μm je znašala razdalja $z_1 = -5$ cm za dane parametre tipalnega žarka (goriščni radij 25 μm in razdalja do detektorja 50 cm). To se dobro ujema z napovedano razdaljo $z_1 = -17 z_R$. V tem primeru je radij tipanega žarka v vzorcu 400 μm. Teoretični izračuni so pokazali, da je primeren radij tipalnega žarka dvakrat manjši od radija merilne celice, da se izognemo interferencam zaradi robov celice. Temu primerno je za dani primer minimalni radij celice 1,6 mm, kar smo tudi uporabili v eksperimentu.

Za vodne vzorce smo kot snov z visokim $\partial n/\partial T$ in nizko toplotno prevodnostjo uporabili n-oktan v trislojnem sistemu (oktan/vzorec/oktan) in tako dosegli spodnjo mejo detekcije $2,2 \times 10^{-5}$ absorpcijskih enot, kar predstavlja 8,5 kratno zvišanje občutljivosti in znižanje spodnje meje detekcije v primerjavi z meritvijo v 100 μm celici ($1,45 \times 10^{-4}$ absorpcijskih enot) pri moči vzbujevalne svetlobe 1,05 mW. V tem primeru je prevladoval 1/f šum, optimalno razmerje radijev reže pred detektorjem in tipalnega žarka pa smo dosegli pri vrednosti 0,05.

V celoti daje disertacija nove in kompleksnejše opise pojava toplotne leče v mikroskopskih vzorcih, kar predstavlja vodilo za razvoj in izdelavo novih TLM instrumentov in optimizacijo signala toplotne leče v kemijskih mikročipih ali miniaturiziranih mikrotiterskih ploščah. To pa bo omogočilo občutljivejšo, hitrejšo in bolj specifično detekcijo različnih snovi.

SUMMARY

In recent years, due to need and consumption of large amounts of foods, drugs and pesticides in the world, people have generated many related wastes and toxic compounds, some of which are discharged directly into environment and present a great threat to human's health and to the environment itself. Some toxic compounds of concern include pesticides, heavy metals, pharmaceuticals, allergens, biogenic amines and toxins. To assess these compounds quantitatively, various techniques have been developed and employed, which range from the commonly used chromatographic techniques and spectroscopy to bioanalytical assays and their combinations, the so called hyphenated techniques. In these systems, thermal lens spectrometry (TLS) has been extensively used as technique for analyte detection, primarily because of its ultra-high sensitivity and fast response. A milestone in further development of TLS is the introduction of thermal lens microscope (TLM), which made TLS suited for microscale detection, such as in microfluidic systems and lab-on-chip chemistry. Important contributions regarding the detection sensitivity and specificity of TLS and TLM have been made by many researchers, but TLS in general still does not reach maturity and applicability in routine chemical analysis. This can be attributed to two main reasons. The first reason is common to all TLS methods and is related to limited availability of appropriate light sources for TLS, which requires light sources (lasers) providing Gaussian beam profile for generation of the thermal lens effect. Laser emissions are however limited to single or very few wavelengths. This seriously limits the specificity of TLS technique and consequently its application in practical chemical analysis. The second reason is specific to TLM and is related to the analysis of TL signal in TLM, which is based on conventional TLS theories valid in macroscopic samples where effects of the surroundings or sample thickness are not considered. With respect to these drawbacks, research was proposed to advance the TLS technique further to enable new practical applications.

In the second chapter of this dissertation extensive theoretical background on TLS is given and its applications by combining different methods (separation techniques, biosensors, FIA and microfluidics) for the detection of toxic and bioactive compounds in environmental samples are reviewed. As a sensitive photothermal method enabling indirect detection of sample absorbance down to 10^{-7}, TLS has been applied in chemical analysis over 30 years. As part of the development of TLS technique, different theoretical models based on the simplified parabolic approximation or the Fresnel diffraction model have been employed for describing the TL signal in static or flowing samples and correspondingly, TLS instruments have evolved from single-beam to dual-beam configuration, from common TLS to modified setups (such as differential TLS, phase-conjugated TLS) for special detection requirements, from laser-excited to ILS-excited TLS, and from macroscopic conventional TLS to TLM applicable in micro-space. Regarding the practical applications, examples of chemical analysis by TLS coupled to separation techniques (HPLC, CE) or bioanalytical-FIA systems are reviewed for the detection of compounds such as pesticides, antioxidants, amino acids, etc. in environment or in food stuffs with LODs from ~ μg/L to ~100 μg/L for different analytes and sample matrixes. For the TLM combined with microchip chemistry, application examples for the fast and microvolume detection of analytes in environmental or biological samples (such as cobalt, Fe(II), pesticides, pharmaceuticals, interferon(IFN), ascorbic acid) with LODs from ~ μg/L to ~mg/L are shown.

In the instrumental part, two TLM systems built in house, as well as their components, are introduced and their operation is discussed in detail. In these systems, different excitation

light sources (lasers, ILS), sample cells and samples are used for different experimental purposes and applications.

The major part and contributions of this dissertation are described in the section Results and discussion which initially describes the development of a novel theoretical model of TLS in microspace. Temperature distributions in the sample system were deduced with respect to different impact factors on the TL signal, including the pump beam divergence, flow of the sample and impacts of the top/bottom layers and sidewalls of the sample cell. Both the Gaussian and top-hat excitation beam profiles were included in the model which is built based on the Fresnel diffraction theory. Subsequent numerical simulations provided some interesting predictions. These include an optimum pump beam waist radius for a given sample length to achieve the maximum sensitivity, an appropriate beam offset between the pump and probe beams for a higher sensitivity and linear signal response in a flowing sample, and a sensitivity enhancement of up to 10 times in ILS-excited TLS when using materials with high $\partial n/\partial T$ and low k as the top/bottom layers adjacent to the analyzed sample.

Following the numerical simulations the construction and optimization of laser- and ILS-excited TLM systems is described. Based on numerical analysis, the two systems were optimized for lower limits of detection (LODs). Based on laser-excited TLM experiments, an empirical formula for the optimum pump beam waist radius for a given sample length is proposed for estimation of experimental parameters for highest sensitivity, and for a "finite TL element", appropriate probe beam parameters were determined to obtain a high detection sensitivity and good response linearity. In flowing mode, an appropriate beam offset between the pump and probe beams was determined experimentally for different flow velocities. This improved the sensitivity and in addition assured a linear signal response. Noise levels in both static and flowing modes were analyzed. In static mode, the noise was found to be dominated by the shot noise and the optimum pinhole aperture-to-beam size ratio $[d_{ph}/(2w_2)]$ for the highest signal-to-noise ratio was found to be 0.35. In the flowing mode, at relatively small $d_{ph}/(2w_2)$ (such as below 1), the noise was dominated by the flow-induced noise while for large $d_{ph}/(2w_2)$ (such as above 1.2) the shot noise was dominant. The pinhole aperture-to-beam size ratio can be chosen between 0.1 and 0.4 for high signal-to-noise ratios. At 4 mW pump power in the sample, LODs of 9.6×10^{-7} AU and 3.5×10^{-5} AU were calculated for 100 μm thick ferroin solution in static and flowing modes, respectively. As an application, Cr(VI) was determined on a microfluidic-FIA-TLM setup following a colouring reaction with diphenylcarbazide (DPC). A LOD of 3.5 ng/mL for Cr(VI) was obtained at the power of 60 mW, corresponding to an absorbance of 1.85×10^{-5} AU for Cr(VI)-DPC at 514.5 nm. This setup has many advantages over conventional FIA-TLS setup, such as 100 times lower sample/reagent consumption, and no need of adding solvents to sample solution to match the physical properties of the carrier liquid containing the reagents.

In ILS-excited TLM, the theoretically predicted distance between the probe beam waist and the sample was experimentally confirmed. At pump beam radius of 100 μm in the sample, this optimal distance was found at $z_1 = -5$ cm for given probe beam parameters with beam waist radius 25 μm and detection distance 50 cm, which is in good agreement with the theoretical value $z_1 = -19z_R$. In this case the probe beam radius in the sample is 400 μm. Theoretical calculation shows that the probe beam waist radius should be two times smaller than the sample cell radius to avoid interference with the probe beam by the sample cell boundary. Accordingly for the given case, the diameter of the sample cell should be larger than 1.6 mm. In experiment, sample cells meeting this requirement were employed. For aqueous samples, materials with high $\partial n/\partial T$ and low k (n-octane) were used in a three-layer system (n-octane/sample/n-octane) to enhance the detection sensitivity. It was demonstrated that the TL signal was enhanced by 8.5 times in the three-layer system compared to that in a standard 100

μm cell. The dominating noise in the system was the flicker noise and the optimum pinhole aperture-to-beam size ratio for the best signal-to-noise ratio was found to be 0.05. The LOD of 1.45×10^{-4} AU was obtained for 100-μm ferroin solution without signal-enhancement layers while the LOD was lowered to 2.2×10^{-5} AU with signal-enhancement layers (n-octane) at P=1.05 mW.

In summary, this dissertation gives a novel and comprehensive description of TLS technique in micro space, which provides a guide for building TLM instruments and for optimizing TL signal in a microchip or in miniaturized microtiter plates for sensitive, specific and high throughput detection of various analytes.

TABLE OF CONTENTS

X

LIST OF FIGURES

XIV

LIST OF TABLES

ABBREVIATIONS

AA – Ascorbic acid
AC – Alternating current
AChE – Acetylcholinesterase
AOPs – Advanced oxidation processes
AOTF – Acousto-optic tunable filter
βLG – β-lactoglobulin
BuChE – Butyrylcholinesterase
CD – Circular dichroism
CE – Capillary electrophoresis
CEA – Carcinoembryonic antigen
CFCP – Continuous-flow chemical processing
ChE – Cholinesterase
CL – Collimating lens
Cr – Chromium
CW – Continuous wave
DAD – Diode-array detection
DC – Direct current
DIC – Differential interference contrast
Dm – Drosophila melanogaster
DPC – Diphenylcarbazide
EC – Electrochemical detection
ECD – Electron capture detector
EDFA – Erbium-doped fiber amplifier
EDTA – Ethylenediaminetetraacetic acid
ELIAC – Enzyme linked immunoaffinity chromatographic
ELISA – Enzyme-linked immunosorbent assay
EU – European Union
FBS – Fetal bovine serum
FFAs – Free fatty acids
FIA – Flow injection analysis
FID – Flame-ionization detector
FLISA – Fluorescent immunosorbent assays
GC – Gas chromatography
HBS-EP – 10mM Hepes, 150mM Sodium Chloride, 3mM EDTA, 0.005% Polysorbate 20
HLA – Human leukocyte antigen
HPLC – High performance liquid chromatography
IC – Ion chromatography
ID – Inside diameter
IFN – Interferon
ILS – Incoherent light source
IR – Infrared
LCPL – Left circularly polarized laser light
LD – Laser diode
LED – Light-emitting diode
LIF – Laser-induced fluorescence
LOC – Lab-on-a-chip
LOD – Limit of detection
MALDI – Matrix-assisted laser desorption ionization

MC – Microcystins
ME – Microchip electrophoresis
MEKC – Micellar electrokinetic chromatography
MS – Mass spectrometric or mass spectroscopy
MUOs – Microunit operations
nAChRs – nicotinic acetylcholine receptors
NOD – Nodularin
OL – Objective lens
OP – Organophosphate
OPH – Organophosphorus hydrolase
PAH – Polycyclic aromatic hydrocarbon
PAR – 4-(2-pyridylazo) resorcinol
PCR – Polymerase chain reaction
PD – Photodiode
PDCA – Pyridine-2,6-dicarboxylic acid
PDMS – Polydimethylsiloxane
PMMA – Poly(methyl methacrylate)
PPCPs – Pharmaceuticals and personal care products
RCM-βLG – Reduced and carboxymethylated form of βLG
RCPL – Right circularly polarized laser light
RIC – Relative intensity change
RID – Refractive-index detector
rFIA – Reversed flow injection analysis
rms – Root-mean-square
RSD– Relative standard deviation
RTILs – Room temperature ionic liquids
S/B – Signal-to-background
S.D. – Standard deviation
S/N– Signal-to-noise ratio
SFE – Supercritical fluid extraction
SFS – Scan fluorescence spectroscopy
SHG – Second harmonic generation
SPE – Solid phase extraction
SPR – Surface plasmon resonance
STP – Sewage treatment plant
TCD – Thermal conductivity detector
TL – Thermal lens
TLC – Thin-layer chromatography
TLE – Thermal lens effect
TLM – Thermal lens microscope
TLS – Thermal lens spectroscopy
TPA – Two-photon absorption
Tyr – Tyrosinase
UV-vis – Ultraviolet-visible
VOC – Volatile organic compound
μ-TAS – Micro total analysis system
1-D, 2-D and 3-D, or one-D, two-D and three-D – One-dimensional, two-dimensional and three-dimensional

SYMBOLS

α, α_s, α_D – Absorption coefficient, absorption coefficient of sample, absorption coefficient of the detector

a, a_e, a_e0 – Radius of the sample cell, excitation beam radius, excitation beam waist radius

A or A_s – Absorbance

ε – Molar absorption coefficient

β – Lateral magnification of an optical system

c or C, C_p – Concentration, specific heat

d, d_opt – Distance between lenses or beam offset between the pump and probe beams, optimum beam offset

d_c – Diameter of the microchannel

d_ph – Diameter of the pinhole before detector

D – Thermal diffusivity

D_m – Mass-diffusion coefficient or molecular diffusion coefficient

D_th – Thermal diffusion length

$E(\cdot)$ – Electric field

f – Modulation frequency, or focal length of lens

F – Focal point

$g(\cdot)$, g – Heat generation rate (heat source term), gravity acceleration

h – Convective heat transfer coefficient, or hour

H – Principal point

H_m – Distance of the sample cell movement along optical axis

I – Light intensity, or current

$J_0(\cdot)$, $J_1(\cdot)$ – Zero- and first-order Bessel functions of the first kind

k – Thermal conductivity

l, l_f – Sample length, length of fluid

L, L_m – Distance, molecular diffusion distance

m – Mode-mismatching degree, or minute

n – Refractive index, or a symbol for numbering

v_x – Flow velocity in x-direction

q – Complex radius of a Gaussian beam

Q – Flow rate

ρ – Density

P – Light power

Re – Reynolds number

S – TL signal

S_ac – Relative intensity change of the probe beam

S_b – Background signal of the photodetector at certain gain

S_T – Soret coefficient

S_m – Interface area

S_dc – Probe beam intensity in the detection plane before excitation

S_dc0 – Measured probe beam intensity by photodetector at certain gain

t, t_c, t_m – Time, thermal time constant, molecular transportation time

T – Temperature

V – Volume

ω – Angular modulation frequency

w_1 – Probe beam waist radius after the objective lens

w_2 – Probe beam radius in the detection plane

w_s – Probe beam radius in the sample plane

z_1, z_{1opt} – Distance from the probe beam waist to the sample plane, the optimum z_1 where TL signal achieves maximum

z_2 – Distance from the sample plane to the detector plane

z_R – Rayleigh range of a Gaussian beam

$\partial n/\partial T$ – Temperature coefficient of refractive index

θ, θ_1 – Thermal lens enhancement factor, beam divergence of a Gaussian beam

η – Fluorescence quantum efficiency, or coefficient of viscosity

σ_m – Specific interface area

ΔH – Height difference

Θ – Full angle of beam divergence of a Gaussian beam

$\Delta\Phi(\cdot)$ – Phase shift induced by the thermal lens element

λ, λ_e, λ_h – Wavelength of the probe beam, wavelength of the excitation beam, thermal wavelength

1   INTRODUCTION

Various toxic compounds, such as pesticides, allergens, pharmaceuticals, toxins and heavy metals, are widely present in environment and food products, and pose a serious threat to the food safety and human's health. Several types of pesticides, including organophosphate (OP), carbamate, and neonicotinoid pesticides, have been applied in vast amounts in many countries due to their relatively low environmental persistence. The results of pesticide residue monitoring program performed in European Union (EU) countries showed that 45% of screened food samples contained pesticide residues [1]. In Slovenia, some pesticides are registered and they will be in use at least till the year 2016. These compounds usually have high acute toxicity. Some are suspected carcinogens and mutagens [2]. Food allergy is now recognized as a worldwide problem and it seems to be on increase. In the US food allergy affects up to 5% of children less than 5 years of age and approximately 4% of the general population [3]. Pharmaceuticals represent a group of emerging chemicals of environmental concern widely used in human and veterinary medicine. Pharmaceuticals have been found in surface waters and wastewaters at levels of up to a few μg/L. Another group of toxic compounds, which become of much interest recently, are the toxins released by microorganisms in sea or other environments, such as the cytotoxin [4] and cyanotoxins [5]. Cyanotoxins are the naturally produced poisons stored in the cells of certain species of cyanobacteria. These toxins fall into various categories. Some are known to attack the liver (hepatotoxins) or the nervous system (neurotoxins); others simply irritate the skin. These toxins are usually released into water when the cells rupture or die. Anatoxin-(a)-S is an acetylcholinesterase (AChE) inhibitor while microcystin and nodularin are protein phosphatase inhibitors. Within the European community, several heavy metals of highest concern are lead, mercury, cadmium, chromium, etc. [6]. Some of these elements are actually necessary for humans in minute amounts (cobalt, copper, chromium, manganese, nickel) while others are carcinogenic or toxic, affecting the central nervous system (manganese, mercury, lead, arsenic), kidneys or liver (mercury, lead, cadmium, copper) or skin, bones, or teeth (nickel, cadmium, copper, chromium). Heavy metal pollution can arise from many sources but most commonly arises from the purification of metals, e.g., the smelting of copper and the preparation of nuclear fuels. Electroplating is the primary source of chromium and cadmium. Through precipitation of their compounds or by ion exchange into soils and muds, heavy metal pollutants can localize and lay dormant. Unlike organic pollutants, heavy metals do not decay and thus pose a different kind of challenge for remediation.

Due to the potential risk of these toxic compounds to the environment and human's health, different kinds of analytical techniques and detection methods have been developed for studies on the occurrence, fate and concentration of these compounds and their metabolites. Chromatographic techniques, which are highly sensitive and selective, are commonly used for analysis of various compounds [7]. Another separation technique, namely capillary electrophoresis (CE), also found many applications in environmental and food analysis [8] due to its faster analysis over chromatographic techniques. Besides, bioanalytical systems, which are usually based on enzymatic reactions or immunoassays were developed to realize rapid and low-cost detection [9]. In these chromatographic, electrophoretic or biological systems, a variety of detection techniques (electrochemical detection, thermal-conductivity detection, mass spectrometry, optical transmission, fluorescence, photothermal effects, etc.) were employed to meet different detection requirements. Among them, thermal lens spectrometry (TLS), as a highly sensitive photothermal technique with unique characteristics (such as non-contact detection, small sample volume requirements, high temporal and or spatial resolution), has been applied for detection of nonfluorescent samples or even for

photolabile analytes in macro space, such as in spectrophotometric cuvettes or flowing sample cells [10], or in micro space, such as in a capillary [11] or in a microchip [12]. For the detection in microchip, miniaturized instrumentation of TLS — thermal lens microscope (TLM), was developed and already found many applications in biochemical analysis [13]. However, TLS or TLM are still too far from maturity to be applied for routine chemical analysis mainly because of their low specificity caused by the limited number of emission lines of lasers available for excitaition. Therefore, further study of TLS, and especially the TLM when excited by different light sources (lasers, incoherent light sources), and promoting its application in environmental analysis, particularly when coupled to microfluidic devices, will be the objective of the research within this dissertation.

In this dissertation, the state of the art of analytical methods for the detection of toxic compounds is first given, and then research goals and methods in my research are presented. Secondly, in the experimental part, both a laser- and an incoherent light source (ILS)-excited TLM systems made in lab, as well as related components and sample/reagents, are introduced. In the next chapter of results and discussion, a theoretical model of TLS in micro space is presented, and based on this model, influences of different systematical parameters on the TL signal are analyzed on the TLM systems and consequently, the LOD of the systems are optimized. As a practical application, Cr(VI) was detected in a microfluidic-FIA-TLM setup with many superiorities over conventional FIA-TLS setup. Finally, conclusions and future prospects are presented.

2   THEORETICAL BACKGROUND

In this chapter, main techniques for the detection of toxic compounds in environment are reviewed. These techniques include different separation techniques and biosensors, coupled with various detectors, from electrical, thermal, optical to photothermal detectors. Among them, an emphasis is put on one of the photothermal technique, namely thermal lens spectrometry and its miniaturized instrumentation — thermal lens microscope (TLM), which is also the method to be further discussed in my research. In addition, as one of important trends of future chemical analyses, microfluidic devices and their applications when combined with TLM are reviewed.

2.1   Analytical methods for toxic compounds in environment

In the chapter of introduction, some toxic compounds in environment were mentioned. In this section, the state-of-the-art of corresponding analytical methods is summarized. These methods can be classified into two types, namely, chromatographic techniques and bioanalytical systems. Chromatographic techniques include techniques such as high performance liquid chromatography (HPLC) and gas chromatography (GC). Bioanalytical systems mainly comprise enzymatic methods and immunoassay.

2.1.1   Chromatographic techniques

As shown in Fig. 1, in chromatographic techniques, a sample dissolved in a mobile phase (which may be a gas, a liquid or a supercritical fluid) is forced through an immobile, immiscible stationary phase. The phases are chosen such that components of the sample have differing solubilities in each phase. A component which is quite soluble in the stationary phase will take longer to travel through it than a component which is not very soluble in the stationary phase but very soluble in the mobile phase. As a result of these differences in mobilities, sample components will become separated from each other as they travel through the stationary phase, and then the components will be separately detected by a detector.
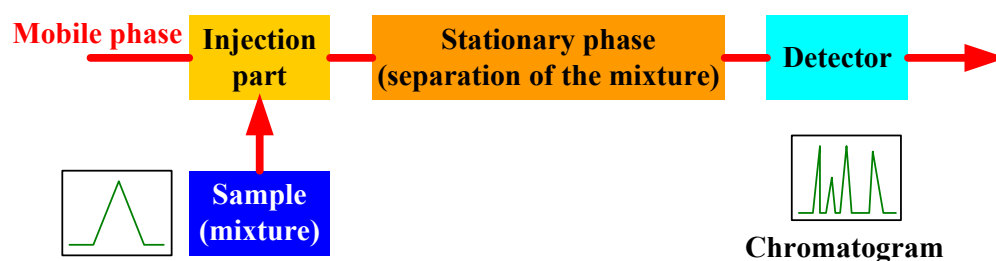
Figure 1: Block diagram of chromatographic technique

Most frequently used methods are GC with thermal-conductivity detector (TCD), flame-ionization detector (FID) and mass spectrometric detector (MSD), or HPLC with UV-Vis detector, refractive-index detector (RID) and MSD [14-16]. In Table 1, three types of chromatographic methods are summarized. The main advantages of these methods are their sensitivity and selectivity, as the limit of detection (LOD) is usually in the sub µg/L to several µg/L range. For example, quantitative analysis of trace level carbamate pesticides in surface, municipal and wastewater was realized by using liquid-liquid extraction and a liquid chromatography quadrupole system coupled to a diode-array detector (DAD). Tsumura et al. [17] described the determination of traces of carbamates in grains, fruits and vegetables with

HPLC. Recovery of pesticides in different food matrices varied from 60 to 103% and the LODs from 1 to 4 ng/mL.

Monaci et al. developed a method using solid phase extraction (SPE) and LC coupled to MS to detect traces of three allergenic cow milk proteins (lactalbumin, lactoglobulins A and B) in mixed-fruit juice samples [18]. Recoveries ranging from 68% to 79% were achieved for 5 and 20 μg/mL tested samples and the LOD was obtained at 1 μg/mL. Comprehensive two-dimensional GC coupled with quadrupole MS and with FID were used for the analysis of suspected allergens in fragrances (α-isomethyl-ionone, benzyl alcohol, cinnamic aldehyde, estragole, farnesol isomer, geraniol, hexylcinnamic aldehyde, isoeugenol, limonene, etc.) with LODs of 4~8 ng/mL [19].

Pharmaceuticals [five anti-inflammatory drugs (acetaminophen, diclofenac, ibuprofen, ketoprofen and naproxen), an antiepileptic drug (carbamazepine) and a nervous stimulant (caffeine)] in wastewater influents and effluents from wastewater treatment plants were determined simultaneously by HPLC with DAD and fluorescence detection [20]. The method involves pre-concentration and clean-up by SPE using Oasis HLB extraction cartridges. Recoveries were ranged from 71 to 103% with relative standard deviation below 15.1%. Limits of quantification were in the range 20–960 and 10–500 ng/L for influent and effluent wastewater samples, respectively. Gómez et al. [21] identified and quantitatively determined 16 pharmaceuticals [the anti-epileptic carbamazepine, seven analgesic/anti-inflammatory drugs (mefenamic acid, indomethacine, ibuprofen, naproxen, diclofenac, ketorolac and acetaminophen), the analgesic opiate codeine, two antidepressants (fluoxetine and paroxetine), β-blockers (atenolol and propranolol), antibiotic (trimethoprim, metronidazole, and erythromycin) and the anti-ulcer ranitidine] in hospital effluent wastewaters by LC-MS-MS using multiple reaction monitoring. The LOD was between 7 and 47 ng/L in spiked hospital effluent. Besides, chemiluminescence detection [22] and evaporative light scattering detection [23] were also coupled to HPLC for pharmaceuticals and metabolites analysis. Thin-layer chromatography (TLC) combined with matrix-assisted laser desorption ionization (MALDI) was used for pharmaceutical analysis and the LOD for piroxicam was 39 ng/mL [24].

However, chromatographic analysis of samples requires several steps in sample pretreatment, namely matrix modification, extraction and clean-up [25-27]. These steps are often time- and solvent-consuming. And finally, the price of the laboratory equipment and operational costs is usually high. Consequently, these methods are not very suitable for monitoring large number of samples. So other kinds of techniques are also developed.

Table 1: Chromatographic techniques and their corresponding characteristics

	Mobile phase	Stationary phase	Detectors (examples)	Applicability
GC	Gases (H_2, N_2, Ar, He)	Capillary or packed columns with substituted siloxanes	TCD, FID, MSD	Volatile organic compounds, gases
HPLC	H_2O, organic solvents		UV-VIS, RID, MSD	Organic compounds and inorganic salts
TLC	Vapor of organic solvents	Impregnated plates	Optical detection (UV-VIS, fluorescence)	Organic compounds

2.1.2 Capillary electrophoresis

Capillary electrophoresis (CE) is another separation technique, which was developed as an alternative or complementary technique to chromatographic techniques. Since the first

demonstration of high separation efficiency with CE [28], the technique has advanced significantly. Unlike chromatographic techniques, in which separation is due to the partition of solutes between the mobile phase and stationary phase, separation by CE is based on the difference in charge-to-mass ratio of the analytes. Compared to chromatographic techniques, CE features faster analysis and method development, lower expenses for consumables and easier operation, but it is less sensitive (LODs with CE are in general an order of magnitude higher than those with LC) [29]. On-line SPE is the preferred pre-concentration technique to improve the detection limits of CE.

García et al. used CE-electrospray ionization-quadrupole ion trap-tandem MS (CE-ESI-MS-MS) to identify and quantify six pesticide residues (dinoseb, pirimicarb, procymidone, pyrifenox, pyrimethanil, and thiabendazole) in peaches and nectarines [30]. Pesticide residues were preconcentrated by SPE on C18 cartridges and CE separation was carried out using a buffer of 0.3 M ammonium acetate at pH 4 with 10% methanol. The LODs for the six pesticides in spiked peach samples were 0.01 mg/kg for pirimicarb and 0.05 mg/kg for procymidone with pressure injection of 50 mbar for 5 s (5 nL).

Two major milk whey proteins (β-lactoglobulin and α-lactalbumin) were analyzed by immunoaffinity CE hyphenated with MALDI-MS [31]. Magnetic beads functionalized with appropriate antibodies were used for β-lactoglobulin and α-lactalbumin immunocapture inside the capillary. A LOD low to 18.4 μg/L was achieved for both whey proteins.

Eight pharmaceutical compounds in wastewater (ibuprofen, triclosan, carbamazepine, caffeine, acetaminophen, sulfamethoxazole, trimethoprim, and lincomycin) were analyzed by CE with UV detection (CE-UV) [32]. Following SPE, LODs from 1.6 to 68.7 μg/L were obtained, which are comparable to those of LC-MS-MS. Quek et al. realized simultaneous separation of 13 pharmaceutical products in water samples by CE with capacitively coupled contactless conductivity detection [33]. LODs were from 61 to 1676 μg/L and the relative standard deviations for migration time and peak area were below 2 and 6%, respectively.

Though CE can provide fast separations (1 to 45 min), high separation efficiency (10^5 to 10^6 theoretical plates), small sample requirement (1-10 μL) and easy coupling to MS, it still has some disadvantages such as incapability in performing preparative scale separations, difficulty in detecting sample with low concentration, and especially the reproducibility problems.

2.1.3 Bioanalytical systems

To avoid the disadvantages of chromatographic or electrophoretic techniques, different types of bioanalytical systems were developed. A bioanalytical system usually includes three basic elements (receiver, transducer and electronics component), as depicted in Fig. 2.
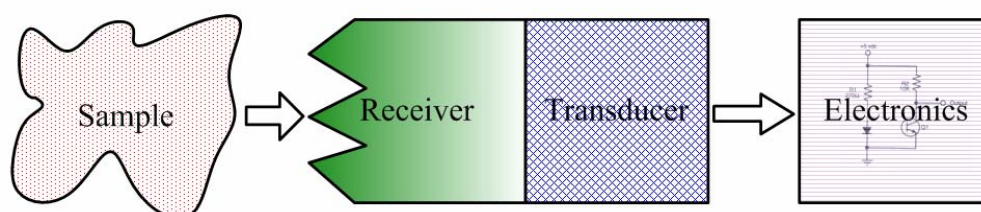
Figure 2: Three basic elements of a bioanalytical system: receiver, transducer and electronics for signal processing and recording.

Receiver is a sort of biological recognition element, which can be different enzymes, antibodies, microbial cells, etc. The receiver has to be specific for selected analyte. The transducer (e.g. optical, amperometric, or electrochemical) recognizes the biochemical

modification of the analyte and transforms it into electrical signal, which is processed and stored by data acquisition electronics.

Some detection techniques are based on several kinds of enzymes, such as tyrosinase (Tyr) organophosphorus hydrolase (OPH), cutinase, cholinesterases (ChE). Bucur et al. chose wild and genetically engineered AChEs from drosophila melanogaster (Dm) to achieve high sensitivity towards three carbamate insecticides (carbaryl, carbofuran and pirimicard) [34]. The best LODs were obtained with the Y370A mutant for carbaryl (2 ng/mL), the E69W mutant for pirimicarb (4.8 ng/mL) and the I161V mutant for carbofuran (0.17 ng/mL).

Another kind of bioanalytical technique is immunoassay, where an immunosensor combines antibody as recognition element and an appropriate transduction mechanism to convert the recognition event into detectable signal. Immunosensors are highly sensitive and specific to selected compound. A LOD as low as 55-60 pg/mL has been reached for chlorpyrifos in different environmental water samples with surface plasmon resonance (SPR) based immunosensor [35].

Negroni et al. performed two-site enzyme immunometric assays for determination of native and denatured β-lactoglobulin [βLG] [36]. The assays were performed in 96-well microtiter plates and were based on the use of pairs of monoclonal antibodies specific to either the native form or the reduced and carboxymethylated form of βLG (RCM-βLG). Detection limits of 30 and 200 pg/mL were obtained for the native βLG and the RCM-βLG assay, respectively.

Unfortunately, immunosensor's high specificity is also their main limitation. With the application of one type of antibodies, the detection of a group or class of chemicals is not possible. This problem could be mitigated to some extent by multiple and combined immobilization of several analyte recognition elements on the sensing surface.

Another variety of transducers rely on optical detection, e.g. absorbance, reflectance, scattering, luminescence and fluorescence of the samples [37, 38] or on photothermal effects of the analytes [39, 40]. Laser-induced fluorescence (LIF) has inherent high sensitivity [41] but lacks wide applicability or requires tedious derivatization reactions. Based on optical absorption-induced effect in the sample, photothermal spectrometry is another kind of sensitive detection technique. Details regarding the fundamentals of one of the photothermal techniques — TLS will be presented in section 2.3. In Table 2, a comparison between the chromatographic and bioanalytical techniques regarding their main types, advantages and disadvantages is presented.

Table 2: Comparison between chromatographic, capillary electrophoretic and bioanalytical techniques

Methods	Main types	Advantages	Disadvantages
Chroma-tographic technique	HPLC GC	(1) High sensitivity and selectivity; (2) LOD: ~ sub µg/L to ~ µg/L	1) Time- and solvent-consuming, high-cost; (2) unsuitable for large number of samples; (3) can not measure toxicity of sample.
Electropho-resis	CE, ME, MEKC	Faster analysis and method development, lower consumable expenses compared to HPLC	Relatively lower sensitivity and poor precision (hence the need to incorporate internal standards)
Bioanaly-tical system	Enzymatic (ChE)	(1) Rapid and inexpensive; (2) Provide information about toxicity of analyte.	Selectivity is not high.
	Immunoassay	High sensitivity and specificity.	Only one type of analyte is detected.

2.2 Optical transmission technique

In the field of spectroscopic analysis, due to its simplicity and rapidity, optical transmission technique is commonly used for quantitative and/or qualitative analysis of various compounds from UV to IR. It constitutes the technical basis of spectrophotometers and UV-Vis or DAD detection in chromatographic systems.

According to Beer's law, light transmittance T through a sample with length l and absorption coefficient α is expressed as

$$T = \frac{I}{I_0} = e^{-\alpha l},\qquad(1)$$

where I and I_0 are the light intensity before and after the sample, respectively.

In a spectrometer, absorbance A of an analyte is defined as

$$A = -\lg T = -\lg e^{-\alpha l},\qquad(2)$$

or if the molar absorption coefficient ε of the sample is known:

$$A = \varepsilon c l.\qquad(3)$$

Then, the absorption coefficient of the sample can be calculated as

$$\alpha = \frac{ln10^A}{l}.\qquad(4)$$

The optical transmission technique can detect absorbance down to $10^{-3} \sim 10^{-4}$ AU in a 1-cm sample cuvette. Some researchers have tried some ways to increase the sensitivity in microspace. The most common way employed is to increase the optical path length of the sample. Zhang used a long liquid waveguide capillary flow cell from 0.5 m to 4 m in spectrophotometric detection and the sensitivity was increased by two orders of magnitude [42, 43]. Though this sounds exciting, it suffers many disadvantages, such as the requirement of high-purity solution with no micro-bubbles to avoid scattering or reflection, addition of surfactant to reduce the surface tension and thereby the back pressure in the flow stream, higher reagent consumption, slow response time, etc.

If this technique is applied in a micro space with sample length of sub-millimeter, the LOD would be only 10^{-3} AU or higher, which is not applicable for practical situations where the concentration of analyte is usually low. Gaspar et al. applied an external lengthened 5-mm-long channel on a microchip and a LOD of ~0.006 AU at 640 nm was obtained [44].

2.3 Thermal lens spectrometry

The majority of biologically important chemicals, such as amino acids, nucleotides, proteins, and hormones are natively nonfluorescent. As for nonfluorescent single molecule detection, electrochemical methods can detect single molecules in a liquid solution [45], and surface-enhanced Raman scattering may be applied if the adsorbed molecule on a silver nanoparticle is the target [46]. However, these methods have quite limited fields of applications. The development of a more general method for nonfluorescent molecule detection could be quite desirable in biochemical or biomedical analysis. Photothermal spectroscopy-based techniques have great potential for the sensitive detection of nonfluorescent molecules.

TLS is known as one of the most sensitive photothermal spectroscopic techniques for measurements in liquids. Owing to its inherent high sensitivity, TLS enables measurement of

optical absorbance lower than 10^{-7}. Other important characteristics of TLS include the possibility of probing very small (sub pL) volumes as well as relatively fast signal response, which is on the millisecond time scale and enables TLS detection in flowing samples.

2.3.1 Principle and development of TLS

2.3.1.1 Basic principle of TLS

The thermal lens effect was observed in 1965 [47], and has been used extensively for trace chemical determination since 1979. In TLS, a modulated continuous-wave (CW) or pulsed laser beam (or other light sources) is employed to illuminate the sample. The sample absorbs the excitation beam, and then a temperature gradient is produced by the nonradiative relaxation of the absorbed energy. If the temperature coefficient of refractive index ($\partial n/\partial T$) of the sample is nonzero, a refractive-index gradient element occurs in the sample. The effect caused by this lenslike optical element is called thermal lens (TL) effect, which is detected by the pump beam itself (in single-beam configuration) or by another lower-power laser beam (namely, probe beam, in dual-beam configuration, as displayed in Fig. 3). Then the TL element-induced probe beam intensity change ΔI is detected by a photodetector through a pinhole. ΔI is usually proportional to the concentration of analytes for a certain range (3 ~ 5 orders of magnitude) in diluted solutions. Then information of the sample (absorbance, thermo-physical parameters) can be obtained through certain analysis. In principle, any substance absorbing the light can be detected by TLS, even fluorescent compounds.
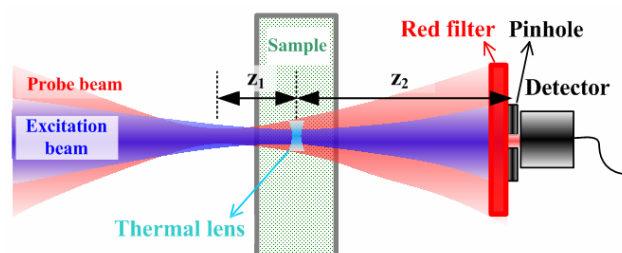
Figure 3: Schematic illustration of dual-beam collinear thermal lens technique.

2.3.1.2 Classification of TLS

Different theoretical descriptions of the TL effect under a variety of experimental conditions can be found in the literature and have been reviewed extensively in several books and review articles [48-54]. These models cover TL effects generated under pulsed and CW excitation, and under different pump/probe geometries, i.e. single and dual beams as well as collinear and crossed-beam configurations. Therefore, TLS can be classified from different pump-probe beam geometries (single- or two-beam), detection mechanisms (near- or far-field) and types of excitation source (pulsed or CW, Gaussian or top-hat). In Fig. 4, examples of some TLS are listed. These instruments can, in general, be classified into two basic categories, i.e. single-beam and dual-beam (pump/probe) instruments. Single-beam instruments [55, 56] were widely used in the initial stages of TLS development. They are simple for their construction and easy for operation, but the sensitivity is low because the focusing point of the light, which is closely related to the TL signal strength, is away from the sample centre. To enhance the sensitivity, two-beam instruments were developed. The dual-beam instruments can be subdivided into two modes, crossed-beam configuration [57], which is applicable to small-volume detection, such as in CE, and collinear configuration [58], which keeps better absolute sensitivity by lengthening the optical interaction length. Besides, for detection of special samples, several TLS instruments were developed, such as differential TLS for detection in high background absorption solvents [59, 60], phase-conjugate TLS for

detection of optically inhomogeneous samples [61], and TL-circular dichroism to measure circular dichroism of optically active samples [62].

Single-beam	Sensitivity is low
Dual-beam	Crossed-beam & collinear $\left\{ \begin{array}{l} \text{small-volume samples, esp. in CE} \\ \text{better absolute sensitivity} \end{array} \right.$
Differential TLS	Alleviate high background absorption of the solvent
Phase-conjugate TLS	Detect optically inhomogeneous samples
TL-circular dichroism	Measure circular dichroism of optically active samples.
Tunable TLS	Six wavelengths of Ar^+ laser used for measurement during 1.5 s; EDFA near-IR excitation light (1515 -1590 nm) to detect nucleotides.
Top-hat beam TLS	A potential for the design of practical TLS instruments with incoherent light sources

Figure 4: Examples of some TLS instruments

In TLS instruments, one of the most important constituents is the excitation source. Usually a laser beam is used as the excitation source, because of its unique properties compared to other light sources, such as high radiance, good monochromaticity, coherence and directionality. A variety of lasers have been utilized for excitation, ranging from CW gas lasers [e.g. He-Ne (540 nm, 632.8 nm, 1.15 or 3.39 μm), CO (1626–1910 cm^{-1}), CO_2 (880–1090 cm^{-1}), He-Cd (325 nm, 441.6 nm), Ar+ (351.1–1092.3 nm) and Kr+ (406.7–676.4 nm)], dye (320–1200 nm) and semiconductor lasers (380–1650 nm), to Nd:YAG lasers (1064 nm, and higher harmonics 532, 355 and 266 nm) and excimer lasers (KrF 248 nm [63]). Recently, spectrally tunable Ti-sapphire (865 to 1050 nm) [64] and F-center lasers (2.5 to 3.5 μm) [65], as well as Er-doped fiber amplifiers (1500 to 1570 nm) [66], were also used as excitation in TLS.

In visible region, Tran et al. exploited six wavelengths (457.9, 476.5, 488, 496.5, 501.7, and 514.5 nm) emitted by an Ar ion laser to excite the sample during a time period of 1.5 s [67]. The LOD is comparable to other dual-beam TL instruments, and it can be used to analyze samples with up to six different components. For determination of various inorganic species (heavy metals, inorganic anions) in visible region, coloring reagents and ligands such as 1,10-phenanthroline [68], pyridine-2,6-dicarboxylic acid (PDCA) [69, 70], 1,5-diphenylcarbazide (DPC) [69-71], and 4-(2-pyridylazo) resorcinol (PAR) [72] were used for derivatization. However, derivatization sometimes is difficult to perform especially for small molecules or it would bring unexpected interference to the analysis or cause change to the analyte, so lasers in other wavelength regions were also employed. In UV region, a frequency-doubled Ar+ laser was used in TLS for detection of nitroaromatic compounds in contaminated water after separation by micellar electrokinetic chromatography at 257 nm [73], or for detection of neonicotinoids at 244 nm [74], and the third harmonics (261 nm) of a mode-locked Ti: sapphire laser has been used for TL imaging of yeast fungus cells [75] and the fourth harmonics (214 nm) was employed in a micro-HPLC-TLS hyphenated system for direct detection of non-labeled amino acids [76]. In the near- and middle-infrared (IR) region, an EDFA combined with an AOTF, tunable from 1500 to 1570 nm, was used for determination

9

of nucleotides [76] and a NIR diode laser for determination of phosphorus [77]. Besides, IR radiation between 4000 and 400 cm^{-1} has been utilized in organic structure determination. With the 934.9 cm^{-1} emission line of a CW CO_2 laser, free fatty acids (FFAs) were determined at concentration levels below 1% [78]. At 1734 cm^{-1} of a CO laser [79], an infrared HPLC-TLS method discriminated fatty acids from higher concentrations of co-eluting noncarboxylic compounds such as longer chain alcohols (octanol, decanol), which show week absorbance at the excitation wavelength.

Though with high sensitivity, laser-excited TLS is still not used for routine chemical analysis due to its low specificity caused by the limited emission lines of lasers available for excitation. It is, therefore, of particular importance that this restriction can be ameliorated. In contrast to the laser beam, another kind of light becoming interesting recently is incoherent light sources (ILSs) with top-hat beam intensity profile [80], which usually have broad wavelength tuning range. ILSs include electric discharge lamps (halogen-tungsten, xenon, and deuterium arc lamps), light emitting diodes (LED), etc. Due to the incoherence and low power of every emission line, only a few works employed this kind of light source in TLS. Bialkowski and Chartier [81] introduced a xenon lamp into a conventional 1-cm sample cell-based TLS and got a detection limit of $\sim 10^{-5}$ AU for pseudo-isocyanine dye in ethanol at irradiance of 7.5×10^3 W/m^2. Then they introduced photothermal spectrometry in small liquid channels, where the TL element is formed by thermal diffusion from the irradiated sample volume through the sample cell walls [82]. The apparatus has been found to work with cells designed to contain sample volumes from 6 μL down to 24 nL.

2.3.1.3 TLS in a flowing medium

In chemical analysis, some analytes are detected in flowing mediums as in the case of liquid chromatography and flow injection analysis. Therefore, TLS in a flowing sample has also been investigated. In Fig. 5, schematic representations of both collinear and crossed-beam TLS configurations in both transversal and coaxial flow modes are shown. Here, "collinear" and "crossed-beam" refer to the optical beam configurations of TLS while "transversal" and "coaxial" express the azimuth between the flow direction of the liquid and the pump beam. Obviously, configuration (d) is the best one from the point of view of absolute TL signal sensitivity and resistivity to sample flow. However, for different sample cell or sample channel structures, such as rectangular or circular cell in macro- or micro-space, other configurations in Fig. 5 also found applications. The crossed-beam TLS configuration is usually used in those cases where the collinear configuration is difficult to realize or the collinear configuration would bring higher noises, such as in CE, where configuration (a) was usually employed [83]. The transversal flow mode is employed only when the coaxial mode is not possible or inconvenient to perform, such as in a microchip, where configuration (b) was used [84], while in an 8-μL flowing cell, configuration (d) was implemented in conventional TLS [85].

(a) crossed-beam TLS in transversal flow   (b) collinear TLS in transversal flow   (c) crossed-beam TLS in coaxial flow   (d) collinear TLS in coaxial flow
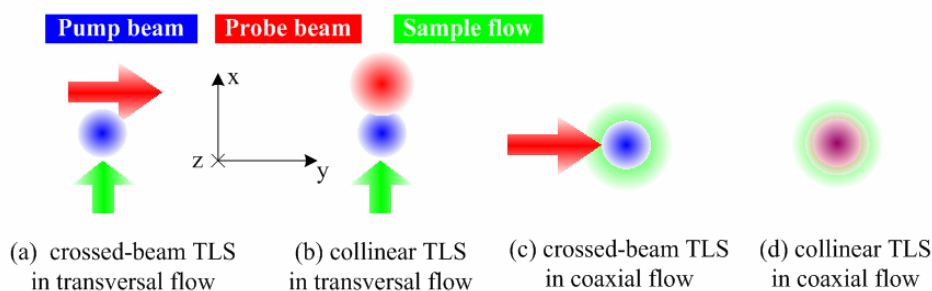
Figure 5: Pump-probe beam configuration for crossed-beam [(a) and (c)] and collinear [(b) and (d)] TLS in transversal flow [(a) and (b)] and coaxial flow [(c) and (d)] modes in a flowing medium.

When the sample flows, the TL signal amplitude is reduced due to the displacement of TL outside the irradiated area, therefore the probe beam has to be displaced for better sensitivity. This is more obvious in configurations (a) and (b) in Fig. 5 than the latter two. For CW excitation, an almost threefold decrease of steady-state TL signal was readily observed when the flow rate was increased from 0 to 0.71 mL/min [86]. The decrease in TL signal is attributed to the decrease of the effective path length. Due to the increased heat transfer associated with sample flows, the effective time constant of the TL is also decreased. It has been demonstrated for CW excitation that the highest sensitivity could be obtained by shifting the position of the probe beam along the direction of the flow [87, 88], while for the configurations (c) and (d), this is not necessary. The loss of sensitivity is much less pronounced in configuration (d). For example, for 1 mL/min flow rate, only 25% decrease in sensitivity was observed in an 8-μL, 1-cm path-length cell [89]. This can be explained by more than one order of magnitude shorter TL time constants compared to the sample residence time. It should be noted that the decrease of TL signal by sample flow is also closely related to the modulation frequency of the pump beam under CW laser excitation or the pulse duration under pulsed laser excitation. In case of pulsed excitation, because of very fast rise time (10 μs) of maximal TL signal, very little variation (few percent) in TL signal was observed for flow rates up to 10 mL/min even in case of transversal flows [90, 91]. Source noise limitations and subsequent poor precision are the main reasons why pulsed TLS is not used for detection in LC and FIA, even though the sensitivity of the technique is not affected by the flow of the sample.

Vyas and Gupta [87] described a theoretical model for flowing samples which is valid for most general conditions. Once the temperature profile is known, the TL signal can be described. In most pump-probe TLS experimental configurations, TL signal is measured as a relative change of the probe beam intensity on the axis of the beam. Under the parabolic approximation, where the TL is treated as an ideal thin lens, the TL signal can be expressed as

$$S(t) = \frac{z_1}{f_x(t)} + \frac{z_1}{f_y(t)}, \tag{5}$$

where z_1 is the distance from the probe beam waist to the sample (Fig. 3). $f_x(t)$ and $f_y(t)$ denote the focal lengths of the "ideal thin lens" in x and y directions (Fig. 5), respectively. In general, an astigmatic lens is formed in the flowing medium. In particular, a cylindrical lens is formed in the case of crossed-beam TLS. The probe beam may be displaced with respect to the pump beam in the x-direction by an arbitrary distance x'. For the collinear TLS,

$$\frac{1}{f_x(t)} = -\frac{\partial n}{\partial T} l \left[\frac{\partial^2 T(x,y,t)}{\partial x^2} \right]_{\substack{x=x' \\ y=0}}, \quad \frac{1}{f_y(t)} = -\frac{\partial n}{\partial T} l \left[\frac{\partial^2 T(x,y,t)}{\partial y^2} \right]_{\substack{x=x' \\ y=0}}, \tag{6}$$

and for the crossed-beam TLS,

$$\frac{1}{f_x(t)} = -\frac{\partial n}{\partial T} \int_{-\infty}^{\infty} \left[\frac{\partial^2 T(x,y,t)}{\partial x^2} \right]_{x=x'} dy, \quad \frac{1}{f_z(t)} = 0. \tag{7}$$

Expressions for $T(x, y, t)$ under excitations of CW and pulsed lasers can be found in Ref. [87].

2.3.1.4 Aberrant nature of TLS and thermal lens enhancement factor

The parabolic model provides a good approximation of the general behavior of TL. However, the refractive index change outside the excitation area is not parabolic. Through consideration of the aberrant nature, a more accurate quantitative description of the TL effect is given by diffraction theory (Huygens principle), which was presented by Sheldon et al. [92], and they

found that in the far field scheme, the TL signal was optimized when the sample cell was located at $\sqrt{3}z_R$ ($z_R = \pi w_1^2/\lambda$: Rayleigh range of the probe beam, with w_1 and λ the beam waist and wavelength of the probe beam respectively) in front of or behind the probe beam waist. Then, Shen et al. brought forward a more general and accurate model for cw laser induced mode-mismatched dual-beam TLS [93]. The model is of simple mathematical expression and convenient to use for both steady-state and time-resolved techniques. When the phase shift of the probe beam caused by TL is very small, an expression for the steady-state TL signal was obtained as

$$S = \left[1 - \frac{\theta_0}{2} \tan^{-1} \left(\frac{2mV}{1+2m+V^2} \right) \right]^2 - 1, \tag{8}$$

where

$$V = \frac{z_1}{z_R} + \frac{z_R}{z_2} \left[\left(\frac{z_1}{z_R} \right)^2 + 1 \right], \; m = \left(w_p / w_e \right)^2, \; \theta_0 = -\frac{P \, \partial n/\partial T}{\kappa \lambda} \alpha \phi l, \; \phi = 1 - \eta \lambda_e / \langle \lambda_{em} \rangle,$$

where z_2 is the distance from the sample to the detection plane (Fig. 3). w_p and w_e are the beam radii of the probe and pump beams in the sample, respectively. m is called the mode-mismatching degree. P is the pump power. k and α are the thermal conductivity and absorption coefficient of the sample. l represents the optical interaction length. When $m=1$, which is the mode-matched dual-beam or single-beam TL situation, Eq. (8) becomes the same form as Sheldon's [92]. In ϕ, $\langle \lambda_{em} \rangle$ is the average wavelength of the fluorescence emission, and η is the fluorescence quantum efficiency, which competes for a share of absorbed excitation energy. When the second-order term is neglected because the value of θ_0 is in most cases smaller than 0.1, and $m=1$ and $V=\sqrt{3}$, then

$$S \sim \theta \alpha \phi l, \tag{9}$$

where

$$\theta = \frac{P \, \partial n/\partial T}{\kappa \lambda}.$$

θ is called "thermal lens enhancement factor", which expresses how much larger or smaller the relative variation of the probe beam is when compared to attenuation of the beam at the measurement wavelength caused by linear absorption. A useful number to remember is that with a He-Ne laser at 632.8 nm as a probe and the excitation power of 4.2 mW in water, $\theta=1$. In other words, the enhancement factor is the ratio of the signals produced from the photothermal lens apparatus to that produced using transmission spectroscopy, assuming that both apparatuses are limited by the same noise sources. The assumption that both signals are limited by the same noise sources is not strictly valid for the excitation-probe apparatus. Nonetheless, the enhancement factor is useful in that it allows comparison of photothermal signals to those obtained using absorption spectrophotometry.

2.3.1.5 Other influencing factors in TLS

1. Change of sample absorbance

When the absorbing species transforms rapidly during the excitation due to photodegradation or other chemical reactions, the changes in absorbance must be considered in the source term. This leads to different time dependencies of the TL signal, depending on the order of the chemical reaction involved [94, 95]. For the case of zero-order reaction, the following expression indicates decrease in TL signal due to disappearance of the analyte (the second

term on the right-hand side):

$$S = \frac{2.303PA}{\kappa\lambda}\left(\frac{\partial n}{\partial T}\right)\tan^{-1}\left(\frac{1}{(1+t_c/t)\sqrt{3}}\right)$$
$$-\frac{2.303PA}{\kappa\lambda}\left(\frac{\partial n}{\partial T}\right)\frac{k_r}{C_0}\left[(t+3t_c/4)\tan^{-1}\left(\frac{1}{(1+t_c/t)}\right)+\frac{t_c\sqrt{3}}{8}In\left[\left(1+\frac{t}{t_c}\right)^2+\left(\frac{t}{t_c\sqrt{3}}\right)^2\right]\right], \quad (10)$$

in which A is the initial absorbance of the sample. When the reaction rate constant k_r equals zero, the expression becomes identical to the case with constant concentration of the analyte with initial concentration C_0. Moreover, the existing theoretical model of thermal lens effect was generalized by Pedreira and coworkers [96] in order to take the time dependence of the absorbance of the sample into account due to the changes in concentration resulting from photochemical reaction and diffusion of absorbing species.

2. Absorption saturation and signal enhancement by transient absorption

Besides, absorption saturation sometimes should be considered. It occurs when populations of a compound are balanced between the ground state and an excited state, coupled together under a strong resonant light illumination. In this case, absorbance A is dependent on the light intensity I. In a simple two-level model,

$$A(I) = A_0/(1+I/I_{sat}), \quad (11)$$

where A_0 is the normal absorbance under a week light illumination condition and I_{sat} $(=h\nu/2\sigma\tau)$ is a measure of the light intensity when the absorption saturation becomes significant. $h\nu$ is the photon energy, σ is the absorption cross-section at the resonant wavelength, and τ is the mean life time of the excited state.

To obtain a large TL signal beyond the absorption saturation limit, the use of transient absorption (optical absorption by molecules in photoexcited states) was employed [97, 98]. The scheme of the signal enhancement is shown in Fig. 6. A high efficiency of photon energy conversion into heat is expected for the transient absorption of visible light. The signal under certain conditions was one or two orders of magnitude larger than that expected from the ground-state absorption. Unfortunately, the measurement of a transient absorption spectrum of the target compound is not easy, especially when the ground-state absorption is in the ultraviolet region and the lifetime of an excited state is smaller than several nanoseconds.
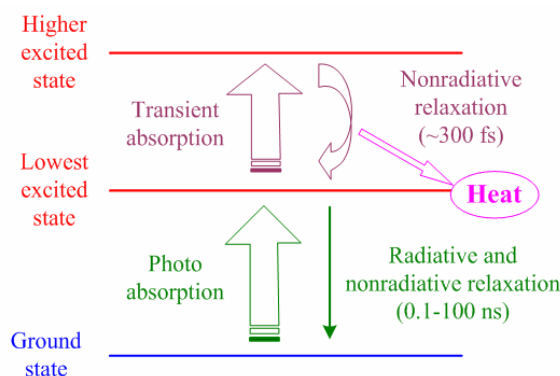
Figure 6: Principle of TL signal enhancement by transient absorption and successive relaxation.

3. Matrix effects and Soret effect on TL signal

Furthermore, the matrix effects on the TL signal should also be taken into consideration, which has been reviewed by J. Georges [99]. The addition of salts, surfactants and polymers in aqueous solutions or the use of solvent mixtures is often needed either to enhance the sensitivity or more generally because such media are required in the separation process prior to TLS detection. In most cases, matrix effects result in small changes in the thermo-optical properties of the solution and small signal variations. However, big signal alterations can arise from the Soret effect. In binary mixtures as well as in solutions with macromolecular species which are initially homogeneous, the temperature gradient can induce the migration of molecules and the formation of a concentration gradient. This results in the formation of a concentration-dependent refractive index gradient which adds to the temperature-dependent refractive index gradient. This combined effect to the change of refractive index can be written as [100]

$$\Delta n(r,z,t) = \frac{\partial n}{\partial T}\Delta T(r,z,t) + \frac{\partial n}{\partial c}\Delta c(r,z,t) , \tag{12}$$

The concentration change can be given by

$$\Delta c(r,z,t) = -S_T c_0 (1-c_0)\Delta T(r,z,t)\Gamma(z,t) , \tag{13}$$

in which

$$\Gamma(z,t) = 1 - \sum_{i=1}^{\infty} \frac{4}{(2i-1)\pi}\sin\left[\frac{(2i-1)\pi}{2}\right]\exp\left[-(2i-1)^2 \frac{t}{t_D(z)}\right],$$

where $t_D(z)=w_e^2(z)/(4D_m)$ is the mass-diffusion time. D_m is the mass-diffusion coefficient. S_T is the Soret coefficient. c_0 is the equilibrium value of the mass fraction of the heaviest component in solution. Time-resolved measurements can help in separating both signal-contributing components and allow to derive mass-diffusion times and mass-diffusion coefficients for a variety of micelles and polymers.

2.3.2 Optimization of TLS systems

To obtain as low LOD as possible, namely the best signal-to-noise ratio, the sensitivity of TLS should be enhanced and the noise level should be decreased. Because TLS is an optical detection technique in, but not limited to, solutions, optimizations were usually realized from three aspects: optical parameters, sample solution and noise.

2.3.2.1 Optical parameters

One of the optical parameters closely related to the TL signal is the power density in the sample, which is determined by the pump beam power and beam radius in the sample. From the definition of enhancement factor [$\theta=P(\partial n/\partial T)/k\lambda$], one of the most direct ways to increase the sensitivity is to increase the power of the pump beam. However, at high powers, nonlinear absorption of light could occur [101], as well as optical saturation [102, 103] and multiphoton processes [104, 105], or the light-induced damage to the analyte especially for some biological molecules [106, 107]. Alternatively, decreasing the pump beam radius can also enhance the TL signal as in TLM described in the next section, but the possible nonlinear absorption or light damage to the analyte should be considered as well. Furthermore, selecting a probe beam with shorter wavelength λ can increase the sensitivity to some extent. Increasing the probe beam power can enhance the absolute TL signal amplitude, but unfortunately, the detector noise induced by the probe beam power instability is also increased proportionally.

Besides, increasing the effective sample length is also a way to increase the sensitivity of TLS.

For certain pump beam parameters (power, beam radius), the second strategy is to optimize the optical configuration of the pump and probe beams. Some papers have presented optimization of the optical configuration to obtain a higher sensitivity. In the far field single-beam scheme, the TL signal was optimized at $z_1 = \pm\sqrt{3}z_R$ [92]. For the dual-beam configuration, Power proposed a near field detection scheme, which enabled a more compact and stable TL measurement and would be less susceptible to the instabilities and drifts in alignment [108]. Li et al. introduced a top-hat beam-excited mode-mismatched TLS based on Fresnel diffraction theory for the sensitivity enhancement of ILS-based TLS [80]. In a flowing medium, Weimer et al. found that in a cross-beam TLS configuration, the optimum signal occurred when the probe beam was located about one pump beam spot size downstream from the pump beam axis [88]. Erskine et al. showed that the effects of flicker noise and shot noise could be reduced by proper choice of pinhole (an aperture-to-beam-size ratio between 0.2 and 0.6) [109]. When regarding CE, Proskurnin et al. applied a near-field transverse TL detector [110], and its optimum configuration (beam sizes, geometry, modulation frequency and flow velocity) was found from the viewpoint of the maximum sensitivity.

2.3.2.2 Thermo-physical properties of sample solutions

As demonstrated in description of the enhancement factor, TL signal is proportional to $(\partial n/\partial T)/k$ ratio. Therefore, choosing an appropriate solvent for the analyte with larger $\partial n/\partial T$ and smaller k will increase the sensitivity. Thermophysical parameters of some materials are listed in Table 3. If the solution is a mixture of two or more solvents, the thermophysical parameters ($\partial n/\partial T$, k) of the liquid, strictly speaking, should be newly measured, but sometimes instead, we can simply take the average value weighted by the mixture composition.

Organic solvents have much higher $\partial n/\partial T$ and lower k than water. Because of this, they have been employed in TLS for sensitivity-enhanced detection of many substances which are not influenced or changed by organic solvents. For example, addition of acetonitrile to the eluent and postcolumn reagent (30% and 60% v/v, respectively) enabled simultaneous determination of Cr(VI) at 0.1 mg/L and of Cr(III) at 10 mg/L levels [111]. The enhancement factor was increased by a factor of 5.4 compared to measurements in an aqueous eluent. Unfortunately, many bioanalytical assays cannot be performed in organic solvents due to denaturation of biomolecules [112].

Room temperature ionic liquids (RTILs) provide a relatively better medium for TLS measurements than water. RTILs can offer at least 20 times higher sensitivity than water and the enhancement could even be adjusted by changing the cation and/or the anion in ILs [113]. RTILs could be used in microfluidic devices to replace either water (to enhance detection sensitivity) or the volatile organic compound (VOC) solvent (to prevent pollution and also to enhance the sensitivity). On the other hand, ILs were shown to cause inhibition of AChE at concentrations of just one percent of IL in aqueous solution, and therefore can not be used for sensitivity enhancement when AChE or similar enzymes are used [10].

Apart from the two methods mentioned above, other possible ways for sensitivity enhancement have also been developed, such as using aqueous micelles [114], reversed micelles [115], crown ethers [116], unique properties of water [117], sample matrix absorption of the probe laser beam [118], or even the latest reported laser-induced precipitation [119].

Table 3: Thermophysical properties of some organic solvents, ionic liquids and solid materials.

Material	k W/m·K	C_P J/g·K	ρ g/cm³	D ×10⁻⁷ m²/s	$-\partial n/\partial T$ ×10⁻⁴ K⁻¹	n	$-(\partial n/\partial T)/k$ ×10⁻³ m/W	S_o g/L	B_p °C	η cP
water	0.598	4.18	1.000	1.431	0.91	1.333	0.15		100	0.894
methanol	0.200	2.53	0.791	0.998	3.94	1.329	1.97	m	65	0.59
ethanol	0.169	2.44	0.789	0.878	4.00	1.361	2.37	m	79	1.2
acetonitrile	0.188	2.23	0.786	1.075	4.50	1.344	2.39	m	82	0.343
acetone	0.161	2.17	0.790	0.937	5.42	1.359	3.37	m	56	0.307
n-hexane	0.120	2.27	0.655	0.807	5.20	1.375	4.33	0.01	69	0.294
toluene	0.131	1.71	0.867	0.886	5.68	1.496	4.33	0.47	111	0.59
carbon tetrachloride	0.099	0.85	1.594	0.731	6.12	1.460	6.18	0.8	76.7	0.901
benzene	0.141	1.74	0.877	0.923	6.52	1.501	4.62	1.8	80	0.652
carbon disulfide	0.149	1.00	1.266	1.173	8.09	1.627	5.43	2.9	46.3	0.363
trichloromethane	0.117	0.96	1.483	0.825	6.03	1.446	5.15	8	61.2	0.542
diethyl ether	0.130	2.37	0.714	0.769	6.06	1.353	4.66	69	35	0.224
ethyl acetate	0.144	1.94	0.900	0.826	4.90	1.372	3.40	83	77	0.426
n-nonane	0.131	2.22	0.718	0.823	4.50	1.405	3.44	i	151	0.668
n-octane	0.128	2.23	0.699	0.822	4.70	1.397	3.67	i	125	0.542
n-heptane	0.123	2.24	0.684	0.801	4.90	1.388	3.98	i	98.4	0.386
n-decane	0.132	2.21	0.730	0.818	4.20	1.410	3.18	i	174	0.92
o-xylene	0.131	1.75	0.870	0.859	5.00	1.505	3.82	i	144	0.812
C_8MImTf_2N	n.d.				n.d.		5.25			
$BMImTf_2N$	n.d.				n.d.		3.90			
$EMImTf_2N$	n.d.				n.d.		2.70			
polystyrene	0.13	1.3	1.06	0.943	1.4	1.6	1.08			
fused silica	1.38	0.75	2.203	8.35	-0.1	1.47	-0.07			
stainless steel	25	0.46	7.9	68.79						

Notes: (1) k: thermal conductivity; C_p: specific heat; ρ: density; D: thermal diffusivity; $\partial n/\partial T$: temperature coefficient of refractive index; n: refractive index; S_o: solubility in water; B_p: boiling point; η: viscosity.

(2) Data (from k to n) of solvents (from water to o-xylene) are from Ref. [48], of ionic liquids (C_8MImTf_2N, $BMImTf_2N$, $EMImTf_2N$) are from Refs. [112] and [113], and of materials (from polystyrene to stainless steel) are from Ref. [120]. Data on solubility, boiling point and viscosity are from wikipedia.

(3) "m", "i" and "n.d." represent "miscible", "immiscible" and "not determined", respectively.

2.3.2.3 Noises

The noises in TLS technique mainly come from two sources:

(1) Light illumination-induced detector noises or inherent electronic noises of the detector and cables such as thermal noise, shot noise, flicker (1/f) noise, in which 1/f noise can be reduced by performing TLS measurement at high modulation frequency. Flicker noise is directly proportional to the light intensity while shot noise increases with the square root of light intensity.

(2) Noise caused by the fluctuation of the relative intensity change (RIC) of the probe beam after the pinhole in the detection plane. On one hand, this may be induced by the pump and probe beams, such as the fluctuation of the pump beam power which can be reduced by real-time recording the power change and subtracting it in TL signal, the mode instability (especially for pulsed laser) and pointing noise of the pump beam, and the power fluctuation and beam pointing instability of the probe beam. The impact from beam pointing instability of the probe beam can be lessened by employing a larger pinhole. On the other hand, the noise can be caused by the convection or flow of the sample, and/or the background absorption of the solution. Therefore, in flowing mode, a stable pump should be used to assure a constant flow in the channel. For the background absorption, selection of appropriate blank or carrier

solution, and/or derivatization reagent if derivatization is necessary, is of particular importance to assure low noises. As demonstrated for the determination of Fe(III) and Fe(II) ions by IC-TLS [68], colorless reagents, for example, 1,10-phenanthroline, were advantageous and provided two and four times lower LODs compared to reagents with relatively high background absorbance.

2.3.3 Analytical applications of TLS

As already described before, TLS detects the optical absorption of the analyte indirectly. Its greatest disadvantage is low selectivity to analytes in the solution. To ameliorate this shortage, TLS has been applied as detection technique for separation methods such as HPLC, CE and IC, and has also been introduced into bioanalytical assays, particularly those relying on FIA.

2.3.3.1 Application of TLS in separation methods

Separation techniques, with their ability to discriminate between several analytes, provide the selectivity to TLS, which in turn offers high sensitivity as well as the ability of probing small volume samples. This makes the combinations such as HPLC-TLS, CE-TLS, and IC-TLS powerful analytical tools. Most recent applications of TLS are related to such hyphenated methods.

One of the applications of HPLC-TLS for determination of carotenoids in complex matrices was the determination of β-carotene in rat and beef livers [121]. The LOD for β-carotene reported in this study was 0.4 mg/L. Guzsvany et al. determined selected neonicotinoid insecticides by LC-TLS [122], with LODs for thiamethoxam (15 μg/L), acetamiprid (3.2 μg/L), and thiacloprid (7.5 μg/L), which are 2.5–8.5 times lower compared to HPLC-DAD. In addition to lower LOD, the advantage of HPLC-TLS is evident in respect of smaller sample size and shorter time needed for its preparation. Hence, the method also found further application in the analysis of samples with complex matrices such as honeys, pollens, and biological tissues as well, contaminated with neonicotinoids at ppb level [123].

Application of TLS in CE enabled determination of 1.8×10^{-7} M dabsylated arginine, histidine, leucine, alanine, glycine, and glutamic acid in a detection volume of 50 pL [124], in which a detection limit of 10 attomoles was calculated. A real application of CE-TLS for analysis of complex samples was reported for determination of etoposide and etoposide phosphate in blood plasma [125]. Based on micellar electrokinetic chromatography and near-field TLS and teniposide as internal standard, this method allowed baseline separation of analytes of interest and potential interfering matrix constituents within 4 min. LODs of 100 μg/L for etoposide phosphate and 170 μg/L for etoposide were obtained, representing a 60-fold improvement compared to a commercial absorption spectrometer operating at 257 nm.

2.3.3.2 Application of TLS in FIA

Flow injection analysis (FIA) is an approach to chemical analysis that is accomplished by injecting a plug of sample into a flowing carrier stream. Compared to batch-mode analysis, FIA offers several advantages related to optimization of analytical procedures, including higher sample throughput, reproducibility, facilitated sample handling and preparation (purification, preconcentration, derivatization, etc.) [112]. In a spectrophotometric method, a significant contribution to the blank uncertainty arises from sample manipulation, where contamination, carryover, and sample cell realignment are likely sources of error when using conventional sample handling techniques. FIA has been advocated as a mean of reducing contamination and carryover in ultratrace analysis with laser-based detectors, such as TLS.

Combination of TLS and FIA is mutually beneficial. The small volume of injection and the

need for sensitivity in FIA are well matched to the TLS capabilities. In this regard, TLS can provide additional improvements in sensitivity and/or sample throughput since there is no need of complete derivatization reactions to achieve sufficient sensitivity, as opposed to less sensitive detection techniques. The FIA provided an elegant mode of avoiding losses of sensitivity or negative systematic errors due to degradation of photolabile analytes, exposed to high-intensity light from excitation lasers used in TLS experiments [126]. Therefore, FIA-TLS is particularly well suited for fast screening of various samples such as pesticides, allergens, and others. The specificity of FIA-TLS can be provided by selective coloring or other reactions (enzyme inhibitions, gene-antigen interactions), which can be performed on-line by using specific reagents in the carrier or by their injections into the FIA system or even by immobilized selective reagents.

The FIA-TLS has been applied for sensitive determination of pesticides in tap water and spiked fruit juices [127]. LODs were obtained for paraoxon (0.2 μg/L) and carbofuran (1 μg/L). In addition, due to its fast response of FIA-TLS, it enabled quasi on-line monitoring (3–5 min time resolution) of degradation processes of OPs [128].

Though TLS has found many applications in conventional chemical analysis, its miniaturized instrument, namely thermal lens microscope, which combines advantages of microscope (small-volume sample, high spatial resolution) with the TL technique (high sensitivity), is more promising, as presented in the next section.

2.4 Thermal lens microscope and microfluidic devices

2.4.1 Principle and development of TLM
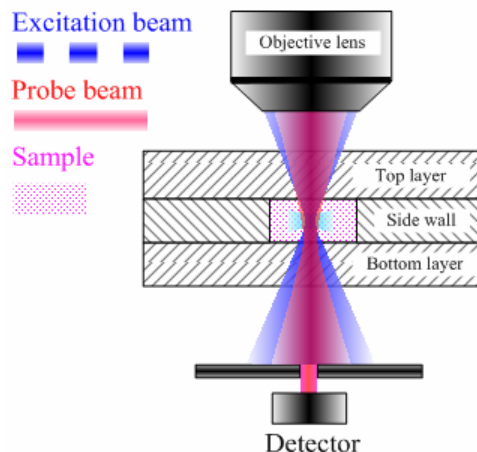
Figure 7: Schematic diagram of a thermal lens microscope.

A promising branch of TLS is the development of microscopic TLS (i.e. thermal lens microscope, TLM), which was brought forward by Harada [129]. TLM is performed on an optical microscope (Fig. 7) in which the optical configuration and formation of TL element are quite similar to the aforementioned general collinear TLS configuration. Wavelength of the excitation beam is selected to coincide with the absorption band of an analyte while wavelength of the probe beam is beyond that band. The excitation laser is tightly focused onto the sample by an objective lens (OL). The diameter of the beam waist is usually ~1 μm. Due to the chromatic aberration or by using a beam expander before the OL, mode-mismatching between the pump and probe beams can be realized. In the far-field detection scheme, the TL signal will be monitored by a photodiode. Besides the high sensitivity inherent to TLS, TLM has exclusive advantages of fast response, micro-space compatibility, high time- and space-resolution imaging and instrumental compactness over conventional TLS. Therefore, TLM

has been applied to a variety of ultrasensitive determinations and imaging studies in microchips or micro sample cells [13].

The TLM described above can be called conventional TLM, for its typical TLS configuration and detection mechanism, i.e. two collinear mode-mismatched lasers are focused into the sample by an OL, and then the probe laser intensity alteration caused by the heat-induced refractive-index change is detected by a photodiode. In addition to this conventional TLM system, to meet special detection requirements or applications, some new TLM apparatuses were developed by changing the pump light source, time resolution or detection mechanism, or by miniaturization which leads to final commercialization.

(1) UV excitation TLM: Hiki et al. developed a UV-TLM with a high-repetition-frequency 266-nm UV pulsed laser for ultrasensitive and nonlabeled detection of nonfluorescent molecules on a microchip [130]. The optimum pulse repetition frequency was at 80 kHz. When combined with LC, fluorene and pyrene were separated in a microcolumn and detected in a capillary with 150 times higher sensitivity than a spectrophotometric method.

(2) Tunable TLM: To demonstrate the applicability of ordinary incoherent light sources in a micro space, Tamaki et al. proposed a laser defocusing TLM detection in a 100-μm microchannel, by utilizing a 250 μm excitation laser beam size in the sample. Excitation with such a large excitation beam size is to resemble an ILS excitation case. They achieved a LOD of 2×10^{-5} AU for Sunset yellow dye in methanol at power 42 mW [131]. Then, a tunable TLS system was developed for microchip analysis [132]. The system utilized a Xe lamp as an excitation source. It could measure the absorption spectrum of a turbid solution without interference from the light scattering background.

(3) Fast time-resolved TLM: A transient TLM [133] was used for fast time-resolved spectroscopy. A femtosecond pulsed laser was used as the light source, and the electron hydration time after three-photon ionization of a water molecule was measured. It showed that the water in a submicrometer channel was about four times more viscous than normal water.

(4) Miniaturized TLM: Yamauchi et al. developed a miniaturized system using TL and fluorescence spectroscopies for microchip chemistry [134]. The system is composed of laser diode modules, fiber-based optics combined with a gradient index lens, and miniaturized detection units for TL and fluorescence signals. The detection limits were 5.6 μg/L for Ni(II) phthalocyanine tetrasulfonic acid and 2.4 μg/L for cy5 (a fluorescent dye from the cyanine dye family), respectively.

(5) Differential interference contrast TLM: When conventional TLM is applied to counting individual nonfluorescent molecules, the low frequency fluctuation of TL signal around 1 kHz caused by the background fluctuation, which results from rapid Brownian motion of the particles and short residence time (several ms) in the focus area of the excitation beam, affects the detection limit to a greater extent than the background signals originating from the solvent, fluorescence, or other sources. To alleviate the background fluctuation, a differential interference contrast (DIC) TLM was developed [135]. In DIC-TLM, the probe beam is separated by a DIC prism into two beams with perpendicular polarization whereas the excitation beam is not separated and it overlaps with one of the two probe beams. Phase contrast appears between the two probe beams due to the difference in refractive index. Then, the probe beams are combined again by another DIC prism, which results in a new polarization component. A background free photodetection is achieved by detecting only this new component as signal after removing the initial polarization component using a polarization filter. The background was reduced to 1/100 by differential interference, and the signal-to-background ratio (S/B) was improved by one order of magnitude, and counting of individual gold nanoparticles (5 nm) was demonstrated by this system.

(6) Commercial TLM: Conventional laboratory-built TLM entails use of large-scale lasers and many optical components, so it is still a large-scale detection system, which has no portability, and needs specialized operator. A commercial desktop-sized TLM (DT-TLM), such as the ITLM-10 shown in Fig. 8, has recently been developed by the Institute of Microchemical Technology Co., Ltd., Japan [136]. The utility of the DT-TLM compared with that of the large TLM has been remarkably improved by simplifying the optics and optimizing the optical configuration. It has excellent characteristics in terms of sensitivity, convenience, and portability as a detector for microchip systems.

Figure 8: A commercial TLM (ITLM-10) from IMT Co., Ltd.

2.4.2 Microfluidic chips

Research and development on downsizing and integration of chemical systems are now a worldwide trend in chemistry. Micro total analysis systems (μ-TAS), also called "lab-on-a-chip", integrate analytical processes for sequential operations like sampling, sample pre-treatment, analytical separation, chemical reaction, and analyte detection in a single microfluidic device. Because of the advantages of microfluidic-based research including low reagent and power consumption, short reaction time, improved control of fluid mixing and heating/cooling, ability to manipulate small particles, droplets and cells, excellent reproducibility and consistency of results due to low Reynolds number, portability for in situ use, low cost, versatility in design, and potentials for parallel operation and for integration with other miniaturized devices, microfluidic chip-based systems have attracted significant attention.

One of the most promising advantages is considerable reduction of the analysis time compared to conventional chemical analysis. There are several characteristic features of the microspace contributing to the short analysis time, for example, short diffusion distance, high interface-to-volume ratio (specific interface area; solid/liquid or liquid/liquid) and small heat capacity. To control molecular transport in the microspace, the molecular transportation time and the specific interface area must be considered. The molecular transportation time is given by [137]

$$t_m = L_m^2 / D_m , \qquad (14)$$

where t_m, L_m, and D_m are the molecular transportation time, diffusion distance and diffusion coefficient, respectively. The specific interface area, σ_m, can be expressed as [138]

$$\sigma_m = S_m / V_m \propto 1/L_m , \qquad (15)$$

where S_m and V_m are the interface area and the volume. Figure 9 shows the scale dependence of the molecular transportation time and the specific interface area. As expressed in Eq. (14), the transportation time is proportional to the square of the scale. Therefore, the transportation takes several hours to a day when the diffusion distance is 1 cm since the diffusion coefficient of typical molecular ions is on the order of 10^{-5} cm^2/s. In contrast with this case, it takes only several tens of seconds when the diffusion distance is 100 μm. The specific interface area of the 100 μm scale microspace is equivalent to that provided by using a separatory funnel with rather vigorous mechanical shaking. These kinds of scale merits become remarkable below the scale of about 250 μm.
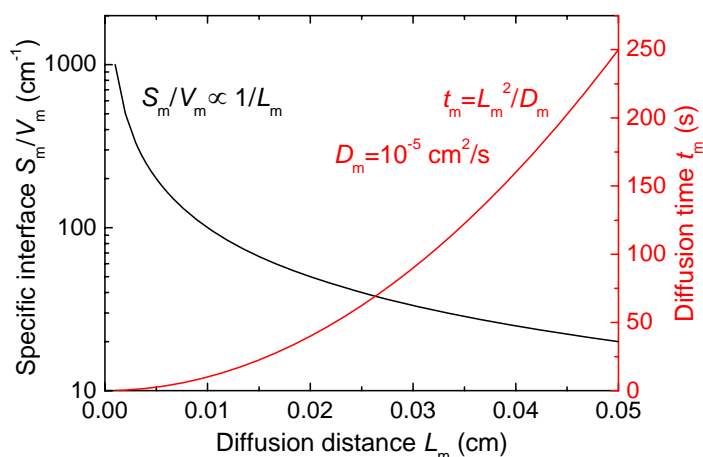
Figure 9: Scale dependence of the specific interface area and diffusion migration time.

According to Fig. 10, a comparison of the immunoassay time between a microtiter plate and a microchip is made. A microtiter plate is usually used in the conventional immunoassay. A labelled antibody must move to the wall in order to react with an antigen on the wall. On the other hand, the liquid phase of the microchannel filled with polystyrene beads is much smaller than that of microtiter plate. The time necessary for the antigen-antibody reaction is greatly reduced. For example, secretory human immunoglobulin A (s-IgA), which is well known as a stress indicator, was assayed with this system, and assay time was dramatically reduced from 15 hours to about 10 minutes [138].
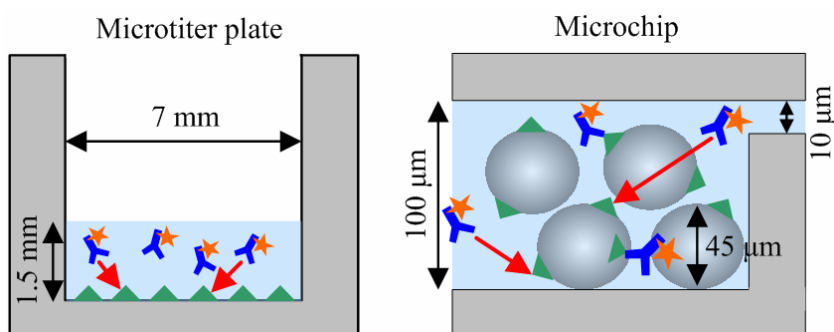
Figure 10: Schematic illustration of immunoassay in microtiter plate and microchip (Drawn according to [138]).

Different channel networks with geometries of interest to a wide variety of applications have been commercially fabricated or developed in laboratory on different optical materials, such as glass, fused silica or polymers [such as polydimethylsiloxane (PDMS)]. The former two materials offer very good pressure capabilities, excellent chemical resistance and optical properties. However, for some applications, such as clinical diagnostics where devices need to be disposable, polymer devices are more suitable than glass devices. Different standard

microchips are easily available such as droplet junction chip, microreactor chip, Y-junction chip and micromixer chip from different companies such as the Dolomite Center Ltd. [139], Institute of Microchemical Technology Co., Ltd. [136], microLIQUID [140], Micronit Microfluidics [141], etc. For special purposes, customized chips are also available.

The flow in the microchannel can be driven by micropumps, which exert pressure on liquids to transport sample/reagents. These liquid molecules can be driven directly or indirectly. Directly-driven micropumps include electrohydrodynamic micropump, electroosmotic micropump, magnetohydrodynamic micropump, surface wave-induced micropump and pressure-driven liquid actuation. Indirectly-driven micropumps include reciprocating membrane micropump, peristaltic micropump, syringe micropump, rotary micropump and bubble-driven micropump.

One of the consequences of the reduction in size of the microfluidic device will be the resulting demands on the detection system. For example, the sample volume in conventional microchannel devices is less than 1 nL and the optical path length is as short as several tens of micrometers, therefore highly sensitive detector should be constructed. Detection methods such as electrochemical detection (EC), LIF, MS and TLM are covered. EC enables detection without labeling and has been used in recent years because of its low cost and sensitivity. Galloway et al. [142] developed an on-column contact conductivity detector for the analysis of various mono- and polyanionic compounds separated by electrophoresis chips fabricated in poly(methyl methacrylate) (PMMA) using hot embossing techniques. LIF is the most widely used. In order to perform high-throughput analysis for DNA digests, continuous analysis of DNA restriction enzyme digest on a microchip was reported with minimal intervention and enhanced time resolution [143]. Although MS enables highly sensitive analysis, the interface between MS and micro channels is still under examination. Tachibana et al. [144] described a robust and simple interface for microchip electrophoresis–MS. The application of TLM for detection of analytes in microchips will be reviewed in the next.

2.4.3 Application of TLM in microchips

For higher sensitivity, Proskurnin et al. optimized the TLM configuration in a microchip [145]. Under the optimum optical scheme design, the LODs of ferroin and Sunset Yellow FCF at 488.0 nm were 5.96 and 1.81 µg/L, respectively (corresponding quantities in the detection volume were 3×10^{-21} and 1×10^{-21} mol). Li et al. developed a collinear-beam TL detector and optimized it with regard to the optical configuration [146]. They introduced it into a HPLC system (mobile phase: 80% methanol and 20% deionized water) to analyze a mixture of five anthraquinone dyes (alizarin, purpurin, quinalizarin, emodin, and quinizarin) and got LODs of 0.5~1.2 µg/L with a pathlength of 200 µm at pump power 28 mW.

By combining microunit operations (MUOs), various chemical processes can be integrated into microchips to create a continuous-flow chemical processing (CFCP) utilizing a multiphase flow network. These MUOs include mixing and reaction, phase separation and confluence of two- and three-phase flows, solvent extractions, solid-phase extraction, heating, concentration, and cell culture. The advantages of the large specific area of liquid–liquid interface and short diffusion distance provided high extraction yields in times one order of magnitude shorter compared to extraction using separatory funnels and mechanical shaking. One example of a liquid/liquid process is the integration of traditional wet chemistry for trace cobalt analysis [147]. The detection limit was 0.13 zmol or 78 chelate molecules. Analysis time was reduced from 2–3 h to only 50 s. Smirnova et al. introduced micro-multiphase laminar flows for the extraction and detection of carbaryl derivative [148], and a LOD of 14 µg/L was obtained. An extremely low LOD was obtained for determination of Pb(II) octaethylporphyrin after extraction into benzene [149]. The LOD of about 74 ng/L (1×10^{-10}

M) corresponds to the average presence of less than one molecule of the analyte in the probed volume (7.2 fL).

The versatility of microchip-based TLM detection offers many other interesting configurations for assays such as microchip-based micro-ELISA applied for the determination of interferon(IFN)-γ [150], and a TLM method for monitoring of intercellular messengers such as arachidonate [151]. In the first case, the polystyrene microbeads precoated with the IFN antibody were placed into a microchip channel. 0.1 ng/mL (6 pM) of IFN could be detected. For the second example, monitoring of the arachidonate released from the rat nerve cells in a culture chamber (0.1-mm-deep, 1-mm-wide and 10-mm-long) on a microchip, was much simpler and required only the injection of glutamate. This stimulated the release of the retrograde messenger (arachidonate), which was detected by TLM at 1.3×10^{-5} M concentration (for injection of 10^{-4} M glutamate) corresponding to 1.3 fmol of arachidonate released per cell.

TLM has also combined with FIA for determination of Fe(II) at an absolute amount of six zeptomoles (in a detection volume of 3 fL) [152]. Solutions of Fe(II) and the reagent were introduced through separate microchannels and transported into the detection area by a capillary action after mixing in a joint channel by molecular diffusion. A similar on-chip FIA-TLM system, with flow rate (0.1–0.2 μL/min) controlled by micro-syringe pump, was used for determination of L-ascorbic acid (AA) and dehydroascorbic acid in urine [153]. A LOD of 17.6 μg/L (1×10^{-7} M) for AA was obtained. The high sensitivity of TLM made the sample preparation simple, and dilutions of the sample up to 100 times reduced the effect of background absorption. Another application of FIA-TLM for analysis of pharmaceuticals was the determination of catecholamines by using on-chip coloring oxidation to aminochromes by sodium metaperiodate, which required only 15 s for completion [154]. LODs for epinephrine, nor-epinephrine, dopamine, and L-dihydroxyphenylalanine are 0.20, 1.20, 0.70 and 0.67 μg/mL, respectively.

2.5 Research goals, methods and scientific significance

Although the thermal lens technique has been extensively developed and applied in various analytical fields, it still doesn't reach maturity and has disadvantages, such as low specificity due to limited laser lines available for excitation, insufficient understanding of TL effect in microspace, limited exploitation of TLM into other techniques (such as FIA, LC) especially for environmental analysis. Therefore, in my research, further investigation of TLS in microspace and promoting its application for environmental analysis with improved sample throughput, sensitivity and specificity are the main research goals.

To achieve the goals mentioned above, a hyphenated technique, namely combined TLM and microfluidic-FIA, will be exploited. Following research aspects will be pursued:

(1) Theoretical modeling and numerical simulation

Novel theoretical models of TLS in microspace will be developed, which consider impacts from parameters such as the flow of the sample, varying excitation beam size within sample, effects of top/bottom layers and side walls. Numerical simulations, which would provide a theoretical guideline for the optimization of TLM in experiments, will be carried out as well.

(2) Experimental setup and analysis

This part will include construction of a laser and a broad-band light source (Xe lamp)-excited TLMs, and study of the TL signal in microspace under different parameters (optical

configuration, state of sample — static or flowing) to verify the theoretical models and optimize the system to achieve lower detection limit.

(3) Applications

As a step towards practical applications, a microfluidic-FIA-TLM setup will be constructed to demonstrate the advantages of microfluidic-FIA-TLM in some previously studied and optimized analytical procedures such as detection of Cr(VI).

Performing the proposed research is expected to bring the following new contributions to science:

(1) Better understanding of basic photothermal phenomena in micro space and flowing systems under different excitation modes (Gaussian, top hat).

(2) Novel methods for fast and high throughput chemical analysis with low cost and low sample/reagent consumption when combined with miniaturized microtiter plates and/or microfluidic-FIA devices.

(3) Improvement of the specificity of TLS. The TLM with ILS excitation would inherit the advantage of tunability like in transmission absorption detection, which makes it possible to directly detect various compounds with low-cost multiwavelength light source. A wide tunability may eliminate the possible problems of derivatization especially for small molecules.

3 EXPERIMENTAL

One major objective in this research is to build novel TLM systems. In this chapter, a laser-excited TLM, an ILS-excited TLM, as well as a conventional TLS setup, are presented, and the optical, mechanical and electronic/electrical components or devices used for building these systems are described. The analytes or reagents for experiments are given as well.

3.1 TLM systems and related components

Due to the advantages of lasers (high power, good coherence and directionality) over other light sources, at present, laser is still the first choice as the excitation source for TLS. In the first part of my experiments, a laser was used as the excitation source to build a laser-excited TLM. At the same time, a conventional TLS system was also employed for some experiments. On the other hand, with purpose of paving a way or providing some idea for later TLS development with better specificity, a xenon lamp was used to build a so-called ILS-excited TLM, in which the term "microscope" is used for two reasons: (1) as opposed to the conventional TLS usually working with a 1-cm sample cell, this system would find applications in microchips or microwells with sample length of ~100 μm; (2) the main body of the system is similar to conventional microscope as well as to laser-excited TLM where this term is already well established.

Figure 11(a) gives schematic diagrams of a laser-excited TLM and a conventional TLS setup used in this work. In Fig. 11(b), an ILS-excited TLM is shown. Double-arrow lines in the Figs. 11(a) and 11(b) mean that the lenses can be moved forward or backward to change the pump or probe beam parameters, or the carrier syringe can be moved upward or downward to change the height difference with respect to the waste syringe.

In the laser-excited TLM, a pump beam from an argon ion laser is reflected by mirrors to beam expander II, which consists of two lenses L3 and L4 and is used to change the focusing radius and position of the pump beam in the sample. Then after passing a chopper, it is combined by a dichroic mirror with a probe beam from a He-Ne laser which first passes an optical isolator (composed of P1 and W1) and beam expander I, which consists of two convex lenses L1 and L2. Then both beams propagate coaxially through an OL, and further through a sample cell where the TL effect is generated, and the probe beam is diffracted by the TL effect and after a collecting lens its central intensity is monitored by a photodiode mounted behind a pinhole. The sample cell can be a simple well for batch-mode measurement, or a complex microfluidic chip for lab-on-a-chip analysis. A gravity-driven pump was incorporated into the TLM to provide liquid flow for microchip.

When a folding mirror M7 is turned to 45° position, the pump laser will be delivered to a conventional TLS setup. After passing a chopper and a focusing lens L9 (focal length can be changed by using different lenses), it is aligned coaxially with a probe beam from a He-Ne laser (Uniphase) after beam expander III which consists of two lenses L6 and L7, and a focusing lens L8 (10 cm focal length or other values to get different w_1s). The two beams go through a sample cell (1 cm quartz cell) and the TL signal is detected by a photodiode mounted behind a pinhole.

In the ILS-excited TLM, a xenon lamp is used as the source of pump beam which is guided into the TLM by an optical fibre, and a bandpass filter is used to filter the ILS. After a wide-band dichroic filter, the ILS is aligned with a He-Ne laser beam after an optical isolator (composed of P2 and W2) and beam expander IV (composed of three lenses: L10, L11 and L12). Then, the ILS is focused by an OL to about 107 μm at the waist. The probe beam

travels through the OL collinearly with the pump beam from the ILS and after probing the TL element and passing two filters and a pinhole, its axial intensity is detected by a photodiode.

Figure 11(c) gives a picture of the laser-excited TLM built in laboratory.

(a)

(b)
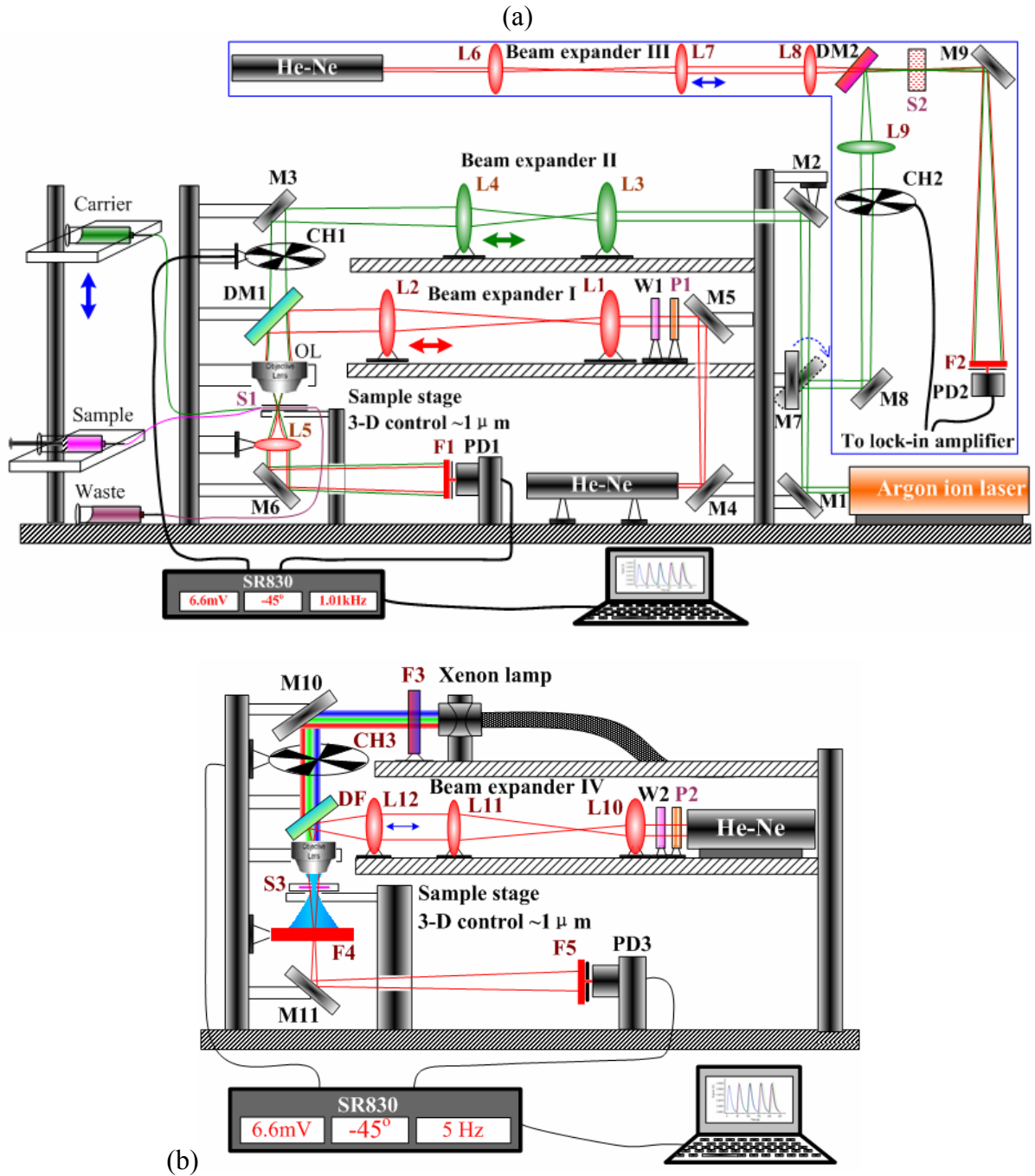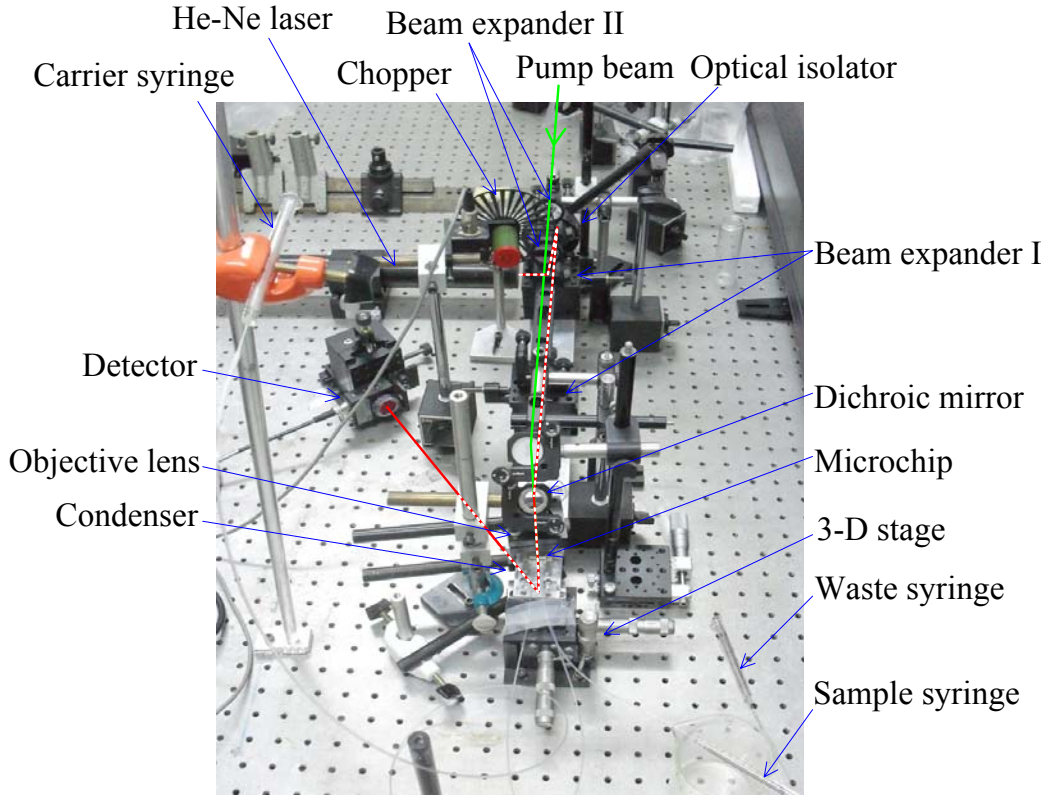
(c)

Figure 11: Schematic diagrams of (a) two TL setups: a laser-excited TLM (side view) and a conventional TLS setup (confined by blue line, top view), and (b) an ILS-excited TLM (side view). L1-L12: lenses; M1-M11: mirrors; F1, F2, F5: interference filters at 632.8 nm; F3: bandpass filter; F4: red filter; DM1, DM2: dichroic mirrors; DF: wide-band dichroic filter; S1, S2, S3: sample cells; PD1, PD2, PD3: photodiodes; P1, P2: linear polarizer; W1, W2: quarter-wave plate at 632.8 nm. (c) Photography of a laser-excited TLM system.

It should be noted that the TL signal strongly depends on the modulation frequency. For continuous laser excitation, we usually choose a frequency at which the excitation duration in a modulation cycle is about 100 times larger than that of the thermal time constant [$t_c=a_e^2/(4D)$, with a_e the pump beam waist radius and D the thermal diffusivity] [48], to obtain a relatively high detection sensitivity. This can be written as

$$\frac{1}{2f} > 100t_c, \tag{16}$$

The frequency can be selected according to

$$f < \frac{1}{200t_c}. \tag{17}$$

On the other hand, the LOD of TLS is also restricted by the noise level of the detector at different frequencies. The lower the frequency, the higher noise will be. Therefore, to select a proper frequency for a specific TLS, a compromise should be made between the detection sensitivity and noise to achieve a low LOD. For ~1 μm beam excitation in laser-based TLM, 1 kHz is suitable, at which a high signal to noise ratio can be assured because of the low electronic noise of the detector at high frequencies. In this laser-excited TLM, 1.01 kHz was used to avoid any electromagnetic noise from the high order AC harmonic frequency of laboratory electrocircuits (50 Hz). For conventional TLS with excitation beam radius of 30 μm in a l-cm sample cell, a frequency of about 30 Hz is chosen. For ILS-excited TLM where

the pump beam radius in the sample is around 100 μm, a modulation frequency of 5 Hz was used.

The detailed information of the components used for these TLS systems are listed as follows:

(1) Pump beam: An argon ion laser (514.5 nm, Innova 90, Coherent Inc.) was used in laser-excited TLM. Beam waist of the argon laser was measured to be 426 μm. A xenon lamp (HPX2000, Ocean Optics) was used in ILS-excited TLM. For the xenon lamp, an optical fibre with core diameter of 350 μm was used to guide the light out from the lamp chamber. At the end of the fibre, a collimating lens (CL) with focal length of 12 mm was used to collimate the light beam.

(2) Probe beam: A linearly polarized He-Ne laser (632.8 nm, 5 mW, linear polarization >500:1, 25-LHP-151-230, Melles Groit) was used as the probe beam in laser- and ILS-excited TLMs. Its beam waist was measured to be 389 μm. A randomly polarized He-Ne laser (632.8 nm, beam waist 400 μm, Uniphase) is used for the conventional TLS setup.

(3) Reflectors, lenses and mirror mounts: High reflection dielectric mirrors (99.8% at 45° from 400-700 nm, Thorlabs Inc.) and lenses with different focal lengths from 15 to 200 mm were mounted on two-D mirror mounts (KM100, Thorlabs Inc.) or lens mounts (FMP1, Thorlabs Inc.) to reflect or focus the probe/pump beams. In Table 4, focal lengths (f_L) of different lenses used in TLS/TLM systems are given.

Table 4: Focal lengths of different lenses used in TLS/TLM systems

Lens num.	L1	L2	L3, L10	L4, L6, L12	L5	L7	L8, L9	L11	OL	CL
f_L (mm)	40	150	30	50	15	100	40-120	200	8 or 15	12

(4) Optical isolator: An optical isolator, which consists of a linear polarizer (LPVISE100-A, Thorlabs Inc.) and a λ/4 waveplate at 632.8 nm (WPMQ05M-633, Thorlabs Inc.), is used to block any possible reflected probe beam back into the laser cavity. In Fig. 12, the optical isolator is shown. The linear polarizer and the waveplate should be located in parallel and as closely as possible to ensure the best isolation performance. First, adjust the polarization direction of the linear polarizer to an azimuth where the transmission of the probe beam after the polarizer is the maximum, and then by rotating the waveplate the reflected stray light can be greatly suppressed.
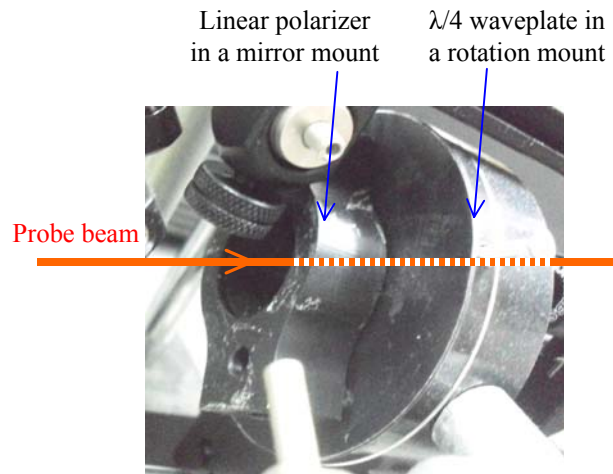
Figure 12: Optical isolator for avoiding the reflected light back into the probe laser cavity.

(5) Bandpass filter: A bandpass filter (pass from 310-710 nm and cut-off from 200-300 and 800-1800 nm, FGS900, Thorlabs) is used to filter the ILS.

(6) Stage for beam expanders: To hold an beam expander for the probe beam, a stage was fabricated and an array of M4 holes were drilled on an aluminum plate as shown in Fig. 13(a). For the pump beam, a small optical rail (RLA300/M, Thorlabs Inc.) was used to hold its corresponding beam expander.

(a)   (b)
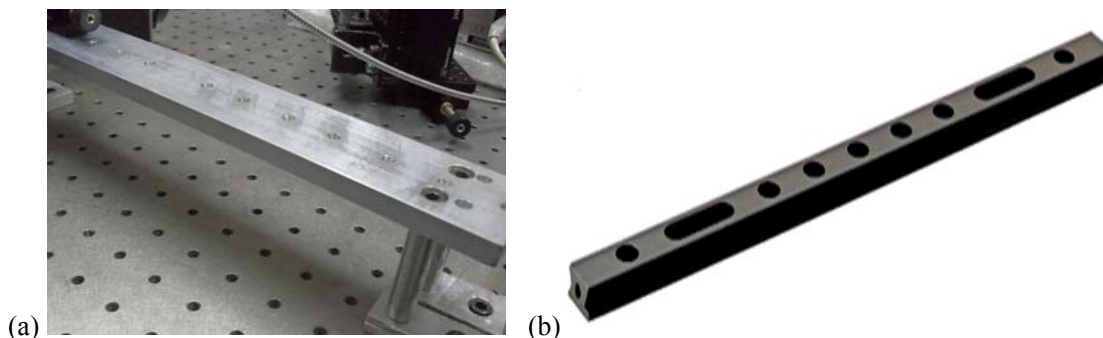
Figure 13: (a) A home-made stage and (b) an optical rail.

(7) Dichroic mirror: A low-pass wide-band dichroic mirror (transmission at 45° from 400-580 nm, reflection at 45° from 620-780 nm, NT69-204, Edmund Optics). Its transmission spectrum was measured with a spectrophotometer, and is shown in Fig. 14.
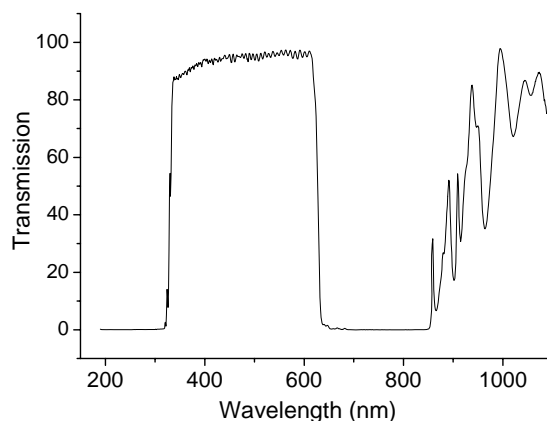
Figure 14: Transmission spectrum of a wide-band dichroic mirror used in this work.

(8) Objective lens (OL): The OL was put on a mirror mount to adjust its tilt with respect to the incident beam. A 20×/NA 0.40 OL (Olympus Inc.) with long working distance 5 mm and a 15 mm-focal length lens were used as OLs.

(9) Sample cell: Sample cells with optical lengths of 10 μm, 100 μm and 1 cm (Starna Cells, Inc.); a microfluidic chip (microchannel: 205 μm wide × 100 μm deep, Y-junction, The Dolomite Centre Ltd., UK), with one Y-junction channel and two straight channels. The inlets (I1, I2, I3, I4) and outlets (O1, O2, O3, O4) of the chip are numbered from bottom to top as shown in Fig. 15(b). Area of the cross section of the microchannel [Fig. 15(c)] was calculated as 0.016 mm^2.

Figure 15: (a) Schematic presentation of 10 and 100 um sample cell from Starna Cells, Inc, (b) Y-junction chip from the Dolomite Centre Ltd., (c) shape of the semicircular channel on the chip, (d) parameters of a 100-µm sample cell and (e) parameters of the microchannel.
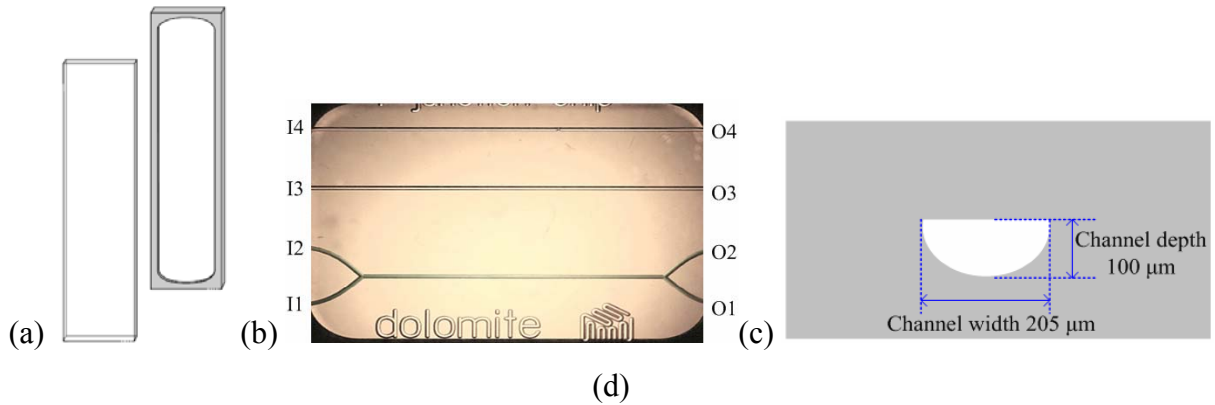
Path length mm	Exterior, mm			Sample chamber, mm			Nominal Vol mL
	Width	Length	Height	Width	Length	Height	
0.1	12.5	2.6	45	8	0.1	40	0.03

(e)

Internal channel cross-section (depth × width)	100 mm × 205 mm
Channel length between Y-junctions	12.5 mm
Volume between Y-junctions	0.2 mL
Channel length of straight channels	22.5 mm
Volume of each straight channel	0.36 mL
Back pressure with 100ml/min flow (water) through one of the straight channels	0.05 bar
Surface roughness of channels (Ra)	5 nm
Chip top layer thickness	2.0 mm
Chip base layer thickness	2.0 mm
Operating pressure	30 bar
Operating temperature	150 ^{o}C
Material	Glass
Fabrication process	HF etching and thermal bonding

To investigate the TL signal under excitation of a divergent pump beam and to find the optimum systematical parameters for a certain sample cell and/or a certain pump beam profile, cells of different sample lengths were employed. Besides the standard sample cells of 10 and 100 µm, to get different sample lengths, a wedge-shaped cell was formed by stacking two quartz plates together as drawn in Fig. 16(a). The depth of the interspace can be adjusted by choosing the height ΔH of a spacer marked in green in the figure. However, it should be noted that ΔH should be very small to avoid the influence of the unparallel surface of the interspace on the TL signal. Here, ΔH=0.3 mm was used to obtain sample lengths of less than 200 µm. To get sample lengths over 200 µm, a sample well sandwiched by two parallel quartz plates was formed by putting two spacers, like shown in Fig. 16(b). The spacer was made by stacking multiple pieces of cover glass (150 µm per piece), and its thickness, which is calculated as $n\times150$ µm (n=1, 2, 3, …, is the number of cover glass), determines the sample length between the two plates.
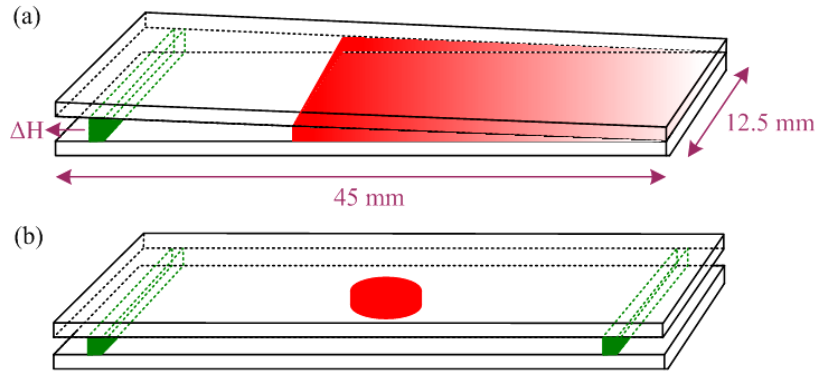
Figure 16: (a) A wedge-shaped sample cell with different sample lengths available; (b) a sample cell sandwiched by two parallel plates.

To investigate the impact of surroundings on the TL signal in ILS-excited TLM, a sample well of Ø 4 mm× 4 mm, as shown in Fig. 17(a), was made out of a Pyrex glass plate to hold the two-layer solutions. The bottom of the well is a piece of 170-μm cover glass, which was glued onto the back of the plate. Similarly, a "T"-shaped sample well was also made for holding the three-layer solutions, as depicted in Fig. 17(b). In this case, the top well of Ø4 mm × 2 mm is used for accommodating the top and sample layers while the bottom well of Ø1.5 mm × 2 mm is for holding the bottom layer. Due to the surface tension of the liquid, the small bottom well can hold the bottom layer even if the density of bottom layer is lighter than that of the sample.
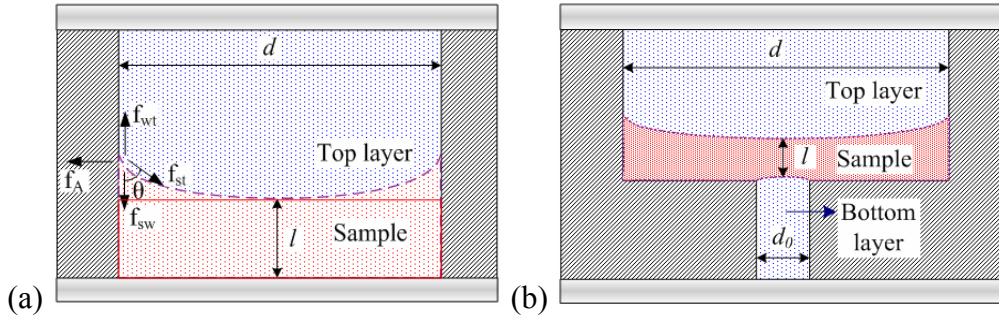
Figure 17: Schematic charts of (a) a two-layer sample well and (c) a three-layer sample well.

Inside the two-layer sample well, if the top layer is air, due to the surface tension, the surface of the sample is curved, like the dashed line in the graph. At the intersection of the sample, top layer and the wall, a balance of forces is reached among the adhesive force (f_A), the sample-wall surface tension force (f_{sw}), the sample-top layer surface tension force (f_{st}) and the wall-top layer surface tension force (f_{wt}). Under the balance, a contact angle between f_{st} and f_{sw} is formed. In our experiment, the parameter of interest is the sample length l, which determines the TL signal. If we inject a sample with volume V_I, the real value of l in the centre of the well is less than V_I/A, where $A=\pi(d/2)^2$. The volume can be expressed as

$$V_I = V_l + \Delta V = \pi \left(\frac{d}{2}\right)^2 l + \Delta V , \qquad (18)$$

ΔV is the volume difference between V_I and V_l.

If the top layer is organic solvent, the curvature will become smaller because of the gravity of the top layer. The surface of the sample would approach a plane if both the thickness and the diameter of the well are not very small. In this case, ΔV is very small and l can be estimated by the injected volume. However, if the sample thickness is very thin in center, l cannot easily be determined. Because the sample, which is injected manually, is not uniformly distributed

31

in the well, it is very difficult to control and to know the sample length precisely especially for the three-layer system. In this situation, a method which correlates TL signal ratio at two discrepant modulation frequencies and the sample length was used for the estimation of the sample thickness (stated later).

To prepare a three-layer system in the sample well, the following procedure was employed:

(1) Clean the sample well with ethanol and water, and then dry it with a fan;

(2) For the preparation of three-layer sample system, first put the plate with T-shaped well on a horizontal plane and then follow the five steps as shown in Fig. 18(a).

Step 1: inject a certain amount of octane into the bottom well with a 50-μL syringe. Considering the evaporation of octane, the injected volume should be a little bit larger than that of the bottom well, such as 4 μL versus 3.53 μL for a bottom well of Ø1.5 mm × 2 mm.

Step 2: inject a certain amount of ferroin (such as 6 μL) into the bottom of the top well. Stir the sample slowly with the needle of the syringe to make it spread out in a shape like in the figure.

Step 3: inject a certain amount of octane (such as 20 μL) into the top well.

Step 4: use a 10-μL syringe to suck a certain amount of sample out of the well. Suction should be performed first at peripheral area until the sample is located only in the center, namely the mouth of the bottom well. Then suck a small amount of sample from the mouth of the bottom well, until the colour of the sample approaches that in a 100-μm sample cell. Judgement of the sample thickness by colour is very rough and only suitable for sample with high concentrations (such as 1 mM ferroin). A more accurate method for sample thickness determination by TL signal will be introduced in section 4.3.3.1. A better way is to perform this step under a microscope with a long working distance OL, where the syringe needle can be precisely located in the well and the interface between octane and ferroin can also be inspected. By virtue of a microscope, it is much easier to obtain the desired sample thickness.

Step 5: inject excess octane into the mouth of the top well from one side and simultaneously seal the mouth by moving a cover glass from the other side. Air bubbles should be kept out of the well during the process.
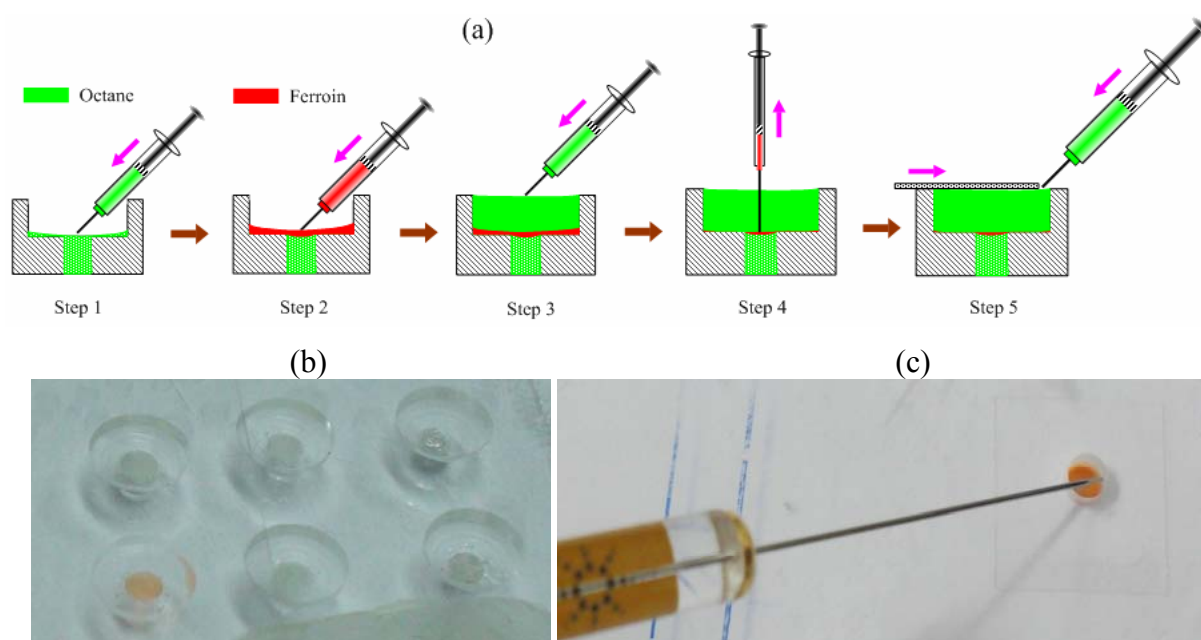
Figure 18: (a) A schematic graph for preparing the three-layer sample system, and photographs of (b) three-layer and (c) two-layer sample systems.

(3) Clean the top and bottom cover glass to avoid any interference with the pump and probe beams in TLS. Check the sample thickness with the method introduced in section 4.3.3.1. If the sample thickness is larger than the desired, repeat steps 4 and 5 in Fig. 18(a), otherwise repeat the whole procedure. A photograph for a three-layer system is presented in Fig. 18(b).

(a)   (b)   (c)
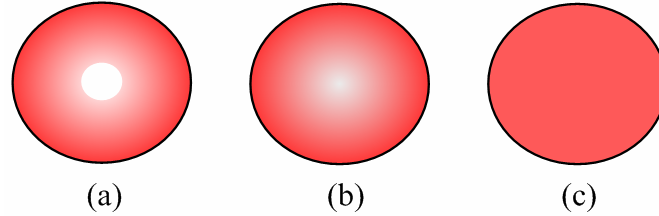
Figure 19: Sample distributions in the well when inject different volumes of sample: (a) the center is not covered by the sample, (b) the center is covered by a very thin layer of sample and (c) the sample is nearly homogeneously dispersed.

For the preparation of two-layer sample system, the procedure is similar except that the step 1 in Fig. 18(a) is eliminated. During the preparation [Fig. 18(c)], it was found that when injecting 4 μL or less, the sample did not spread evenly over the well bottom surface, like in Fig. 19(a); if the volume was increased to 5 μL, the surface was covered similarly to Fig. 19(b) due to surface tension. If the injection volume reached 6 μL, the sample tended to be uniformly distributed [Fig. 19(c)] though its surface is still curved near the sidewall.

(10) Mount for the sample: A sample stage with x-y-z control (17AMB003/MD, CVI-Melles Groit, resolution 1 μm) was used to realize precision adjustment. To fix the sample on this stage, a mount for the sample cell [Fig. 20(a)] and a mount for the microchip [Fig. 20(b)] were home made.

(a)   (b)
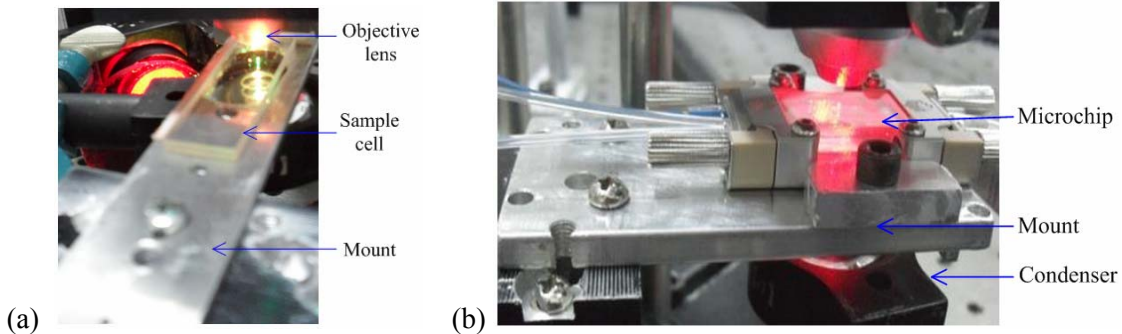
Figure 20: (a) A mount for the sample cell, and (b) a mount for the microchip.

(11) Beam condenser: To collect the divergent probe beam under the OL, a beam condenser (L5) which is composed of two stacked lenses with focal length of 2.5 and 4 cm respectively, was used.

(12) Red filter and interference filter: A red filter and a narrow-band filter at 632.8 nm with FWHM of 1 nm were used to block the pump beam and other interferefering light sources.

(13) Detector: A home-made pinhole (250 μm, 700 μm, 1 mm, 1.8mm and 4 mm in diameter or other size) was fixed in front of a non-biased photodiode or a biased photodiode (PDA36A, 8-level gain adjustment, 10 dB per step, Thorlabs Inc.), which was mounted on a two-D stage (Model 2492, CVI-Melles Groit).

From Figs. 21(a) and 21(b) we can see that the power response of the photodiode PDA36A is linear with the light power, but the non-biased PD shows nonlinear behavior. At the higher end of the investigated power range, the response of PDA36A is about 9 times higher than that of the non-biased PD with respect to the same incident light power. Though the response

33

of the non-biased PD at low light power, such as at μW level, is high, it is not applicable because the corresponding AC intensity change caused by TL element is very low. Therefore, in all TLS systems used in this work, PDA36A was chosen as the detector. The detector has a relatively large responsivity at 632.8 nm, which is about 0.4 A/W according to the specification of the detector. In addition, background signals of the detector (i.e. no probe beam illumination) at different gains were checked, as shown in Fig. 21(c). This is quite important when we compare the TL signals at different pinhole sizes. TL signal is defined as a ratio of the relative intensity change of the probe beam (S_{ac}) to the probe beam intensity before excitation (S_{dc}), in which S_{dc} can be calculated by subtracting the background signal (S_b) at certain gain from the measured voltage (S_{dc0}) recorded by a multimeter. In Figs. 21(d) and 21(e), background noise levels of PDA36A at different gains are given at 1.03 kHz (laser-excited TLM case) and 5.5 Hz (ILS-excited TLM case). The background noise should be considered when analyzing the noise in a TLS system or choosing appropriate pinhole size and/or gain for achieving maximum signal-to-noise ratio in that system.
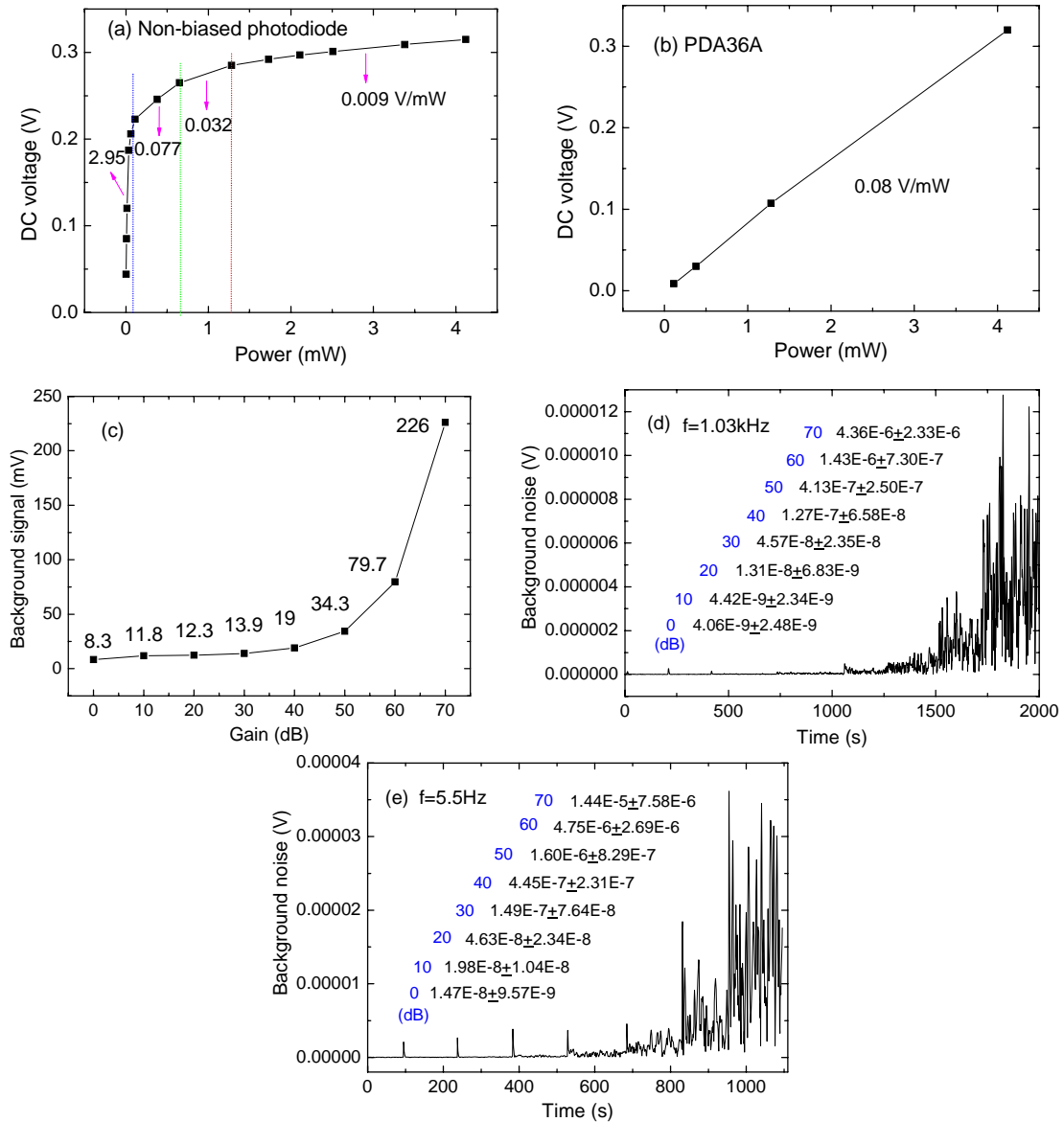
Figure 21: Power response of (a) a non-biased photodiode previously used in our lab and (b) a Si photodiode PDA36A. (c) Background signal of PDA36A measured by a multimeter at different gains and corresponding noise levels at modulation frequencies of (d) 1.03 kHz and (e) 5.5 Hz recorded by a lock-in amplifier.

(14) Gravity-driven pump: Due to the lack of microsyringe pump, a pump driven by gravity was fabricated. It was used in microfluidic-TLM and microfluidic-FIA-TLM setups to drive the sample and carrier through the microchip.

The procedure of fabrication of this pump is as follows:

(1) To obtain a relatively stable flow in the channel, proper syringes were chosen as the carrier and waste reservoirs. According to the US patent "Microfluidic gravity pump with constant flow rate" [155], some tips should be given attention: 1) The reservoir should has an aspect ratio [length/inside diameter (ID)] of at least 5:1, preferably 10:1 or even 100:1; 2) Tubings with nominal diameters between 3.5 mm and 4 mm were found to be well suited as a reservoir; 3) The outlet reservoir is preferably of the same size, material and geometry as the supply reservoir.

Therefore, two 500 μL syringes (Hamilton) without plungers were selected as the carrier and waste reservoirs and two PEP tubings (VICI AG International) with length 70 cm and ID 750 μm were used to connect the carrier/waste syringes and the microchip. On the other hand, micro syringes with volumes of 10 μL, 50 μL and 100 μL (Agilent Technologies, Hamilton) were used as the sample injector, and a PEP tubing (VICI AG International, length 25 cm and ID 500 μm) was selected to connect the sample injector and the microchannel.

In Fig. 22(a), the connection of microchip and tubings is shown: the tubing from the carrier was connected to I2 [Fig. 15(b)] and the tubing from the sample was connected to I1; the tubing to the waste was connected to O1, and O2 was sealed. This connection is suitable for the initial experiments on ferroin as the sample. Because there is no reaction, the sample can be detected in the microchannel (length 1 cm) between the two Y-junctions. In this case, the sample was filled in the carrier reservoir and then it went through the carrier tubing, through the microchannel and to the waste reservoir at last.

If there is a reaction in the microchip and the reaction is not completed in a few seconds, it is better to detect the product in one of the straight channel to assure a good signal shape because the channel between the two Y-junctions on this microchip is only 1 cm. In this case, an extension loop (length 15 cm, ID 200 μm) was used to connect O1 to O3 (or O4) and the tubing to waste was changed to I3 (or I4) correspondingly, as employed in the later Cr(VI) detection. For simplicity, the former connection without extension loop will be called "Connection I" and the latter "Connection II". When a microchip with longer channel behind the Y-junction is available or the reaction can be completed in 1~2 seconds, the extension loop could be discarded.

(2) One syringe was clamped on a pole to a certain height, and the other was put on the optical table. Both two syringes were kept horizontally to assure a constant pressure difference when the flow went from the carrier syringe to the waste one. To make the flow run continuously in the channel, any bubbles were avoided or eliminated before experiments. Then a steady flow could be obtained.

In Fig. 22(b), flow velocities of water in the microchannel at different height differences for Connection I are given. We should note that the flow rate in the microchannel is not only related to the tubing connection and the height difference, but also to the physical properties (density, viscosity) of the fluid in the channel. For another fluid with different density and/or viscosity, the flow rates at different heights should be newly measured.
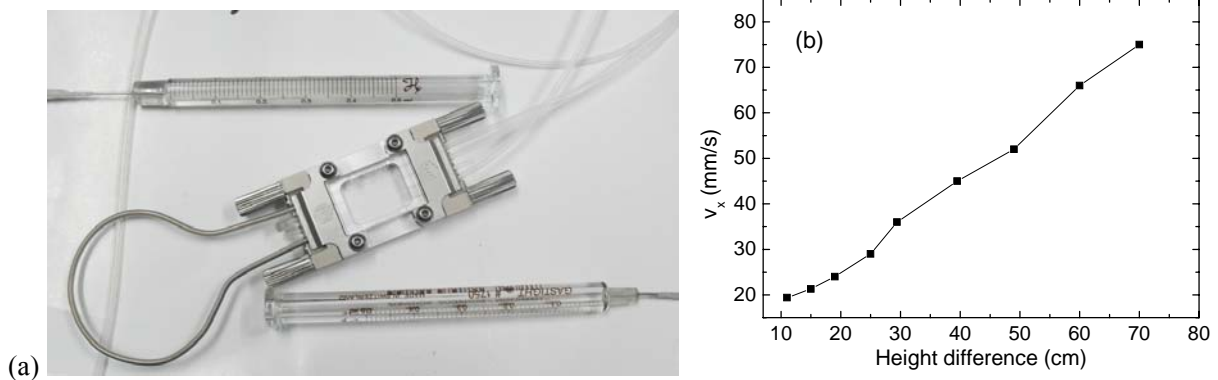
Figure 22: (a) Microchip and syringes for gravity-driven flow, and (b) flow velocities of water in the microchannel at different height differences for the left tubing connection (the carrier tubing is blocked).

(15) Mechanical chopper: In a mechanical chopper (300 CD, Scitec), blades with different number and consequently large or small clear apertures were used to modulate the pump beam at low or high modulation frequencies.

When using a mechanical chopper to modulate the pump beam, the duty cycle would be different if the ratio of the pump beam size and the aperture changes. Such as in Fig. 23, three different profiles are given.
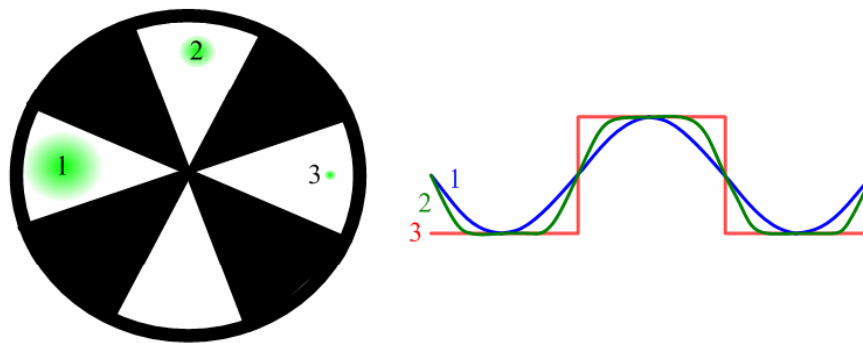
Figure 23: Modulation profiles of the pump beam for three different ratios of the beam size to the slot dimension of the chopper.

From the circuit theory [156], an alternating current expressed as the root-mean-square (rms) value produces the same heating in a resistor as that produced by a direct current of the same magnitude. Thus, the rms current is important in power calculations. $I_{rms}= 0.707I_p$, with I_p the peak amplitude of a sinusoidal alternating current. For sinusoidal modulation of the laser, the rms power density in the sample is: $Q_{rms}=0.3535P/\pi a_e^2$; while for square-wave modulation with duty ratio of 0.5, $Q_{rms}=0.5P/\pi a_e^2$. Therefore, the heat produced in a modulation cycle under square-wave modulation would be 1.41 times higher than that under sinusoidal modulation. Therefore, in laser-excited TLM, the outer part of the chopping blade was positioned at the focusing point of the Lens 3 in beam expander II (Fig. 11), and in ILS-excited TLM, a two-cycle blade with large clear aperture was used.

(16) Lock-in amplifier: SR830 (SRS Inc.) was used with time constant set to 1 s and low-pass filter slope at 24 dB/octave.

(17) Power meter: FieldMaster™ Power/Energy Meter (Coherent Inc.) was used. If the light intensity is measured at single wavelength, the power can be measured by the power meter after setting the instrument to a correct wavelength. However, if a broad-band light intensity is measured, both the relative irradiance spectrum of the light source and the response factor

of the power meter should be known to obtain the real total power. The real total power of the ILS and its equivalent power at certain wavelength will be calculated for illustration.

In Fig. 24, the irradiance spectrum $I(\lambda)$ of the xenon lamp, as well as the absorption spectrum $\alpha_s(\lambda)$ of 10 μM ferroin solution, is shown.
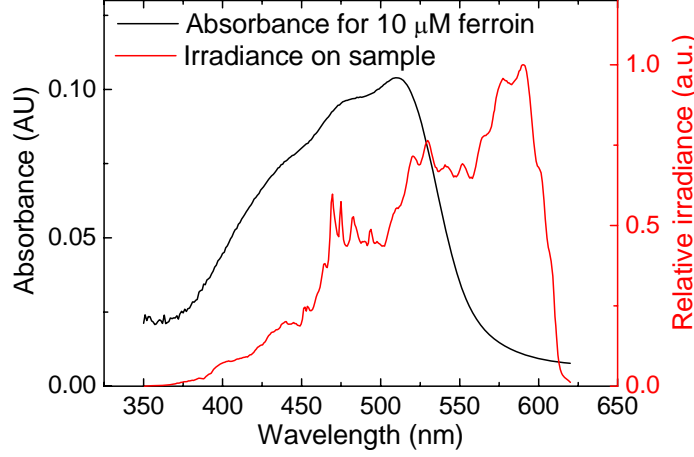
Figure 24: Relative power spectrum of the ILS after the OL and absorption spectrum of 10 μM ferroin.

In Fig. 25, the response factors $R(\lambda)$ of the power meter to light at different incident wavelengths are given. With respect to the same ILS excitation on the detector's head, the displayed power values on the power meter panel were recorded by setting the instrument at different wavelengths (3 nm apart) from 405 to 633 nm. Then the response factors were obtained by normalizing the recorded power values to that at 405 nm. The bigger the factor, the smaller the response of the detector's head to the light will be.
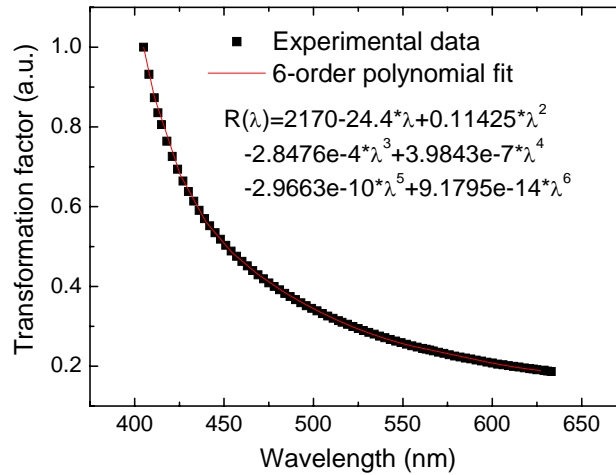
Figure 25: Response factors of the power meter to light excitation at different incident wavelengths.

The real total power of the light source can be expressed as

$$P_0 = \int_{\lambda_1}^{\lambda_2} P(\lambda)d\lambda = \int_{\lambda_1}^{\lambda_2} C_0 I(\lambda)d\lambda \ . \tag{19}$$

The heat generated on the detection head can be written as:

$$\int_{\lambda_1}^{\lambda_2} P(\lambda)\alpha_D(\lambda)d\lambda = Q_{heat} = P_{0m}\alpha_D(\lambda_m) , \tag{20}$$

where $\alpha_D(\lambda)$ is absorption coefficient of the detection head at light wavelength λ. λ_m is the measurement wavelength of the power meter. Because $R(\lambda) = \dfrac{C_1}{\alpha_D(\lambda)}$, and $R(\lambda_m) = \dfrac{C_1}{\alpha_D(\lambda_m)}$ at λ_m,

$$C_0 = \frac{P_{0m}/R(\lambda_m)}{\int_{\lambda_1}^{\lambda_2} I(\lambda)/R(\lambda)\,d\lambda}. \tag{21}$$

C_0 and C_1 are proportionality constants between two physical quantities. P_0 is the real total power of the light source and P_{0m} is the measured total power taken by the power meter at λ_m.

According to Eqs. (19) and (21), the real total power can be calculated. The total power of the xenon lamp after the OL is measured to be 3.1 mW when the wavelength of the power meter is set to 514.5 nm. Considering both the relative irradiance spectrum of the ILS (Fig. 24) and the response factor of the power meter (Fig. 25), we can get that the real power of the xenon lamp in the range of 400 to 620 nm is 2.826 mW.

Furthermore, for a certain sample, an equivalent power of the ILS to a laser excitation at λ_{eq} can be expressed. Providing that the absorbed power by the sample is the same for both the ILS and laser excitations:

$$\int_{\lambda_1}^{\lambda_2} P(\lambda)\alpha_s(\lambda)\,d\lambda = \int_{\lambda_1}^{\lambda_2} C_0 I(\lambda)\alpha_s(\lambda)\,d\lambda = P_{eq}\alpha_s(\lambda_{eq}), \tag{22}$$

so

$$P_{eq} = \frac{\int_{\lambda_1}^{\lambda_2} C_0 I(\lambda)\alpha_s(\lambda)\,d\lambda}{\alpha_s(\lambda_{eq})}. \tag{23}$$

where $\alpha_s(\lambda)$ is absorption coefficient of the sample at light wavelength λ.

For example, according to the absorption spectrum of ferroin (Fig. 24), relative irradiance spectrum of the ILS (Fig. 24) and response factor of the power meter (Fig. 25), the equivalent power of the xenon lamp in the range of 400 to 620 nm is calculated to be 1.05 mW at λ_{eq}=514.5 nm.

(19) Spectrophotometer: Absorbance spectra were measured on a Agilent Hewlett-Packard 8453A UV-VIS-NIR spectrophotometer.

3.2 Analytes and reagents

(1) Ferroin

1 mM ferroin solution in water was used as stock solution. All other concentrations from 1 µM to 300 µM were prepared by diluting the stock solution with deionized water. Deionized water was prepared using a Milli-Q water purification system, MilliRO 5 PLUS.

(2) Chromium (VI)

In experiments which incorporated detection of Cr(VI), potassium dichromate ($K_2Cr_2O_7$, min 99.8% Riedel-de Haën, Germany), 1,5 diphenylcarbazide (DPC, Sigma-Aldrich), phosphoric acid (H_3PO_4, Riedel de Haën) and acetone (HPLC grade, J. T. Bakers), were used. All the materials were used as obtained from the suppliers and no further purification of the chemicals was performed.

Solutions were prepared as follows:

Stock standard solution (1 mg/mL) of Cr(VI) was prepared by dissolving 0.01414 g of $K_2Cr_2O_7$ in 5 mL of water. Solutions of lower concentrations were prepared daily by appropriate dilution.

Stock solution of DPC was prepared by dissolving 0.01 g of DPC in 5 mL of acetone.

H_3PO_4 solution was prepared by diluting 3 mL of 85% H_3PO_4 with 7 mL of water.

DPC solution (10 mL) for on-line generation of Cr-DPC was prepared by diluting 0.8 mL DPC stock solution with 8.8 mL water and 0.4 mL 25% H_3PO_4.

From Fig. 26, we can see that the absorbance of 10 μM Cr(VI)-DPC [corresponding to 500 ng/mL Cr(VI)] at 540 nm is 0.345 AU, corresponding to a molar extinction coefficient of 34500, which is in agreement with the value already reported [157]. At 514.5 nm, the absorbance is 0.264 AU, which corresponds to a molar extinction coefficient of 26400 or an absorption coefficient of 60.79 m^{-1}.
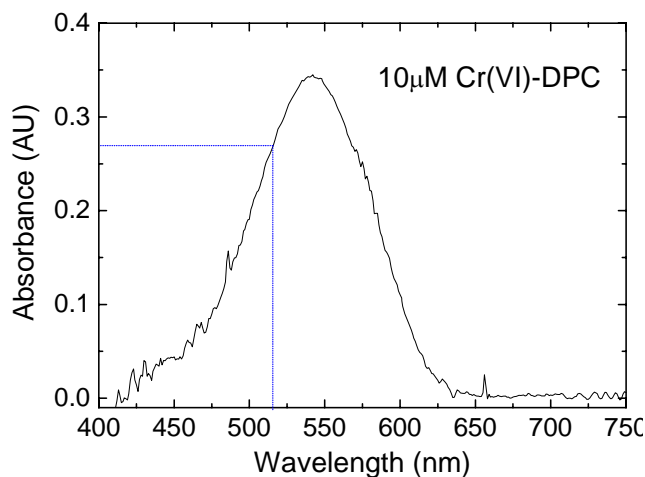
Figure 26: Absorption spectrum of Cr(VI)-DPC complex.

4 RESULTS AND DISCUSSION

For the newly constructed TLM systems as described in the previous chapter, one important task is to optimize the systems in terms of detection limit. This includes maximization of the detection sensitivity while minimizing the noises. Although some papers have discussed the optimization of TL signal in microspace [145,158], they were either based on other configurations (such as crossed-beam scheme) or just concerned some particular aspects of the TL signal in micro space, not contributing to a full understanding of the TL signal in TLM. Therefore further investigation of TL effect in microscale volume is still needed for the system optimization.

In this chapter, theoretical models of TLS in micro space will be given first, and then based on these models, the TLS will be characterized in specific TLM systems both theoretically and experimentally. Detection sensitivity was optimized and noises in these systems were investigated. As an application of the laser-excited TLM, a microfluidic-FIA-TLM was built to detect Cr(VI).

4.1 Theoretical models in TLM

At first, propagation of a light beam (laser or incoherent light beam) in TLM system is analyzed. Then change of the focusing position of a light beam in the sample cell due to movement of the sample cell or the light beam is described. The last part presents the TLS model in micro space.

4.1.1 Propagation of a light beam in TLM system

For the two TLM systems described in the prevous chapter, both a laser beam from an Argon ion laser and an ILS beam from a xenon lamp are used as the excitation source. In order to theoretically modelling the TL signal induced by these excitation sources, propagation of these light beams in TLM system and their intensity profiles in the sample were firstly determined.

To figure out how the light beam propagates through the optical system, both the distribution of the light source and the configuration of the optical system should be known.

4.1.1.1 Propagation of Gaussian beam in TLM system

For the laser beam with nearly Gaussian intensity profile, distribution of the light beam is clear and its propagation can be easily modelled with the theory of Gaussian beam propagation and transformation. In laser-excited TLM, both the probe- and pump-beam parameters after the OL can be adjusted by beam expanders. For ILS-excited TLM, since the light beam from a xenon lamp is collimated through a lens mounted at the end of an optical fibre, only one expander is used for changing the probe beam parameters. For a specific system, the propagation of the beam in the system can be simulated by matrix optics method, where every component is characterized by a matrix. In the experimental systems, two convex lenses are used to form an expander in laser-excited TLM, while in ILS-excited TLM, the expander for the probe beam is composed of three lenses.

For a Gaussian beam, it is possible to define a radius of curvature [$q(z)$] describing both the curvature of the wavefront [$R(z)$] and the transversal size of the beam [$w(z)$]. The nature of this radius of curvature is complex. It is given by [159]

$$\frac{1}{q(z)} = \frac{1}{R(z)} - j\frac{\lambda}{\pi w(z)^2}. \tag{24}$$

Once this complex radius of curvature is defined, the ABCD law can be applied for the calculation of the change of the parameters of the beam.

The ray transfer matrix (RTM) equation describing the propagation of a laser beam through the system is

$$\begin{pmatrix} q_2 \\ 1 \end{pmatrix} = k_c \begin{pmatrix} A & B \\ C & D \end{pmatrix} \begin{pmatrix} q_1 \\ 1 \end{pmatrix}, \tag{25}$$

where k_c is a normalization constant chosen to keep the second component of the ray vector equal to 1, $q_1 = q_0 + d_0$, $q_0 = j\pi w_0^2/\lambda$. q_1 and q_2 are the complex radii of curvature at the first and the last surfaces of the optical system, respectively, and the overall RTM of the optical system is

$$\begin{pmatrix} A & B \\ C & D \end{pmatrix} = \begin{pmatrix} 1 & 0 \\ \frac{-1}{f_{OL}} & 1 \end{pmatrix} \begin{pmatrix} 1 & d_2 \\ 0 & 1 \end{pmatrix} \begin{pmatrix} 1 & 0 \\ \frac{-1}{f_2} & 1 \end{pmatrix} \begin{pmatrix} 1 & d_1 \\ 0 & 1 \end{pmatrix} \begin{pmatrix} 1 & 0 \\ \frac{-1}{f_1} & 1 \end{pmatrix}, \tag{26}$$

for the two-lens expander and

$$\begin{pmatrix} A & B \\ C & D \end{pmatrix} = \begin{pmatrix} 1 & 0 \\ \frac{-1}{f_{OL}} & 1 \end{pmatrix} \begin{pmatrix} 1 & d_3 \\ 0 & 1 \end{pmatrix} \begin{pmatrix} 1 & 0 \\ \frac{-1}{f_3} & 1 \end{pmatrix} \begin{pmatrix} 1 & d_2 \\ 0 & 1 \end{pmatrix} \begin{pmatrix} 1 & 0 \\ \frac{-1}{f_2} & 1 \end{pmatrix} \begin{pmatrix} 1 & d_1 \\ 0 & 1 \end{pmatrix} \begin{pmatrix} 1 & 0 \\ \frac{-1}{f_1} & 1 \end{pmatrix}, \tag{27}$$

for the three-lens expander, where d_0, d_1, d_2 and d_3 are distances between the output laser beam waist and the first expander lens (focal length f_1), between the first and the second expander lenses, between the second expander lens (focal length f_2) and the OL (focal length f_{OL}) in laser-excited TLM or the third expander lens (focal length f_3) in ILS-excited TLM, and between the third expander lens and the OL, respectively.

Then q_2 can be expressed as

$$q_2 = \frac{Aq_1 + B}{Cq_1 + D}. \tag{28}$$

The waist radius and its position after the OL can be written in terms of the real and imaginary parts of the resulting complex radius of curvature as

$$w_1 = w_{OL}\left[1 + \left(\frac{\pi w_{OL}^2}{\lambda R_{OL}}\right)^2\right]^{-1/2}, \quad L = R_{OL}\left[1 + \left(\frac{\lambda R_{OL}}{\pi w_{OL}^2}\right)^2\right]^{-1} = L_S - z_1, \tag{29}$$

where

$$R_{OL} = \left[\mathrm{Re}\left(\frac{1}{q_2}\right)\right]^{-1}, \quad w_{OL} = \left[-\frac{\pi}{\lambda}\mathrm{Im}\left(\frac{1}{q_2}\right)\right]^{-1/2}.$$

L_S is the distance from the OL to the sample plane.

4.1.1.2 Propagation of incoherent light beam in TLM system

For the beam from an ILS, distribution of the light beam can not be easily expressed analytically and hence the description of the propagation of the beam through the optical system is a little bit complicated. In this work, a qualitative analysis of the propagation of the incoherent light beam through an optical system, which is composed of the collimating lens and the OL, was made. Figure 27(a) depicts the propagation of the ILS light ray from the optical fibre to the collimating lens and then through the OL. Those rays in the fibre core with reflection angle larger than the critical angle (θ_c) can transmit through the fibre. The light rays coming out from the fibre can be regarded as emitted from a plane light source whose size equals the cross-sectional area of the fibre core, as shown in Fig. 27(a), where three representative points at 0 (center) and ±R (core radius) in the end plane of the fibre are selected to show the propagation of the incoherent light beam across the optical system. The fibre end was placed at the focal plane of the collimationg lens to achieve the best collimation. Every point in the plane light source emits a cone-shaped light beam, whose vertex angle is $2\theta_c$. According to the propagation characteristics of light ray in the fibre, central intensity of every cone-shaped light beam is usually lower than the outer part. Therefore, in a region behind the collimating lens, the light intensity distribution looks like the light spot in the left of Fig. 27(a). With the incoherent light beam propagating further along the optical axis, the light rays from different light points in the fiber end will overlap and the corresponding light intensity will be distributed more evenly, which would look like the second and third spots from left to right in Fig. 27(a). After the OL, the plane light source in the fibre end is imaged to the focal plane of the OL. According to the principle of geometrical optics, the image of the plane light source under the OL is a light spot with diameter equal to the initial plane light source size multiplied by the lateral magnification of the optical system.

To theoretically analyze the imaging of the plane light source through the optical system composed of the collimating lens (with focal length f_c, focal point F_c and principal point H_c in object space, and f_c', F_c' and H_c' in image space) and the OL (f_{OL}, F_{OL}, H_{OL}, f_{OL}', F_{OL}' and H_{OL}'), equivalent parameters of the optical system (f, F, H, f', F' and H') are calculated. Parameters of the system have been marked in Fig. 27(b), where x is the distance from the equivalent focal plane at F to the object plane at F_c, x' is the distance from the equivalent focal plane at F' to the image plane, and $d_{c\text{-}OL}$ is the distance from the principal plane of the collimating lens at H_c' to that of the OL at H_{OL}.

With $f_c = -f_c' = -12$ mm, $f_c = -f_c' = -8$ mm and $d_{c\text{-}OL}=140$ mm, equivalent parameters of the optical system can be calculated as [160]

$$f' = -\frac{f_c' f_{OL}}{f_c' - f_{OL} - d_{c-OL}} = -0.8 \text{ mm}, \quad p = -\frac{f' d_{c-OL}}{f_{OL}} = -14 \text{ mm}, \quad p' = -\frac{f' d_{c-OL}}{f_c} = 9.33 \text{ mm}, \quad (30)$$

where p is the distance from the principal plane of the collimating lens at H_c to the equivalent principal plane at H and and p' is the distance from the principal plane of the OL at H_{OL}' to the equivalent principal plane at H'.

According to the above parameters, x is calculated to be 1.2 mm. Correspondingly, x' is obtained by applying Newton's imaging equation:

$$x' = \frac{f \cdot f'}{x} = -0.53 \text{ mm}, \quad (31)$$

from which we can see that the image of the object (whose position can be calculated as p' + f' + x' =8 mm) is exactly at the focal plane of the OL (f_{OL}' =8 mm). The lateral magnification (β) of the optical system for the object can be calculated as

$$\beta = -\frac{f}{x} = -0.667.$$ (32)

This means the image is downsized and inverted. For the fiber core with diameter 350 μm, the image size under the OL is 233 μm.
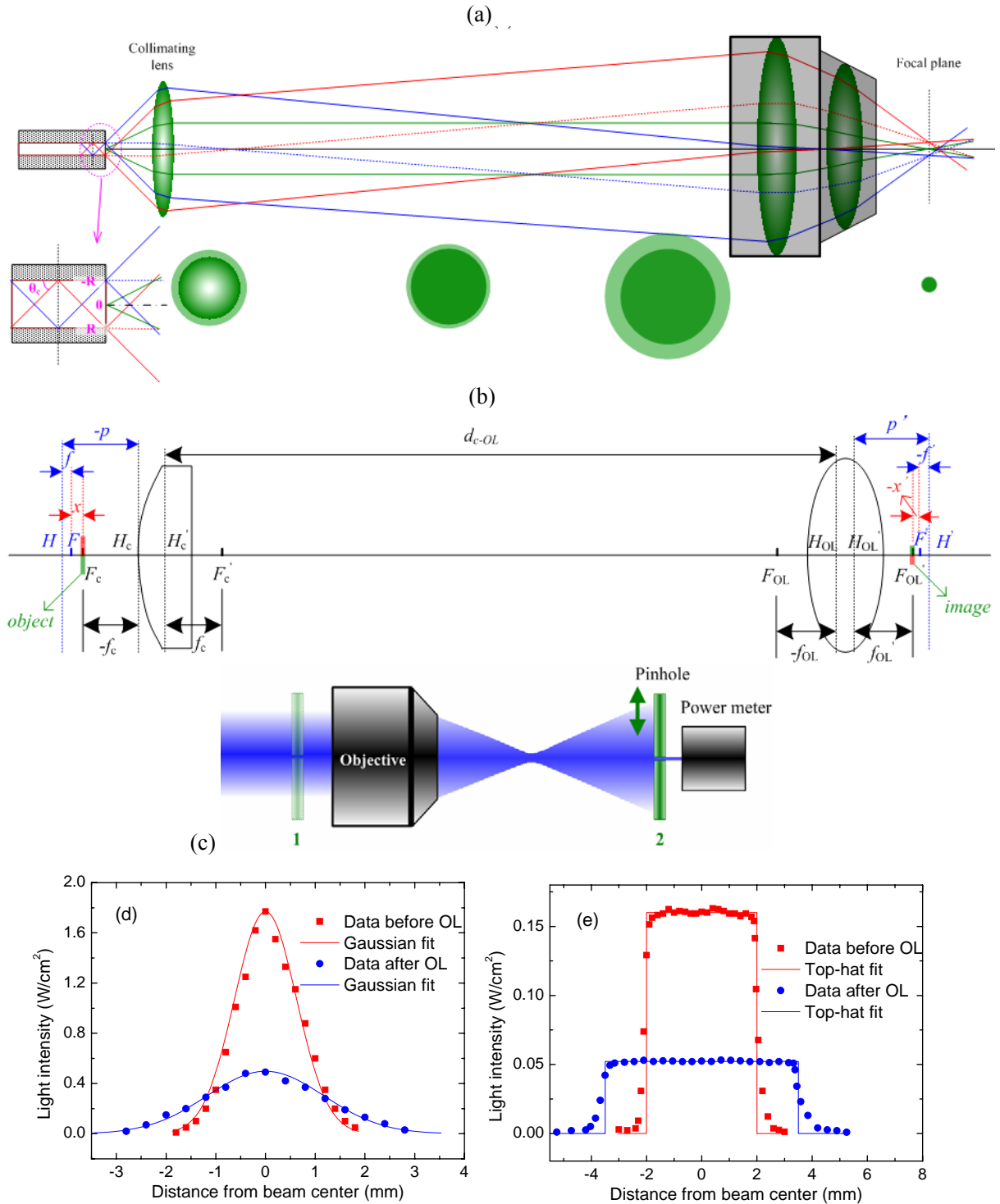
Figure 27: Schematic graphs for (a) propagation of the ILS light ray from the optical fibre to the collimating lens and then through the OL, (b) equivalent optical parameters for the optical system composed of the collimating lens and the OL, and (c) excitation beam intensity profile measurement before and after the OL by pinhole scanning method. Experimental light intensity profiles measured before (Position 1) and after the OL (Position 2) for (d) Argon laser and (e) xenon lamp, as well as corresponding fitting curves.

Figure 27(c) shows a schematic graph for measuring the cross-sectional light intensity distributions, which were obtained by scanning a 200-μm pinhole across the light spot at postion 1 (1 cm before the front of the OL) and position 2 (2 cm behind the OL), and simultaneously, recording the transmitted light power behind the pinhole with a photodetector. In Figs. 27(d) and 27(e), intensity profiles of the Argon laser and the xenon lamp before and after the OL were measured. From the results we can see that the profiles for the laser case are nearly gaussian, while for the ILS case, top-hat-like profiles were obtained. Though the intensity profile of the incoherent light beam at the focal plane of the OL could not be measured under the experimental conditions in our lab, we can assume that it should be also like a top hat, perhaps with some of fringes due to the diffraction of the light waves through the finite aperture of the OL. Therefore, in the next section of theoretical derivation of temperature distribution in micro space, both the Gaussian and top-hat beam excitations are included.

4.1.2 Change of the focusing position of a light beam in sample cell

When moving the microchip along z-axis or adjusting the beam expanders to change the beam parameters after the OL, the focusing position of the pump/probe beam in the sample cell will be changed and this change is slightly different from the moved distance (such as H_m in Fig. 28) due to the refraction.
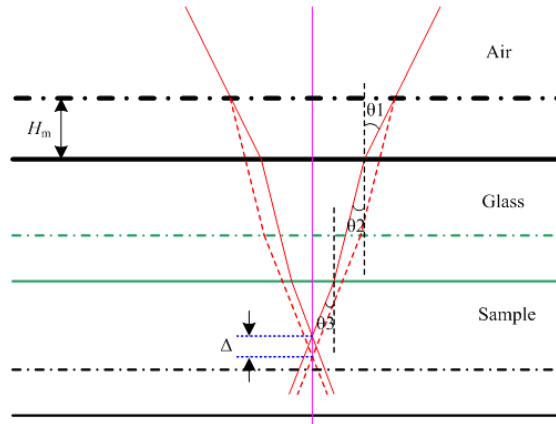
Figure 28: Schematic graph of focusing position change of a light beam after the movement of sample cell by H_m along z-axis.

According to the principle of optical refraction, this change can be written as

$$\Delta = H_m \left(\frac{\tan \theta_1}{\tan \theta_3} - 1 \right),\tag{33}$$

in which

$$\theta_3 = \arcsin\left(\frac{n_1 \sin \theta_1}{n_3} \right).$$

For a Gaussian beam, the beam divergence is given by [159]

$$\theta_1 \simeq \frac{\lambda}{\pi w_0}.\tag{34}$$

The total angular spread of the beam far from the waist is then given by

$$\Theta = 2\theta_1.\tag{35}$$

When w_0=0.7, 1 and 2 μm, θ_1 is 13.4º, 9.38º and 4.69º, respectively.

In later experiments, this focusing position change of the pump or probe beam caused by moving the microchip along z-axis or adjusting the beam expanders will be considered.

4.1.3 Theoretical models of TLS in micro space

TL signal is produced by the temperature rise-induced refractive index change following absorption of the light energy. Therefore, in a system as shown in Fig. 7, temperature distribution needs to be obtained first. As a result of the difficulty of obtaining a complete temperature distribution for the system, the problem was solved for four different cases:

(1) Firstly, effect of the varying excitation beam size on TL signal dominates while the effect of surroundings (side wall and top/bottom layer) is neglected, such as in Fig. 29(a), which is especially applicable for highly focused laser-excited TLM.

(2) Secondly, a two-dimensional temperature distribution in flowing medium is given without considering the impact of surroundings, such as in Fig. 29(b).

(3) Thirdly, effect of the top/bottom layers on TL signal is taken into account whereas that of both side wall and varying beam size is neglected, as drawn in Fig. 29(c), which is usually suitable for the case when the pump beam radius is much smaller than the width of the sample cell and doesn't change a lot along the sample length.

(4) Finally, a one-dimensional model as in Fig. 29(d) is employed to account for the influence of the side wall when the beam size is comparable to that of the sample cell, particularly for the case when the thermal conductivity of the side wall is much larger or smaller than that of the sample. Thermal diffusion along z-axis is neglected.

In Fig. 29, T_s is the temperature of surroundings. T_i, k_i, D_i and $\partial n_i/\partial T$ are the temperature rise with respect to T_s, thermal conductivity, thermal diffusivity and temperature coefficient of refractive index of the ith medium, respectively, i=0 (top-layer), i=1 (sample), i=2 (bottom layer), i=3 (sidewall). h_i is the convective heat transfer coefficient between the ith medium and the surroundings. v_x is the flow velocity along x-axis. Dimensions of each layer are indicated in Fig. 29. Because intensity profiles of ILS and some high-power multi-mode lasers are usually flat on its top, "top-hat beam" is used to represent ILS (or some high-power lasers) as used by other researchers [80].
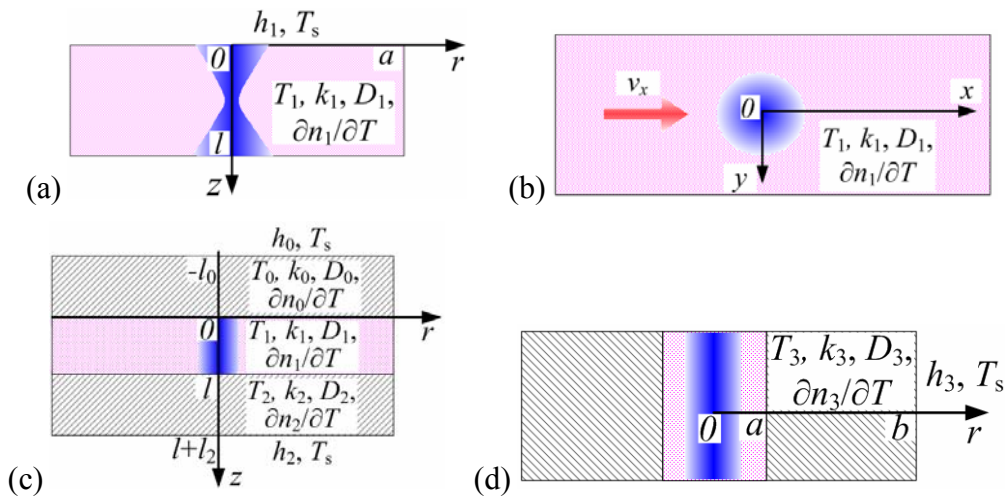
Figure 29: Coordinates and sample and/or sample cell parameters used in (a) a three-dimensional sample model with changing excitation beam radius inside the sample, (b) a two-dimensional sample model in a flowing medium, (c) a three-layer sample model without sidewall and (d) a one-dimensional sample model considering the sidewall.

In the next part, the temperature distributions under excitation of both a Gaussian and a top-hat beam are deduced. Then, the Fresnel diffraction theory is employed to describe the influence of TL element on the probe beam.

4.1.3.1 Temperature distribution with varying excitation beam

Many previous TLS theories treated the excitation beam as constant in the sample, which is not always true especially for the cases where the beam radius changes in the sample. Bialkowski [161,162] has given the effective inverse focal length of TL considering the divergent nature of the excitation beam, however, this is for pulsed excitation case and by neglecting thermal conduction along z-axis a direct integration of temperature along z was performed. Recently, Anraku et al. [163] used fluidic dynamics and wave optics softwares to simulate the effect of a divergent excitation beam and sample surroundings. Though this finite element analysis based method is reliable, it is too complicated and inconvenient for complete TL signal analysis due to the lack of analytical forms describing the temperature distribution in the sample and related TL signal. Therefore, a more general expression of the temperature distribution in the sample under excitation of a divergent excitation beam will be deduced first. The impact of sample cell on the temperature is neglected. This is reasonable for the TL signal analysis if the thermal wavelength [$\lambda_h = 2(\pi D/f)^{1/2}$, with D being the thermal diffusivity and f the modulation frequency] is smaller than the sample length, which is satisfied in case of laser-excited TLM described in the experimental part ($\lambda_h = 42.4$ μm at $f = 1$ kHz, smaller than the used sample lengths such as 100 μm).

The thermal diffusion equation in the sample is given as

$$\frac{1}{r}\frac{\partial}{\partial r}\left(r\frac{\partial T_1}{\partial r}\right)+\frac{\partial^2 T_1}{\partial z^2}+\frac{1}{k_1}g\left(r,z,t\right)=\frac{1}{D_1}\frac{\partial T_1}{\partial t} \quad \text{in } 0\leq r\leq a, 0\leq z\leq l, \quad (36)$$

with the boundary and initial conditions

$$k_1\frac{\partial T_1}{\partial r}\bigg|_{r=a}=-h_1T_1|_{r=a} \text{ ; } k_1\frac{\partial T_1}{\partial z}\bigg|_{z=0}=h_1T_1|_{z=0} \text{ ; } k_1\frac{\partial T_1}{\partial z}\bigg|_{z=l}=-h_1T_1|_{z=l} \text{ ; } T_1\left(r,t\right)|_{t=0}=0. \quad (37)$$

The solution of this problem can be written in terms of the Green's function,

$$T_1\left(r,z,t\right)=\frac{D_1}{k_1}\int_{r'=0}^{a}\int_{z'=0}^{l}\int_{\tau=0}^{t}G\left(r,z,t|r',z',\tau\right)\cdot g\left(r',z',\tau\right)2\pi r'dr'dz'd\tau, \quad (38)$$

where the Green's function is obtainable from the solution of the homogeneous version of the problem. The Green's function can be expressed as [164]

$$G\left(r,z,t|r',z',\tau\right)=\sum_{m=1}^{\infty}\sum_{p=1}^{\infty}\frac{\exp[-D_1(\beta_m^2+\eta_p^2)(t-\tau)]}{N(\beta_m)N(\eta_p)}R_0(\beta_m,r)Z(\eta_p,z)R_0(\beta_m,r')Z(\eta_p,z'), \quad (39)$$

where the eigenfunctions $R_0(\beta_m, r)$ and $Z(\eta_p, z)$, and the norms $N(\beta_m)$ and $N(\eta_p)$ are

$$R_0(\beta_m,r)=J_0(\beta_m r), \frac{1}{N(\beta_m)}=\frac{2}{J_0^2(\beta_m a)}\frac{\beta_m^2}{a^2[(h_1/k_1)^2+\beta_m^2]},$$

$$Z(\eta_p,z)=\eta_p\cos(\eta_p z)+\frac{h_1}{k_1}\sin(\eta_p z),$$

46

$$\frac{1}{N(\eta_p)} = 2\left[\left(\eta_p^2 + \frac{h_1^2}{k_1^2}\right)\left(l + \frac{h_1/k_1}{\eta_p^2 + h_1^2/k_1^2}\right) + \frac{h_1}{k_1}\right]^{-1}, \tag{40}$$

and the eigenvalues β_m and η_p are the positive roots of

$$\beta_m J_1(\beta_m a) = \frac{h_1}{k_1}J_0(\beta_m a), \;\; \tan(\eta_p l) = \frac{2\eta_p h_1/k_1}{\eta_p^2 - h_1^2/k_1^2}, \text{ respectively,} \tag{41}$$

where $J_0(\cdot)$ and $J_1(\cdot)$ are the zero- and first-order Bessel functions of the first kind, respectively. For a continuous light source, the heat generation rate can be expressed as

$$g(r,z,t) = \begin{cases} \dfrac{2\alpha P}{\pi[a_e(z)]^2}\exp\left\{-2\dfrac{r^2}{[a_e(z)]^2} - \alpha z\right\}\dfrac{1+\cos\omega t}{2} & \text{for a Gaussian beam,} \\[4mm] \dfrac{\alpha P}{\pi[a_e(z)]^2}Circ(r,z)\exp(-\alpha z)\dfrac{1+\cos\omega t}{2} & \text{for a top-hat beam.} \end{cases} \tag{42}$$

$$a_e(z) = \begin{cases} a_{e0}\sqrt{1+[(z-0.5l)/z_{Re}]^2} & \text{for a Gaussian beam,} \\[2mm] a_{e0}\sqrt{1+[(z-0.5l)/z_T]^2} & \text{for a top-hat beam.} \end{cases} \tag{43}$$

$$Circ(r,z) = \begin{cases} 1 & \text{for } r \le a_e(z), \\ 0 & \text{for } r > a_e(z). \end{cases} \tag{44}$$

in which α is the absorption coefficient of the sample. P, a_{e0}, $z_{Re}=\pi a_{e0}^2/\lambda_e$, λ_e and ω are the power, beam waist radius, Rayleigh range, wavelength and angular modulation frequency of the excitation beam, respectively. It should be noted that for the top-hat beam, change of the beam size along z-axis is assumed to be hyperbolic, as described by the bottom formula on the right side of Eq. (43) with z_T determined by the light beam profile after the focusing lens. As shown in Fig. 30, the beam radius distribution of a xenon light source, which was measured in experiment by knife-edge method, is well fitted by a hyperbolic curve. The minimum beam size (twice of a_{e0}) is obtianed to be 214 μm, which is in good agreement with the theoretically calculated value of 233 μm as shown in section 4.1.1.2.
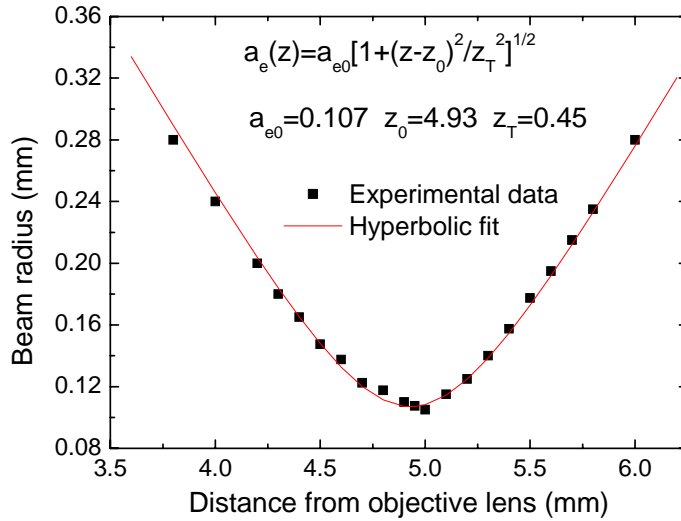
Figure 30: Beam radius distributions of a xenon lamp along optical path after a 20×/NA 0.40 long-working-distance objective lens.

47

By further mathematical deduction, the temperature distribution can be written as

$$T_1(r,z,t) = \frac{D_1}{k_1} \sum_{m=1}^{\infty} \sum_{p=1}^{\infty} \frac{\exp[-D_1(\beta_m^2+\eta_p^2)t]}{N(\beta_m)N(\eta_p)} R_0(\beta_m,r)Z(\eta_p,z)B(t) \int_{z'=0}^{l} A(z')\frac{Z(\eta_p,z')}{[a_e(z')]^2}\exp(-\alpha z')dz', \qquad (45)$$

$$A(z') = \begin{cases} 2\alpha P \int_{r'=0}^{a} r' J_0(\beta_m r')\exp\left\{-\frac{2r'^2}{[a_e(z')]^2}\right\}dr' & \text{for a Gaussian beam,} \\[3mm] \alpha P \dfrac{a_e(z')}{\beta_m} J_1[\beta_m a_e(z')] & \text{for a top-hat beam.} \end{cases} \qquad (46)$$

$$B(t) = \frac{\left\{e^{D_1(\beta_m^2+\eta_p^2)t}\left[D_1(\beta_m^2+\eta_p^2)\cos\omega t + \omega\sin\omega t\right] - D_1(\beta_m^2+\eta_p^2)\right\}}{D_1^2(\beta_m^2+\eta_p^2)^2+\omega^2} + \frac{e^{D_1(\beta_m^2+\eta_p^2)t}-1}{D_1(\beta_m^2+\eta_p^2)}, \qquad (47)$$

4.1.3.2 Temperature distribution in a flowing medium

In fluid mechanics, the Reynolds number is defined as

$$Re = \frac{2\rho v d_c}{\eta}, \qquad (48)$$

where ρ is the fluid density, v is the flow velocity, d_c is the diameter of the channel, η is the viscosity coefficient. When $Re<2000$, the flow is laminar; when $Re>2000$, the flow is turbulent. At 20°C, the viscosity coefficient of water is 1.0087 cP (10^{-3} Pa·s). For example, if water flows in a 600 μm channel, the flow is laminar when $v<3.36$ m/s. In the microchip used in this research, the flow is definitely laminar flow because the flow velocity is usually much less than 1 m/s.

In a microchannel, the flowing velocity at r with respect to the center of the channel can be expressed as [165]

$$v = \frac{\Delta P + \rho g l_f}{4\eta l_f}\left(r^2 - d_c^2\right), \qquad (49)$$

Where ΔP is the pressure difference, g is the gravity acceleration, l_f is the length of the fluid. The average flow velocity of the fluid is

$$v = \frac{\Delta P + \rho g l_f}{8\eta l_f}d_c^2. \qquad (50)$$

We can see that the average flow velocity is just half of the flow velocity at the central line of the fluid.

Here, to obtain an analytical temperature solution for the fluid excited by a pump beam in a microchannel, the flow velocity across the channel cross-section is assumed to be the same, namely v_x, when the flow is in the x-direction. The sample is supposed to be homogeneous and optically thin. Then the temperature satisfies the following thermal differential equation,

$$\frac{\partial T_1(x,y,t)}{\partial t} = D_1\nabla^2 T_1(x,y,t) - v_x\frac{\partial T_1(x,y,t)}{\partial x} + \frac{D_1}{k_1}g(x,y,t), \qquad (51)$$

where $g(x,y,t)$ is the source term, which is expressed as

$$g(x,y,t) = \begin{cases} \dfrac{2\alpha P}{\pi a_e^2} \exp\left[-2(x^2+y^2)/a_e^2\right]\dfrac{1+\cos\omega t}{2} & \text{for a Gaussian beam,} \\[12pt] \dfrac{\alpha P}{\pi a_e^2} Circ(x,y)\dfrac{1+\cos\omega t}{2} & \text{for a top-hat beam.} \end{cases} \tag{52}$$

where a_e is the excitation beam radius in the sample. $Circ(x, y)$ is defined as

$$Circ(x,y) = \begin{cases} 1 & \sqrt{x^2+y^2} \le a \\ 0 & \sqrt{x^2+y^2} > a \end{cases}. \tag{53}$$

The assumed boundary conditions are

$$T_1(x,y,t)\big|_{t=0} = 0; \quad T_1'(x,y,t)\big|_{t=0} = 0,$$
$$T_1(x,y,t)\big|_{x=\pm\infty} = 0; \quad T_1(x,y,t)\big|_{y=\pm\infty} = 0, \tag{54}$$

where $T_1'(x, y, t)$ represents the gradient of the temperature, and the size of the sample in x- and y-direction is considered infinite. The solution is given by

$$T_1(x,y,t) = \int_{-\infty}^{+\infty}\int_{-\infty}^{+\infty}\int_0^{+\infty} G(x,y,t|\xi,\eta,\tau)g(\xi,\eta,\tau)d\xi d\eta d\tau, \tag{55}$$

where $G(x, y, t|\xi, \eta, \tau)$ is the Green's function appropriate for Eq. (51) and can be expressed as [166]

$$G = \frac{H(t)}{4\pi k_1(t-\tau)}\exp\left\{-\left[x-(\xi+v_x(t-\tau))\right]^2\Big/\left[4D_1(t-\tau)\right]\right\}\exp\left\{-(y-\eta)^2\Big/\left[4D_1(t-\tau)\right]\right\}, \tag{56}$$

where $H(t)$ is the unit step function. Substitution of Eq. (56) in Eq. (55), along with Eq. (52), leads to the desired temperature distribution

$$T_1(x,y,t) = \frac{\alpha PD_1}{\pi k_1}\int_0^t \frac{(1+\cos\omega\tau)\exp\left\{-2\left[(x-v_x(t-\tau))^2+y^2\right]\Big/\left[8D_1(t-\tau)+a_e^2\right]\right\}d\tau}{8D_1(t-\tau)+a_e^2}, \tag{57}$$

for the Gaussian beam excitation case, and

$$T_1(x,y,t) = \frac{\alpha PD_1}{4\pi^{3/2}k_1 a_e^2}\int_0^t\int_{-a_e}^{a_e}\frac{1+\cos(\omega\tau)}{\sqrt{4D_1(t-\tau)}}\exp\left\{-\frac{\left[\xi-x+v_x(t-\tau)\right]^2}{4D_1(t-\tau)}\right\}$$
$$\times\left[erf\left(\frac{\sqrt{a_e^2-\xi^2}-y}{\sqrt{4D_1(t-\tau)}}\right)+erf\left(\frac{\sqrt{a_e^2-\xi^2}+y}{\sqrt{4D_1(t-\tau)}}\right)\right]d\xi d\tau, \tag{58}$$

for the top-hat beam excitation case. Here, $erf(\cdot)$ is the error function.

4.1.3.3 Temperature distribution in a three-layer system

Three-layer temperature model has been deduced by some researchers [167, 168], but they treated the dimensions of layers on both sides [layers 0 and 2 in Fig. 30(c)] as infinite. However, such assumption is no longer valid in micro space if these two layers are very thin (such as ~100 μm). Here, both the finite dimensions of the top and bottom layers and their heat exchange with outer surroundings are considered. The mathematical formulation of thermal conduction in this three-layer system is given as

$$\nabla^2 T_0 - \frac{1}{D_0}\frac{\partial T_0}{\partial t} = 0 \quad \text{in} \ -l_0 \le z < 0 \,, \tag{59}$$

$$\nabla^2 T_1 - \frac{1}{D_1}\frac{\partial T_1}{\partial t} = -\frac{g(r,z,t)}{k_1} \quad \text{in} \ 0 \le z \le l \,, \tag{60}$$

$$\nabla^2 T_2 - \frac{1}{D_2}\frac{\partial T_2}{\partial t} = 0 \quad \text{in} \ l < z \le l + l_2 \,, \tag{61}$$

with the boundary conditions

$$T_0\big|_{z=0} = T_1\big|_{z=0} \,; \ T_1\big|_{z=l} = T_2\big|_{z=l} \,; \ k_0\frac{\partial T_0}{\partial z}\bigg|_{z=0} = k_1\frac{\partial T_1}{\partial z}\bigg|_{z=0} \,; \ k_1\frac{\partial T_1}{\partial z}\bigg|_{z=l} = k_2\frac{\partial T_2}{\partial z}\bigg|_{z=l} \,;$$

$$k_0\frac{\partial T_0}{\partial z}\bigg|_{z=-l_0} = h_0 T_0\big|_{z=-l_0} \,; \ k_2\frac{\partial T_2}{\partial z}\bigg|_{z=l+l_2} = -h_2 T_2\big|_{z=l+l_2} \,. \tag{62}$$

In steady state, solutions of Eqs. (59)-(61) contain both the static and periodic terms. Here only the periodic solution is considered since the TL signal observed in a real case measurement is related to the periodic term only, if a phase-sensitive detection is used. For a continuous light source oscillating at the modulation frequency (ω), the heat deposited by sample absorption is given by:

$$g(r,z,t) = \begin{cases} \dfrac{2\alpha P}{\pi a_e^2}\exp\left[-2r^2/a_e^2 - \alpha z\right]\dfrac{\exp(j\omega t)+c.c.}{2} & \text{for a Gaussian beam,} \\[3mm] \dfrac{\alpha P}{\pi a_e^2}Circ(r)\exp(-\alpha z)\dfrac{\exp(j\omega t)+c.c.}{2} & \text{for a top-hat beam,} \end{cases} \tag{63}$$

$Circ(r)$ is similar to its form in Eq. (44) except there is no longer any z-dependence. Correspondingly, by applying the Hankel integral transformation technique, the alternating current (AC) temperature distributions in the three regions can be expressed as:

$$T_0(r,z,t) = \int_0^\infty \delta J_0(\delta r)\cos(\omega t)\left[A_0\exp(\delta_0 z) + B_0\exp(-\delta_0 z)\right]d\delta \,, \tag{64}$$

$$T_1(r,z,t) = \int_0^\infty \delta J_0(\delta r)\cos(\omega t)\left[A_1\exp(\delta_1 z) + B_1\exp(-\delta_1 z) - C\exp(-\alpha z)\right]d\delta \,, \tag{65}$$

$$T_2(r,z,t) = \int_0^\infty \delta J_0(\delta r)\cos(\omega t)\left\{A_2\exp\left[\delta_2(z-l)\right] + B_2\exp\left[-\delta_2(z-l)\right]\right\}d\delta \,, \tag{66}$$

where

$$C = \begin{cases} \dfrac{\alpha P\exp(-\delta^2 a_e^2/8)}{2\pi k_1(\alpha^2 - \delta_1^2)} & \text{for a Gaussian beam,} \\[4mm] \dfrac{\alpha P J_1(\delta a_e)}{\pi a_e k_1 \delta(\alpha^2 - \delta_1^2)} & \text{for a top-hat beam,} \end{cases}$$

$$D = \frac{k_0\delta_0 + h_0}{k_0\delta_0 - h_0}e^{2\delta_0 l_0} \,, \ E = \frac{k_2\delta_2 - h_2}{k_2\delta_2 + h_2}e^{-2\delta_2 l_2} \,,$$

$$F = \frac{(k_1\delta_1 - k_0\delta_0) + (k_1\delta_1 + k_0\delta_0)D}{(k_1\delta_1 + k_0\delta_0) + (k_1\delta_1 - k_0\delta_0)D}, \quad G = \frac{(k_0\delta_0 - k_1\alpha) - (k_0\delta_0 - k_1\alpha)D}{(k_1\delta_1 + k_0\delta_0) + (k_1\delta_1 - k_0\delta_0)D}C,$$

$$H = \frac{(k_2\delta_2 - k_1\delta_1) - (k_2\delta_2 + k_1\delta_1)E}{(k_2\delta_2 - k_1\delta_1)E - (k_2\delta_2 + k_1\delta_1)}e^{-2\delta_1 l}, \quad I = \frac{(k_1\alpha - k_2\delta_2) + (k_2\delta_2 + k_1\alpha)E}{(k_2\delta_2 - k_1\delta_1)E - (k_2\delta_2 + k_1\delta_1)}Ce^{-(\alpha+\delta_1)l},$$

$$B_1 = \frac{I - G}{F - H}, \quad A_1 = FB_1 + G, \quad B_0 = \frac{A_1 + B_1 - C}{1 + D}, \quad A_0 = DB_0,$$

$$B_2 = \frac{A_1 e^{\delta_1 l} + B_1 e^{-\delta_1 l} - Ce^{-\alpha l}}{1 + E}, \quad A_2 = EB_2, \quad \delta_i = \sqrt{\delta^2 + j\omega/D_i}, \quad i=0, 1, 2.$$

4.1.3.4 Temperature distribution considering the effect of sidewall

The thermal conduction in one-dimensional sample-sidewall system is given as

$$D_1\frac{1}{r}\frac{\partial}{\partial r}\left(r\frac{\partial T_1}{\partial r}\right) + \frac{D_1}{k_1}g(r,t) = \frac{\partial T_1(r,t)}{\partial t} \quad \text{in } 0 \le r \le a, \tag{67}$$

$$D_3\frac{1}{r}\frac{\partial}{\partial r}\left(r\frac{\partial T_3}{\partial r}\right) = \frac{\partial T_3(r,t)}{\partial t} \quad \text{in } a < r \le b, \tag{68}$$

with the boundary and initial conditions

$$T_1(r,t)\big|_{r=a} = T_3(r,t)\big|_{r=a}; \quad k_1\frac{\partial T_1}{\partial r}\bigg|_{r=a} = k_3\frac{\partial T_3}{\partial r}\bigg|_{r=a}; \quad k_3\frac{\partial T_3}{\partial r}\bigg|_{r=b} = -h_3T_3\big|_{r=b}; \quad T_1(r,t)\big|_{t=0} = 0;$$

$$T_3(r,t)\big|_{t=0} = 0. \tag{69}$$

The solution of this problem can be written in terms of the Green's function,

$$T_i(r,t) = \frac{D_1}{k_1}\int_{\tau=0}^{t}\int_{r'=0}^{a}r'G_{i1}(r,t|r',\tau)\cdot g(r',\tau)dr'd\tau \quad i=1, 3, \tag{70}$$

where the Green's function is obtainable from the solution of the homogeneous version of the problem. The Green's function can be expressed as [169]

$$G_{i1}(r,t|r',\tau) = \sum_{n=1}^{\infty}e^{-\beta_n^2(t-\tau)}\frac{1}{N_n}\frac{k_1}{D_1}\psi_{in}(r)\psi_{1n}(r'), \tag{71}$$

where the norm N_n is

$$N_n = \frac{k_1}{D_1}\int_0^a r'\psi_{1n}^2(r')dr' + \frac{k_3}{D_3}\int_a^b r'\psi_{3n}^2(r')dr', \tag{72}$$

The eigenfunctions $\psi_{1n}(r)$ and $\psi_{3n}(r)$ are

$$\psi_{1n}(r) = J_0\left(\frac{\beta_n}{\sqrt{D_1}}r\right), \tag{73}$$

$$\psi_{3n}(r) = A_{2n}J_0\left(\frac{\beta_n}{\sqrt{D_3}}r\right) + B_{2n}Y_0\left(\frac{\beta_n}{\sqrt{D_3}}r\right). \tag{74}$$

A_{2n} and B_{2n} are

$$A_{2n} = \frac{1}{\Delta}\left[J_0(\gamma)Y_1\left(\frac{a}{b}\eta\right) - KJ_1(\gamma)Y_0\left(\frac{a}{b}\eta\right)\right],$$

$$B_{2n} = \frac{1}{\Delta}\left[KJ_1(\gamma)J_0\left(\frac{a}{b}\eta\right) - J_0(\gamma)J_1\left(\frac{a}{b}\eta\right)\right],$$

where $Y_0(\cdot)$ and $Y_1(\cdot)$ are the zero- and first-order Bessel functions of the second kind, respectively, and

$$\Delta = J_0\left(\frac{a}{b}\eta\right)Y_1\left(\frac{a}{b}\eta\right) - J_1\left(\frac{a}{b}\eta\right)Y_0\left(\frac{a}{b}\eta\right).$$

Then, the β_n values are the roots of the following transcendental equation

$$\begin{vmatrix} J_0(\gamma) & -J_0(\frac{a}{b}\eta) & -Y_0(\frac{a}{b}\eta) \\ KJ_1(\gamma) & -J_1(\frac{a}{b}\eta) & -Y_1(\frac{a}{b}\eta) \\ 0 & \frac{H}{\eta}J_0(\eta)-J_1(\eta) & \frac{H}{\eta}Y_0(\eta)-Y_1(\eta) \end{vmatrix} = 0, \tag{75}$$

$$\gamma = \frac{a\beta_n}{\sqrt{D_1}}, \quad \eta = \frac{b\beta_n}{\sqrt{D_3}}, \quad H = \frac{bh_3}{k_3}, \quad K = \frac{k_1}{k_3}\sqrt{\frac{D_3}{D_1}}.$$

The heat source term is similar to Eq. (52) except for the rectangular coordinate, which is changed into polar coordinates. After deduction, the temperature can be expressed as

$$T_i(r,t) = C_0 \sum_{n=1}^{\infty} e^{-\beta_n^2 t}\frac{1}{N_n}\psi_{in}(r)\cdot A\cdot B(t) \qquad i=1,3. \tag{76}$$

in which

$$N_n = \frac{k_1}{D_1}\frac{a^2}{2}\left[J_0^2(x_1)+J_1^2(x_1)\right]+$$

$$\frac{k_3}{D_3}\sum_{i=1}^{3}C_i\left\{\frac{b^2}{2}\left[F_i(y_1)G_i(y_1)+H_i(y_1)I_i(y_1)\right] - \frac{a^2}{2}\left[F_i(y_0)G_i(y_0)+H_i(y_0)I_i(y_0)\right]\right\},$$

in which $x_1 = \gamma$, $y_1 = \eta$, $y_0 = \dfrac{a\beta_n}{\sqrt{D_3}}$,

when $i=1$: $C_i = A_{2n}^2$, $F_i(\cdot)=G_i(\cdot)=J_0(\cdot)$, $H_i(\cdot)=I_i(\cdot)=J_1(\cdot)$;

$\quad i=2$: $C_i = B_{2n}^2$, $F_i(\cdot)=G_i(\cdot)=Y_0(\cdot)$, $H_i(\cdot)=I_i(\cdot)=Y_1(\cdot)$;

$\quad i=3$: $C_i = 2A_{2n}B_{2n}$, $F_i(\cdot)=J_0(\cdot)$, $G_i(\cdot)=Y_0(\cdot)$, $H_i(\cdot)=J_1(\cdot)$, $I_i(\cdot)=Y_1(\cdot)$.

$$B(t) = \frac{1}{\beta_n^4+\omega^2}\left[e^{\beta_n^2 t}\left(\beta_n^2\cos\omega t+\omega\sin\omega t\right)-\beta_n^2\right]+\frac{e^{\beta_n^2 t}-1}{\beta_n^2}.$$

$$C_0 = \begin{cases} P/(2\pi a_e^2) & \text{for a top-hat beam,} \\ P/(\pi a_e^2) & \text{for a Gaussian beam.} \end{cases}$$

$$A = \begin{cases} \dfrac{\alpha a_e \sqrt{D_1}}{\beta_n} J_1\left(a_e \beta_n / \sqrt{D_1}\right) & \text{for a top-hat beam,} \\ \alpha \displaystyle\int_0^a r' J_0\left(\beta_n r' / \sqrt{D_1}\right) \exp\left(-2r'^2/a_e^2\right) dr' & \text{for a Gaussian beam.} \end{cases}$$

4.1.3.5 TL signal model under Fresnel diffraction theory

In TLS technique, a probe laser will be used to probe the temperature-rise induced refractive index change (namely the TL element), as shown in Fig. 31.
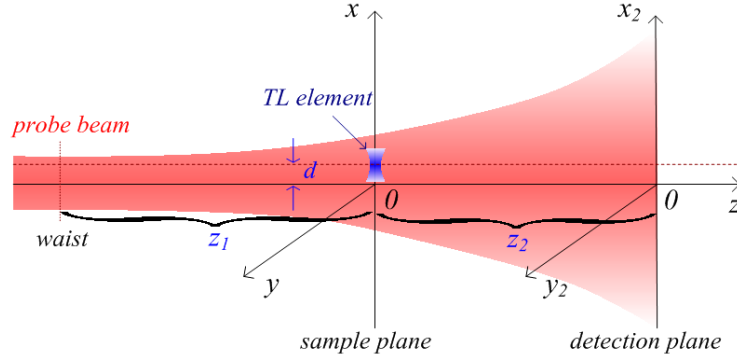
Figure 31: Schematic diagram of a probe beam diffracted by a phase shift element in rectangular coordinate system.

Because of the aberrant nature of the TL element, the Fresnel diffraction theory is used to give an accurate quantitative description of the TL effect. On the basis of it, the complex electric field distribution of the probe beam in the detection plane is expressed as [108]

$$E_2(r_2, z_1 + z_2, t) = \frac{j2\pi}{\lambda z_2} \exp[-jk(z_2 + \frac{r_2^2}{2z_2})] \int_0^\infty E_1'(r, z_1, t) J_0(k\frac{rr_2}{z_2}) \exp(-jk\frac{r^2}{2z_2}) r dr, \qquad (77)$$

in a cylindrical coordinate system, and

$$E_2(x_2, y_2, d, z_1 + z_2, t) = \frac{j \exp(-jkz_2)}{2\lambda z_2} \int_{-\infty}^{+\infty}\int_{-\infty}^{+\infty} E_1'(x, y, d, z_1, t) \exp\left\{-\frac{jk}{2z_2}\left[(x_2 - x)^2 + (y_2 - y)^2\right]\right\} dx dy, \qquad (78)$$

in a rectangular coordinate system. Where λ is the wavelength of the probe beam, $k=2\pi/\lambda$ is the wave number. z_1 and z_2 are the distance from the probe beam waist to the sample and the distance from the sample to the detection plane, respectively. r (or x, y) and r_2 (or x_2, y_2) are the coordinates in the sample and detection plane, respectively. d, which is called the beam offset, is the distance between central axes of the probe and excitation beams in direction of x coordinate. $d > 0$ means the central axis of the excitation beam (dashed line in Fig. 31) is above the central axis of the probe beam and $d < 0$ means below the central axis of the probe beam. $E'_1(r, z_1, t)$ or $E'_1(x, y, d, z_1, t)$ is the complex amplitude of the electric field of the probe beam at the exit plane of the TL element, that is

$$E_1'(r, z_1, t) = E_1(r, z_1) \exp[-j\Delta\phi(r, t)]. \qquad (79)$$

or

$$E_1'(x, y, d, z_1, t) = E_1(x, y, z_1) \exp[-j\Delta\phi(x - d, y, t)]. \qquad (80)$$

$E_1(\cdot)$ and $\Delta\Phi(\cdot)$ are the electric field of the probe beam before the TL element and the phase shift induced by the TL element, respectively. For a Gaussian probe beam with TEM00 mode,

$$E_1(r, z_1) = \sqrt{\frac{2}{\pi}} \frac{E_0 w_1}{w_s} \exp[-jkz_1 - \frac{jk}{2q_1} r^2], \tag{81}$$

or

$$E_1(x, y, z_1) = \sqrt{\frac{2}{\pi}} \frac{E_0 w_1}{w_s} \exp[-jkz_1 - \frac{jk}{2q_1} (x^2 + y^2)], \tag{82}$$

$$\Delta\phi(x-d, y, t) = \frac{2\pi}{\lambda} l \frac{\partial n_1}{\partial T} T_1(x-d, y, t) \tag{83}$$

for the model in a flowing medium,

$$\Delta\phi(r, t) = \frac{2\pi}{\lambda} \int_0^l \frac{\partial n_1}{\partial T} T_1(r, z, t) dz \tag{84}$$

for the model considering pump beam divergence,

$$\Delta\phi(r, t) = \frac{2\pi}{\lambda} \left\{ \int_{-l_0}^0 \frac{\partial n_0}{\partial T} T_0(r, z, t) dz + \int_0^l \frac{\partial n_1}{\partial T} T_1(r, z, t) dz + \int_l^{l+l_2} \frac{\partial n_2}{\partial T} T_2(r, z, t) dz \right\} \tag{85}$$

for the three-layer model, and

$$\Delta\phi(r, t) = \frac{2\pi}{\lambda} l \frac{\partial n_1}{\partial T} T_1(r, t) \tag{86}$$

for the model considering sidewall. Here E_0 and w_1 are the central electric field amplitude and radius ($1/e^2$ field intensity) of the probe beam waist. w_s is the radius of the probe beam in the sample. q_1 is the complex radius of the probe beam defined as $1/q_1 = 1/R_1 - j\lambda/(\pi w_s^2)$. R_1 is the curvature radius of the wavefront of the probe beam at the sample plane, $R_1 = z_1[1+(z_c/z_1)^2]$, and $w_s = w_1[1+(z_1/z_R)^2)]^{1/2}$, with $z_R = \pi w_1^2/\lambda$ the Rayleigh range of the probe beam. The mode-mismatching degree is defined as $m = (w_s/a_e)^2$.

It should be noted that in Eqs. (77) – (86), the thickness of the TL element is assumed to be infinitesimal, as treated in previous TLS theories, which means that the incident and exit planes of the probe beam with respect to the TL element are identical and the TL element just changes the phase of the probe beam at position z_1. But actually, every TL element should have a certain thickness. At cases when z_1 is much larger than the thickness of TL element, the previous "infinitesimal" assumption is reasonable. However, when z_1 is comparable to or even smaller than the thickness of TL element (usually the case in laser-excited TLM), the TL element may have a more complicated effect on the probe beam, such as there may exist different z_1s for different thin TLs (if we treat this "thick" TL as a combination of many thin TLs). Therefore, in this research, a term "finite TL element" is used to emphasize that the thickness of TL element should be considered where the infinitesimal TL element is not valid any more. Due to the difficulty of theoretically describing the probe beam diffraction by a finite TL element, we will still use the above theory for theoretical calculations.

In the detection plane, the intensity profile is obtained by taking the complex square of the electric field, that is

$$I_2(r_2, z_1 + z_2, t) = |E_2(r_2, z_1 + z_2, t)|^2, \tag{87}$$

or

$$I_2(x_2, y_2, z_1 + z_2, t) = |E_2(x_2, y_2, d, z_1 + z_2, t)|^2 . \tag{88}$$

When using a photodiode placed behind a pinhole to measure the central intensity of the probe beam, the TL signal S can be defined as

$$S = \frac{|S_{ac}|}{S_{dc}} = \frac{|I_2(t = n2\pi/\omega + \pi/\omega) - I_2(t = n2\pi/\omega)|}{I_2(t = 0)} , \tag{89}$$

where S_{ac} is the relative intensity change (RIC) of the probe beam in a modulation cycle. n is an arbitrary cycle in steady state. S_{dc} is the central intensity of the probe beam before excitation.

In the next sections, optimizations for the laser-excited and the ILS-excited TLM intruments with respect to different systematical parameters are made both theoretically and experimentally. For numerical simualtions, based on the theoretical models derived above, fortran programs were written, compiled in Fortran Powerstation 4.0 (Microsoft Developer Studio), and run on a Mac mini with Windows XP operating system. Every numerical integration is performed with Gaussian integration algorithm. These programs are available for free on request.

4.2 A laser-excited TLM

As shown in the theoretical models of previous section, the TL signal in micro space may be influenced by different factors, including the sample cell, flow of the sample and optical configurations of the pump and probe beams. For the laser-excited TLM, impacts from the surroundings of the sample were neglected. Because at high modulation frequencies, the TL signal is only slightly influenced by the sample cell when sample length is such as 100 μm. If a sample length of less than 10 μm is used, the impacts from the surroundings should be considered. Based on the laser-excited TLM as shown in Fig. 11, the TL signal caused by a divergent pump beam in static mode was analyzed first, and then, the signal in a microfluidic chip was investigated as well. During these processes, ferroin solutions were used as the sample, on which the optimal optical configuration of the TLM, corresponding to maximized sensitivity and reduced noises, was found. Then, as an application of the system, Cr(VI) was detected in the microfluidic-FIA-TLM setup.

4.2.1 Experimental preparations

4.2.1.1 Change of pump and probe beam parameters under an OL

In pump/probe beam TLS configuration, the pump and probe beams should be mismatched to obtain a high sensitivity, and one of the parameters closely correlated with the mode-mismatching degree is z_1. In laser-excited TLM, z_1 is usually on the scale of ~10 μm. To obtain an appropriate adjustable range of z_1 without changing the beam waist w_1 of the probe beam too much, parameters of beam expander I (Fig. 11), namely focal lengths of L1 and L2, should be carefully chosen. For the pump beam, to investigate the TL signal under excitation of a light with different divergence, different pump beam waist radii from 0.7 to 4 μm under the OL were employed. To achieve these different pump beam waists without changing the focusing position in the sample cell too much, parameters of beam expander II, namely focal lengths of L3 and L4, should also be carefully selected.

According to the propagation of Gaussian beam in a TLM system (section 4.1.1.1) and the already known systematical parameters (lasers, distances between optical elements, OL), focal lengths of L1 and L2 are determined as 4 and 15 cm, respectively. From Fig. 32(a) we can see

that while the beam waist w_1 changes only by about 20%, variation of the waist position up to 100 μm is enough for the optimization of z_1. Focal lengths of L3 and L4 are selected as 3 and 5 cm, respectively. Figure 32(b) gives the change of the pump beam waist radius when moving L4 in beam expander II. The beam sizes were measured by the knife-edge method. In this figure the change of waist position, which can be up to ~300 μm according to numerical simulation, is not given, but one more important parameter — the change of the power of the pump beam after the OL is presented. It is shown that at smaller pump beam waist, the pump laser power is also lower. This is because to reach the diffraction-limited focusing under the OL, expansion of the pump beam by expander II induces loss of the peripheral light of the beam by the limited clear aperture of the OL. Similarly, for the conventional TLS, focal lengths of two lenses L6 and L7 were chosen as 5 and 10 cm, respectively.
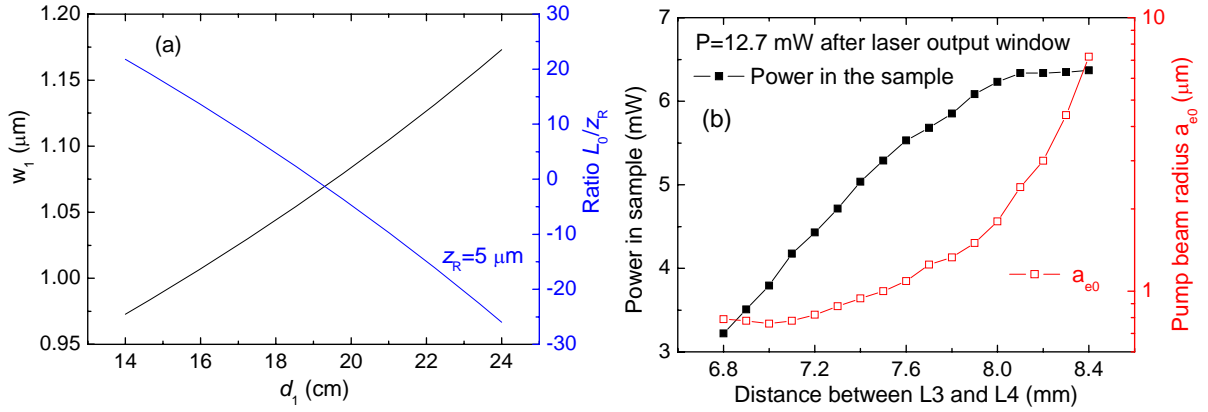
Figure 32: (a) Probe beam parameters after a 20×/NA 0.40 OL with the change of d_1, where d_0=0.15 m, f_1=0.04 m, f_2=0.15 m, d_2=0.2 m, and (b) power and beam radius change of the pump beam after the same OL at different d_{1e}s, where d_{0e}=0.95 m, f_3=0.03 m, f_4=0.05 m, d_{2e}=0.4 m. z_R is the Rayleigh range of the probe beam at w_1=1 μm and L_0 is the distance with respect to the centre (corresponding to d_1=19 cm) of an adjustable range of the probe beam focusing position.

4.2.1.2 Preliminary alignment of the system

Because the TL signal is directly related to the TL element-induced diffraction of the probe beam, which is detected by a fixed detector, the probe beam is employed as the reference beam to which the pump beam can be aligned. Procedure of preliminary alignment of the laser-excited TLM is as follows:

(1) First, according to the height of the lens in beam expander I, fix M5 to a proper position on the pole (Fig. 11). Then adjust the M4 and M5 to allow the probe beam to go through the centers of the two lenses L1 and L2. By shifting the lens mount along the optical path, the probe scheme after the OL can be changed without much interference to the original light path. The same process is used for the pump beam when it goes through the beam expander II.

(2) At the dichroic mirror, the pump and probe beams should be aligned coaxially by checking their overlapping at two positions one meter apart. Make them propagate in a direction perpendicular to the optical table, and mark their spots on the table surface using a sheet of concentric circle-printed paper. Then, put the OL in and make the expanded light spot fall on the center of the concentric circles. The same process is used for the condenser lens L5 (Fig. 11). Then add the guiding mirror M6 to lead the probe beam to the detector, which is about 15 cm away from the lens L5. The detector is mounted on a two-dimensional (2-D) stage. Adjust the 2-D stage and make the light intensity behind the pinhole achieve maximum by checking the DC signal from the detector with a multimeter. A pinhole with diameter (d_{ph}) of 4 mm is used.

4.2.1.3 Examination of TL signal

To find and obtain a stable TL signal, the procedure of checking the noises and finding the TL signal is as follows:

(1) Without the sample, block the pump beam, and check the noise of the detector induced by the probe beam when the optical isolator is on or off, and it is usually less than 0.1 μV at 1 kHz at d_{ph}=4 mm if there is no reflected or stray light back into the probe laser cavity; then, in a reversed way, block the probe beam and check the noise induced by the pump beam (there should be no noise from the pump beam); and then, both the pump and probe beams are open, check the noise again to see if there is some additional noise, which may be caused by the strayed or reflected light of the pump beam back into the probe laser cavity. Load the sample on the stage, check the noise in the same way as stated above.

(2) Adjust M3 and the z-position of the 3-D sample stage, make the TL signal maximum. According to the absorbance and the power fluctuation, estimate if the instability of the TL signal is reasonable. For example, if the power fluctuation is less than 1%, an instability of the TL signal less than 2% can be regarded as reasonable for a sample with stable and moderate absorption to the excitation light (such as 100 μM ferroin solution in a 100 μm sample cell, corresponding to an absorbance of 0.01 AU at 514.5 nm).

In Fig. 33, the TL signal of 500 μM ferroin solution in a 100 μm sample cell is given. From the curve we can see that the TL signal is highly stable over a period of 300 s.
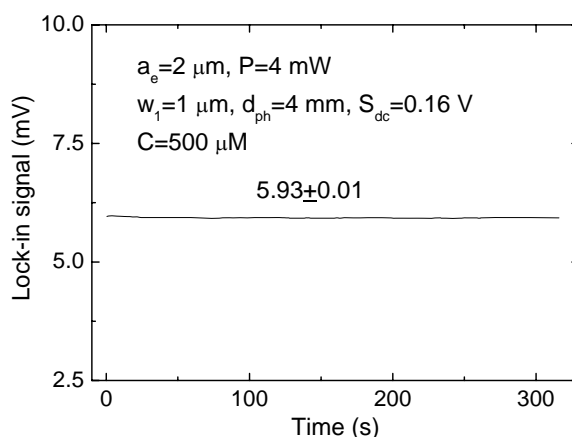
Figure 33: TL signal of ferroin solution as a function of time in a 100 μm sample cell.

4.2.2 TLS in a sample cell considering the excitation beam divergence

First, TL signal was first optimized for a static sample. For the detection by TLM, when a low mass LOD is required, the excitation beam can be focused as tightly as possible as long as no negative effect (such as photodegradation) happens. But, if a low concentration LOD is desired, the excitation beam radius needs to be optimized to get the maximum sensitivity for a given sample length. Experiments have revealed that optimization of the TLM system should not just focus on the optical configuration and sample thermophysical properties, but also should consider the sample length. Different sample lengths may correspond to different optical configurations.

4.2.2.1 Numerical simulations of temperature distributions

The TL signal is determined by the AC temperature distribution in the sample. Hence, the temperature profiles for two excitation beam radii of 0.7 and 1.4 μm for a sample length of 100 μm were calculated and the results are shown in Fig. 34. Absorption coefficient of the

analyte is assumed to be 25.32 m^{-1}, which corresponds to ferroin of 10 μM. Thermophysical parameters of water were given in Table 3.
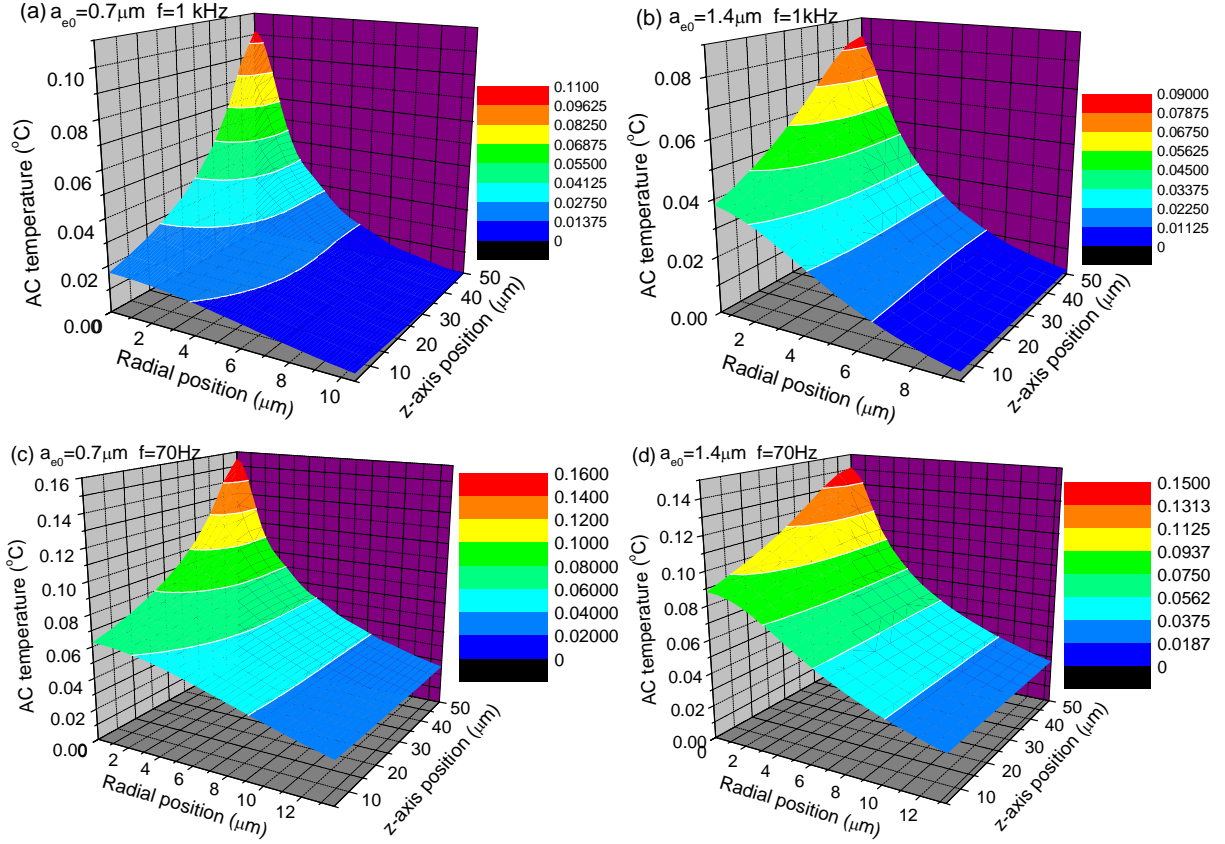
Figure 34: Temperature profile in the sample with sample length 100 μm under excitations of beams of (a) 0.7 μm, 1 kHz; (b) 1.4 μm, 1 kHz; (c) 0.7 μm, 70 Hz; (d) 1.4 μm, 70 Hz.

In Fig. 34, temperature profiles in the sample under different excitation conditions (pump beam radius, modulation frequency) are given. The time constant t_c is 8.57×10^{-7} s at a_{e0}=0.7 μm and 3.43×10^{-6} s at a_{e0}=1.4 μm. The thermal diffusion length $D_{th}=(D/\pi f)^{1/2}$ is 6.7 μm at 1 kHz and 25.3 μm at 70 Hz. The figure shows that at high modulation frequency (such as 1 kHz), the AC temperature profiles are mainly determined by the pump beam radius distribution along z-axis and also by the thermal diffusion in a modulation cycle. At lower frequency (70 Hz), the influence of the latter effect on the temperature is more obvious. Compared to excitation at 1 kHz, the temperature decreases less from the center to outer regions and the temperature profiles cover larger area. On the other hand, if comparing Figs. 34(a) and 34(b), we can see that the temperature peak at a_{e0}=0.7 μm is slightly higher (about 10%) than that at a_{e0}=1.4 μm, but the decrease of the temperature along z-axis is much greater than in the latter case, which means that the TL signal for a_{e0}=1.4 μm should be greater than that at a_{e0}=0.7 μm. As a result of this, we can suppose that for a given sample length, there should be an optimum a_{e0}, at which the TL signal achieves maximum. For higher detection sensitivity, the optimum beam size must be found.

Influences of different optical parameters, such as sample length, pump beam waist radius and detection scheme (w_1, z_1, d_{ph}), on the TL signal sensitivity and response linearity are now discussed. Results for conventional TLS are also given. The power of the laser in the sample was kept at 4 mW for the laser-excited TLM and conventional TLS setup. The modulation frequencies of 1.01 kHz and 30 Hz were used for the laser-excited TLM and conventional TLS, respectively. The signal from the photodiode before excitation (S_{dc}) is 0.16 V. In sections 4.2.2.2-4.2.2.5, 1 mM ferroin solution was used as the sample for the TLM and 10

μM for the conventional TLS. From sections 4.2.2.2 to 4.2.2.4, a pinhole of 4 mm was mounted before the detector to capture the TL signal in laser-excited TLS or TLM, while in section 4.2.2.5, influence of the pinhole size on the sensitivity and noise is discussed. In laser-excited TLM, an OL (20×/NA 0.40) was used to keep the probe beam waist radius w_1 around 1 μm when shifting the L2 in Fig. 11 to change z_1, and in sections 4.2.2.3, 4.2.2.4 and 4.2.2.6, w_1=2 μm produced by an OL (a single lens with focal length 15 mm) was also employed to demonstrate its superiority in sensitivity over w_1=1 μm for relatively long sample cell. For conventional TLS, w_1s=15~50 μm were produced after L8 with different focal lengths. The probe beam radius in the detection plane is about 1 cm in laser-excited TLM and TLS.

4.2.2.2 z_1-dependent TL signal in laser-excited TLM

The pump beam radius after the OL was changed by shifting the L4 in Fig. 11. When the L4 was moved to a distance of 7.1 or 8.05 cm away from the L3, a pump beam waist radius of 0.7 or 2 μm was achieved correspondingly. In Fig. 35(a), a schematic diagram of the optical configurations in the sample for a_{e0}=0.7 and 2 μm is drawn, in which, to differentiate the probe beam profiles, green TL element and curves are used for a_{e0}=0.7 μm while red TL element and curves are for a_{e0}=2 μm. The distance between the two TL elements resulting from the shift of the L4 is about 160 μm, as indicated by δz in Fig. 35(b). Planes "0" represent the central plane of the TL element. By moving the L2 in Fig. 11, d_1 (distance between the L1 and L2) was changed and correspondingly z_1 was altered. In Fig. 35(a), d_1=16.7 and 22 cm correspond to the positions of z_1=0 for a_{e0}=0.7 and 2 μm, respectively. In Fig. 35(b), the measured TL signals at different z_1s for these two pump beam radii are displayed. The experimental data are in agreement with the theoretical curve except for the positions of the optimum z_1 (z_{1opt}), where the TL signal achieves maximum. The maximum TL signal appears at larger z_1 than the theoretical prediction for both pump beam radii. Compared with the theoretical values of 25 and –40 μm for a_{e0}=0.7 and 2 μm, respectively, the experimental optimum distances appear at z_1=90 and –100 μm, corresponding to d_1 of 20 cm for a_{e0}=0.7 μm and of 18.5 cm for a_{e0}=2 μm, respectively, which are also depicted in Fig. 35(a). This is due to two reasons: one is the finite pinhole (4 mm) before the photodetector in contrast with theoretical calculations just at the central point; the other is the finite TL element as opposed to the infinitesimal TL element hypothesis as mentioned before (section 4.1.3.5). It should be noted that the optimum position of d_1 could be different if something is changed, such as the pump/probe beam wavelengths, the sample cell thickness or channel shape. For example, in section 4.2.3.3, where a microchannel with U-shape is used, the optimum d_1 is around 20 cm. Besides, we can find that TL signal at a_{e0}=2 μm is about 1.36 times higher than that at a_{e0}=0.7 μm. It should be noted that this signal enhancement is achieved under the same excitation power in the sample for both a_{e0}=0.7 and 2 μm. Practically, for a given laser output power, the power transmitted by the OL at a_{e0}=0.7 μm is lower than that at a_{e0}=2 μm. In the described system, a decrease of 1.45 times was found, as shown in Fig. 32(b).
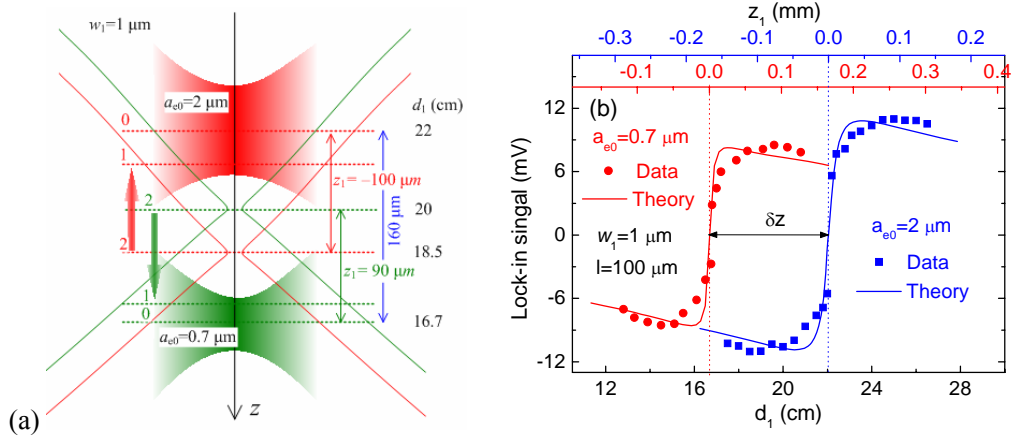
Figure 35: (a) Schematic diagram of optical configurations in the sample for two pump beam waist radii of 0.7 and 2 µm when shifting lens L4 in laser-excited TLM, (b) z_1-dependence of TL signals. The sample length is 100 µm.

From the discussion above we can see that for a certain sample length, focusing the pump beam to its diffraction limit is not always favorable from the point of view of sensitivity enhancement and power conservation. The sample length-dependent TL signals for a given pump beam parameters and the a_{e0}-dependent TL signals for a certain sample length will be presented, respectively.

4.2.2.3 Sample length-dependent TL signal in TL system

Figure 36 gives the sample length-dependent TL signals as well as theoretical predictions. We can see that for small sample lengths such as less than 100 µm, the TL signals are in agreement with those calculated in theory. If the sample length increases further, the TL signal becomes smaller than theoretical values. This difference comes from the fact that for a finite TL element, there exist different z_1s for different thin TLs (if we treat the finite TL as a combination of many thin TLs), and for those thin TLs away from z_{1opt}, the corresponding TL signals are smaller than those if they are located at z_{1opt} as assumed in theoretical calculations.. The confocal distance z_{ce} (two times of Rayleigh range z_{Re}) at $a_{e0}=2$ µm and $\lambda_e=514.5$ nm is 49 µm. By examining the figure we can find that the effective sample length (l_{eff}) for $a_{e0}=2$ µm is about 300 µm (ca. $6z_{ce}$).
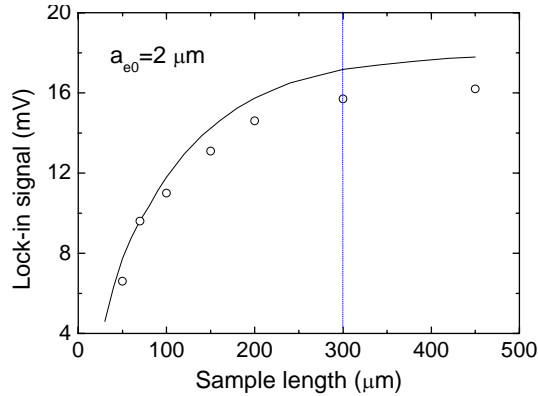
Figure 36: Sample length-dependent TL signals in the laser-excited TLM at $a_{e0}=2$ µm.

60

4.2.2.4 Optimum pump laser beam waist radius for a given sample length

The strength of TL element is determined by the power density and effective excitation length of the pump laser in the sample, both of which are dominated by the excitation beam waist radius a_{e0}. In Fig. 37, the TL signals at different a_{e0}s for three sample lengths, 100 μm, 300 μm and 1 cm, were measured. In conventional TLS [Fig. 37(b)], w_1 is comparable to the excitation beam radius, namely w_1=10~50 μm which was obtained by employing L8 (Fig. 11) with different focal lengths. For l=100 μm and 1 cm, the experimental data are in agreement with the theory. But for l=300 μm, the disagreement between the experimental data and theory is observed like for longer sample lengths in Fig. 36. The amplitudes of the TL signals at larger pump radii are smaller than predicted theoretically. When we examine the peaks of the curves, it can be found that the maximum TL signal appears at an optimum beam size where the confocal distance of the pump beam is approximately half of the sample length, namely z_{ce}=l/2. An empirical expression for the optimum excitation beam radius in a sample cell with length l can be written as:

$$a_{e0} = \sqrt{\frac{\lambda_e l}{4\pi}} \; . \tag{90}$$

Under optimal conditions the beam radius at the border of the sample cell, is $5^{1/2}a_{e0}$.
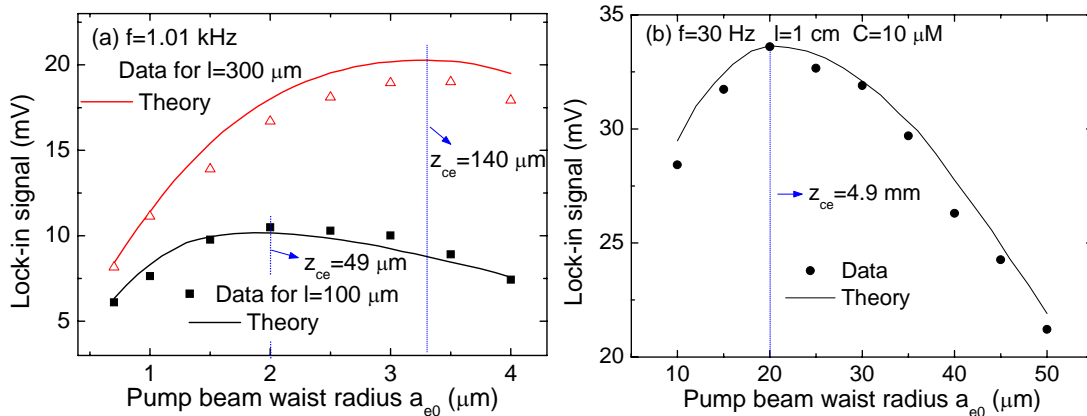
Figure 37: TL signal as a function of pump beam radius (a) in two microchannels of 100 and 300 um in laser-excited TLM, and (b) in a 1-cm cuvette in conventional TLS.

Furthermore, compared with the TL signal [the leftmost solid square in Fig. 37(a)] at diffraction limit of the pump beam (a_{e0} = 0.7 μm) which was often applied in TLM, the maximum signal is 1.36 times higher for 100-μm sample length and 2.3 times higher for 300-μm sample length, respectively, while the power density in the sample is only 1/10 or 1/20 of that at the diffraction limit for l=100 or 300 μm, respectively. Therefore, for micro cells with relatively long sample length, instead of focusing the pump beam to its diffraction limit, the optimum pump beam radius should be employed to assure not only higher detection sensitivity but also much lower power density in the sample to alleviate the possibility of degradation of the analyte.

4.2.2.5 Influence of the pinhole size on the TL signal

In the previous section, the sensitivity was optimized by choosing a proper pump and/or probe beam radius for a given sample length, where the pinhole before the detector was fixed at 4 mm. According to Ref. 109, the pinhole size not only impacts the signal amplitude captured by the detector but also the noise level of the detector caused by the transmitted light. In this section, the signal-to-noise ratios at different pinhole sizes are presented.

At first, response of different parts of the detection plane of the photodetector to certain TL signal after a fixed pinhole was checked, as shown in Fig. 38(a). From the figure we can see that except for the peripheral part, the detection plane has almost homogenous response to light intensity change along x_2 or y_2 direction. To further verify the response homogeneity of the detection plane, TL signals at different pinholes were examined. Pinholes of 0.25, 0.7, 1, 1.8 and 4 mm were placed at a distance where the probe beam radius is about 4 cm. The corresponding pinhole-to-beam size ratio is not more than 0.05, namely $d_{ph}/(2w_2) \leq 0.05$, to assure that only the central part of the probe beam is detected. TL signals were calculated according to Eq. (89), in which background signal of the detector was considered when determining S_{dc} as stated in the "**Detector**" part in section 3.1 (page 34). As exhibited in Fig. 38(b), the TL signals are similar for different pinholes.

Then, the signal-to-noise ratios (S/N) at different pinholes were checked as shown in Fig. 38(c). In S/N calculation, the signal is taken as the relative intensity change (S_{ac}) of the probe beam after certain pinhole and the noise as the standard deviation of the probe beam noise when there is no pump beam excitation. From the figure we can see that both changes of the noise and the S/N with $d_{ph}/(2w_2)$ in this laser-excited TLM are similar to the shot-noise-limited case shown in Ref. 109, but the maximum S/N appears at smaller $d_{ph}/(2w_2)$ of about 0.35 in comparison to 0.57 predicted in Ref. 109. This is probably because of two reasons: one is that at the modulation frequency of 1.01 kHz used in this work, flicker noise still influences the signal, which causes the optimum $d_{ph}/(2w_2)$ to shift to smaller values; the other reason is that as displayed in Fig. 38(d), the relative intensity change S_{ac} in the detection plane is mostly localized in the region of $r_2 < 0.5w_2$, which is smaller than that of $0.7w_2$ in Ref. 109.
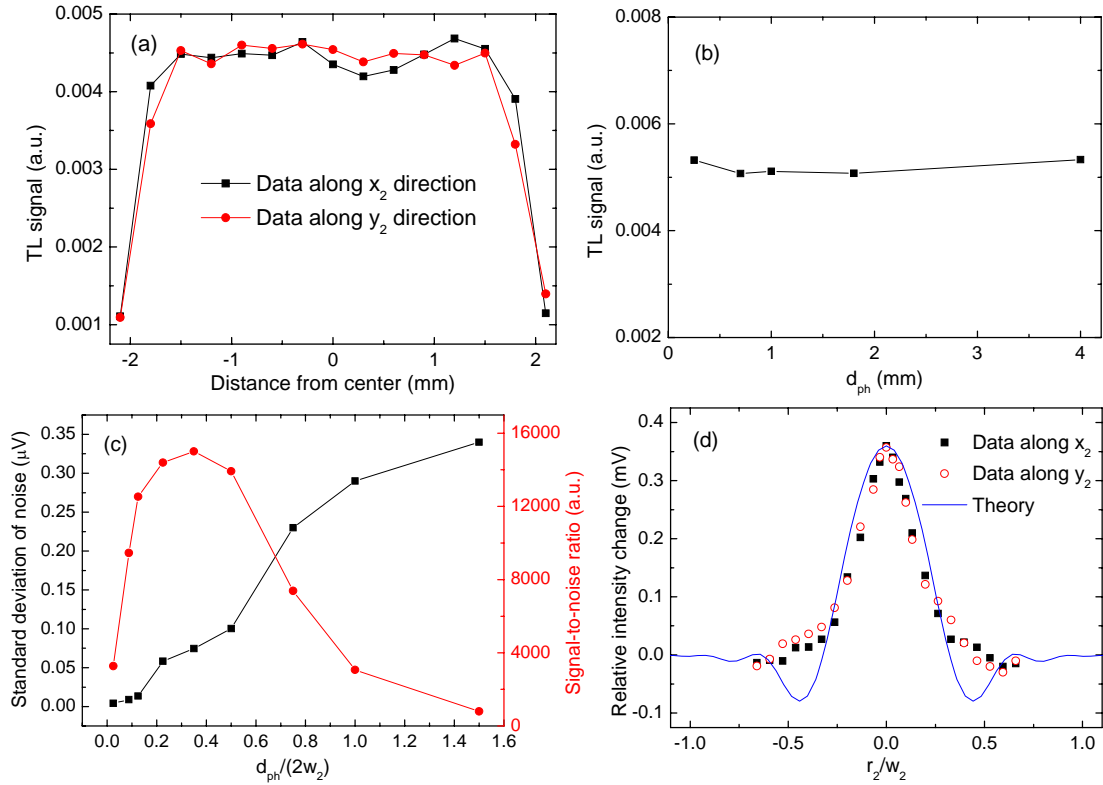
Figure 38: (a) Response of the detection plane in the detector to TL signal behind a 250-μm pinhole, (b) TL signal behind different pinholes at a detection distance where w_2=4 cm, (c) probe beam noise and singal-to-noise ratio as a function of $d_{ph}/(2w_2)$, and (d) relative intensity change of the probe beam in the detection plane. The sample is 100 μM ferroin in a 100 μm sample cell.

The pinhole-to-beam size ratio is 0.2 for the initially selected pinhole of 4 mm with respect to the probe beam size of 2 cm in the detection plane. At this ratio the S/N approaches the maximum as indicated in Fig. 38(c).

4.2.2.6 Signal linearity and detection limits of the instruments

In Fig. 39, the calibration curves for different combinations of (w_1, d_1, l) are shown. For l=100 μm, a_{e0} is set to be 2 μm and for l=300 μm a_{e0} is 3.3 μm. When checking the signal linearity at different d_1s (or z_1s) for w_1=1 μm and l=100 μm, it was found that at smaller z_1, such as at d_1=20.8 cm [plane "1" in Fig. 35(a)], the TL signal shows a non-linear response over a relatively wide concentration range such as 2 orders of magnitude or higher, as indicated by the red data points and line in Fig. 39. This is maybe due to the following reason: for a finite TL element, at small z_1, such as plane "1" in Fig. 35(a), one part of the TL element converges the probe beam while the other diverges it. This complicated effect makes the TL signal response nonlinear over a wide concentration range. Therefore, optimization of the probe beam parameters is quite necessary not only for a lower LOD but also for a better signal linearity. At power P=4 mW in the sample, the LOD for the ferroin solution detection in batch mode is calculated as 8.7×10^{-9} M (l=100 μm) for laser-excited TLM.
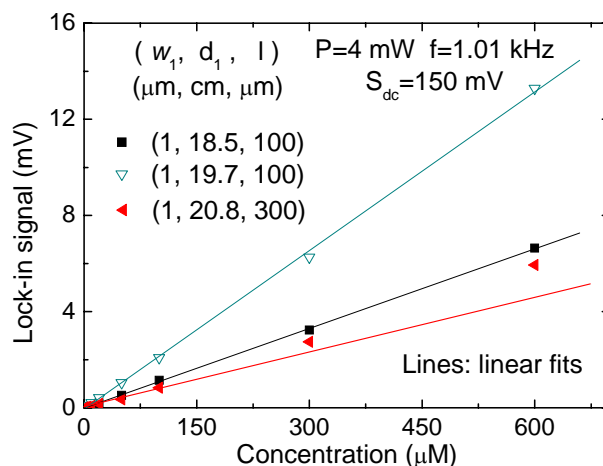
Figure 39: Calibration curves for ferroin solution under different pump beam radii and detection schemes.

4.2.2.7 Brief summary

Above, TLS under excitation of a divergent pump beam was discussed in static mode. An optimal pump beam radius for laser-excited TLM or TLS was proposed for a certain sample length. At this optimal pump beam radius, the sensitivity achieves maximum at over ten times lower power density in the sample compared to the excitation at diffraction limit of the pump beam. Upon detailed analysis of the influence of a TL element with finite thickness on the TL signal in laser-excited TLM, suggestions for selection of an optimum detection scheme to obtain a lower LOD and a better signal linearity were made. In practical applications, this will help to optimize TLS systems for macro- or micro-scale detection of different analytes. TLS in static mode is applicable to analyte detection in sample cells or microwells where no liquid flow occurs. If the TLS/TLM is applied to detection in flow systems such as FIA or microfluidic chips, influence of the flow of the sample on the TL signal should be considered, as discussed in the next section.

4.2.3 TLM on a microfluidic chip

After mounting the microchip as well as the gravity-driven pump under the TLM, the TLM signal in a microfluidic channel was investigated. The impacts of sample flow and experimental parameters (such as pump beam waist radius, pump-probe beam offset, detection scheme, and the like) on the temperature and the TL signal are described in the following sections.

4.2.3.1 Numerical simulations of temperature rise and TL signal

Some parameters used in the numerical simulations were chosen as follows: power of the excitation light is 10 mW; absorption coefficient of the analyte is 25.32 m^{-1}. Unless otherwise stated, probe beam parameters of (w_1=1 μm, z_1=-15z_R, z_2=2 cm) were used.

Figure 40(a) shows the temperature distributions at several flow velocities. Because the modulation frequency is high (1 kHz), the temperature profiles at v_x less than 1 cm/s change a little compared to that at v_x=0. With increasing the flow velocity, the temperature is obviously influenced by the flow of the sample, and the maximum of the temperature profiles shifts in the direction of the flow. In this research, v_x=10 cm/s is regarded as a high flow velocity while v_x<1 cm/s is regarded as a low velocity.
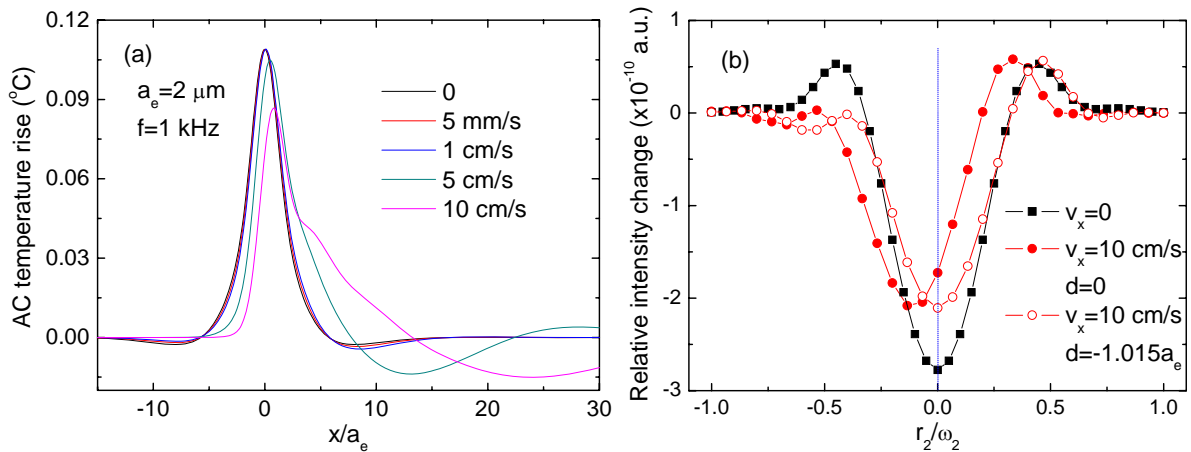
Figure 40: Influence of different flow velocities on (a) the temperature distributions in *x* direction, and (b) the RIC distributions in x_2 direction at *d*=0 and *d*=d_{opt}..

Corresponding to the temperature distributions, the RIC distributions of the probe beam are given in Fig. 40(b). It shows RIC distributions at flow velocities of 0 and 10 cm/s. We can see that if the excitation and probe beams are coaxial (*d*=0), the peak of RIC at high flow velocity shows a deviation from the central position. The higher the flow velocity, the larger the deviation is. To get maximum signal at central point of the probe beam in detection plane, the probe beam should be displaced downstream a certain distance to fit the change of the temperature distribution. As shown by the open circle curve, if the probe beam moves along the direction of the flow by 1.015a_e for v_x=10 cm/s, the peak of RIC will again coincide with the central point of the probe beam. This optimum beam offset for certain v_x is denoted by d_{opt}, such as d_{opt}=-1.015a_e for v_x=10 cm/s. In experiment, we can move one of the beams (usually excitation beam for convenience) to achieve the maximum RIC in the central axis of the probe beam.

In Fig. 41(a), variations of TL signals with z_1 are presented. The optimum value of z_1 (denoted by z_{1opt}), for which the TL signal reaches its maximum, becomes smaller with the increase of the flow velocity. In the investigated flow velocity range, z_{1opt} can be found between 10z_R and 20z_R for z_1>0 or between -10z_R and -20z_R for z_1<0. This shows that TL signal in microspace

behaves differently from the generally accepted TLS theory predicting optimal position at $z_1 = \pm\sqrt{3}z_R$, which is indeed accepted by some authors for the case of TLM [13]. The TL signal at $z_1 < 0$ and $z_1 > 0$ has similar behavior with the change of z_1. When the probe beam is displaced to d_{opt}, the detected TL signal is higher. The higher the flow velocity, the larger the signal difference is. For example, at $v_x = 10$ cm/s, the TL signal at d_{opt} is about 1.2 times higher than that at $d=0$.
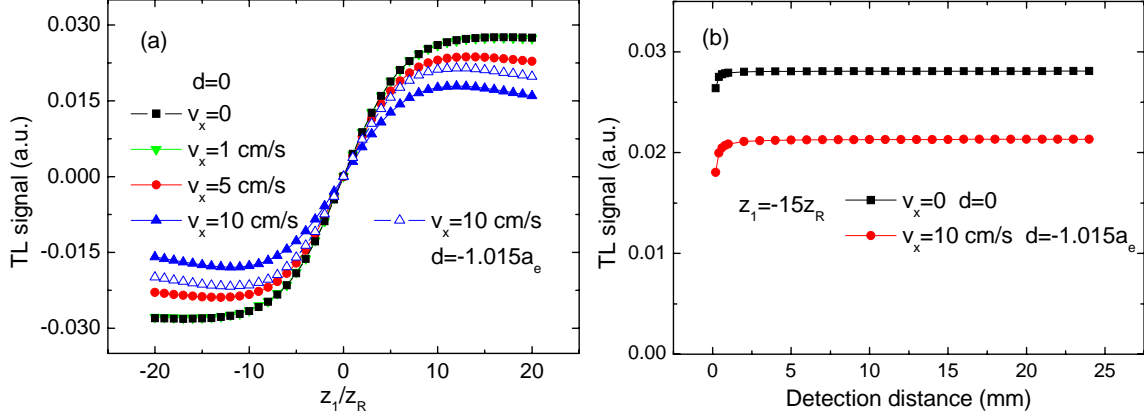
Figure 41: TL signals as a function of (a) z_1 and (b) detection distance at different velocities at $d=0$ and $d=d_{opt}$. The signal at $z_1 < 0$ is negative, which means the phase of signal is opposite to that at $z_1 > 0$.

Figure 41(b) exhibits the TL signals as a function of detection distance (z_2 in Fig. 31) at flow velocities of 0 and 10 cm/s. The TL signal varies quickly in small detection distances, and then reaches a nearly constant value when the detection distance further increases. From the variation of the signal we can see that at such a small excitation beam radius ($a_e = 2$ μm), the detection scheme is regarded as the far field detection. In the experimental apparatus, a condenser lens opposite to the OL was used to project the probe beam to a larger distance for the convenience of detection.

For the detection of samples at high flow velocities, influence of the fluctuation of the flow velocity on the TL signal must be taken into consideration. On the other hand, if the TLM is designed for multi-line or broad-band detection, in which a multi-line laser is employed as the excitation source, the change of the excitation beam radius in the sample caused by the aberration of the OL should be taken into account. The fluctuation of the excitation beam radius may also occur in case of poor beam pointing stability or mode instability of the light source. Figure 42 presents the sensitivity of TL signal to the fluctuations of the flow velocity and the excitation beam radius. Here, two distances of $z_1 = -8z_R$ and $-20z_R$, where the TL signals are similar as shown in Fig. 41(a), are used to represent two detection schemes with different mode-mismatching degrees $\{m=(w_s/a_e)^2$, with w_s being the beam radius of the probe beam in the sample: $w_s = w_1[1+(z_1/z_R)^2]^{1/2}\}$. For $w_1 = 1$ μm and $a_e = 2$ μm, the degree of mode-mismatching is 16 at $z_1 = -8z_R$ and 100 at $z_1 = -20z_R$, respectively.

In Fig. 42(a), 10 cm/s is regarded as the reference velocity v_{xr} (corresponding TL signal is S_0). From the figure we can see that the TL signals at $z_1 = -8z_R$ are less sensitive to the variance of flow velocity. When the flow velocity changes 10%, the TL signal varies less than 1% for $z_1 = -8z_R$, but for $z_1 = -20z_R$ the variation approaches 6%. Thus a relatively smaller z_1 is beneficial when the flow velocity fluctuates. In Fig. 42(b), 2 μm is regarded as the reference radius a_{er} (corresponding TL signal is S_0). The TL signals at larger z_1 are less sensitive to the variation of excitation beam radius. When the beam radius varies 10%, the corresponding signal change at $z_1 = -20z_R$ is about 1.4% whereas it is above 4.4% at $z_1 = -8z_R$. Therefore, if the variation of pump-beam radius is relatively large, a relatively large z_1 should be employed. Based on the above discussions, it is seen that by choosing proper detection scheme (smaller

or larger z_1 around z_{1opt}), changes of TL signal due to the fluctuation of flow velocity or excitation beam radius can be reduced.
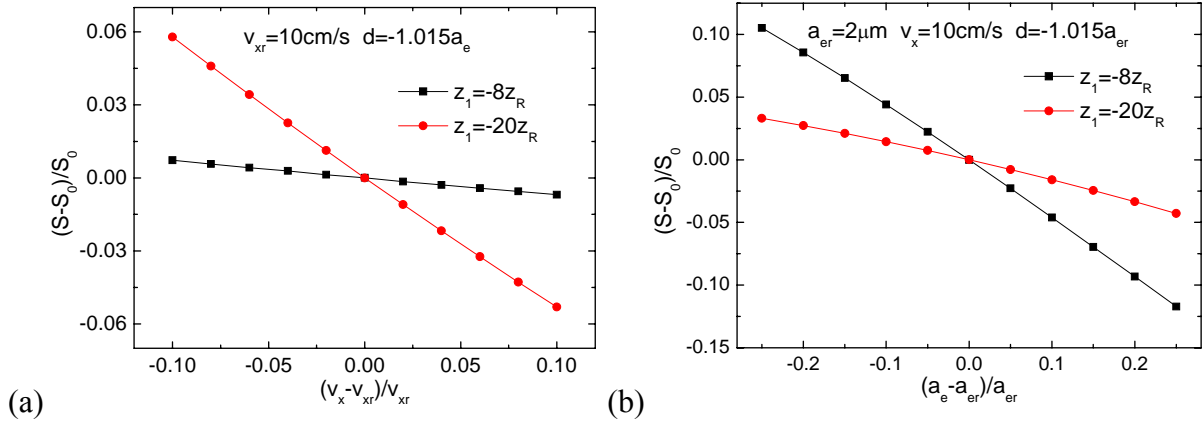
Figure 42: Relative TL signal change as a function of (a) fluctuation of the flow velocity relative to reference flow velocity v_{xr}=10 cm/s and (b) variation of the pump-beam radius relative to reference beam radius a_{er}=2 μm, at z_1=-8z_R and -20z_R, respectively.

4.2.3.2 Combination of microchip and TLM

Due to the localization of the sample in the microchannel, we can easily judge the position of the pump or probe beam in the microchannel by moving the sample stage and observing the change of the beam spot after the microchannel, and therefore it is much easier to find the TL signal compared to in a sample cell [Fig. 15(a)]. As shown in Fig. 43(a), the bottom of the channel is a semicircle, which will change the light profile/pattern and propagation path after the channel. By comparison between the detection schemes at z_1>0 (green curves) and z_1<0 (red curves), it is obvious that the distance z_1 is better to be negative. In this case the probe beam after the channel is less changed by the curved channel, reducing the possibility of curved wall-induced deterioration of the TL signal linearity.
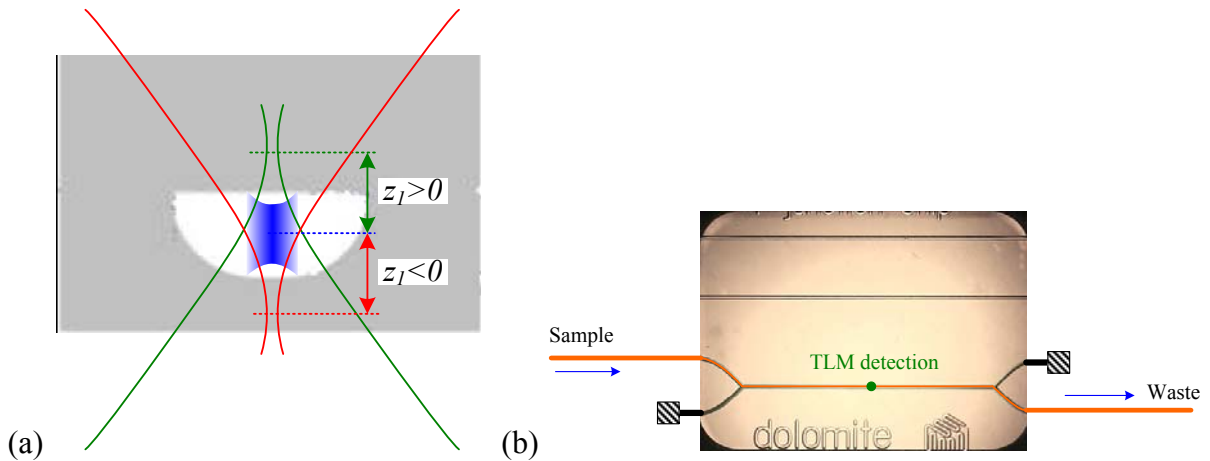
Figure 43: (a) Detection scheme in the microchannel for both z_1>0 and z_1<0, and (b) connection of the microchip and tubings of Connection I, where the green spot denotes the TLM detection site.

A microfluidic-TLM system was constructed based on a gravity-driven pump. In the first step, to optimize the optical configuration of TLM in a flowing medium, "Connection I" was used, as shown in Fig. 43(b). The depth of the microchannel is 100 μm. For experiments described in sections 4.2.3.3-4.2.3.5, the concentration of the ferroin solution is 300 μM, and the excitation power in the sample is 4 mW. S_{dc}=0.15 V.

4.2.3.3 Dependence of TL signal on the distance d_1

In Fig. 44, the TL signals for different d_1s at v_x=0 and 52 mm/s are shown. d_1 is the distance between lenses L2 and L1 (Fig. 11). For v_x=52 mm/s, both d=0, d_{opt+} and d_{opt-} were considered. Here, d_{opt+} was the optimum beam offset when the flow ran from the carrier reservoir to the waste reservoir and d_{opt-} when the flow was in reverse. To realize such an offset (d_{opt+} or d_{opt-}) between the pump and probe beams, the pump beam was shifted by d_{opt+} or d_{opt-} along the direction opposite to the sample flow. From the figure we can see that at v_x= 52 mm/s, the maximum TL signal at d_{opt} is about 1.11 times larger than that at d=0. The small difference between the TL signals at d_{opt+} and d_{opt-} indicates the imperfect symmetry of the probe beam in the detection plane, and the improvement to the TL signal seems a little bit better for the d_{opt-} than that for d_{opt+}. In the next from sections 4.2.3.4 to 4.2.3.7, d_1 is 20 cm for a_e=2 μm and 21 cm for a_e=0.7 μm, respectively.
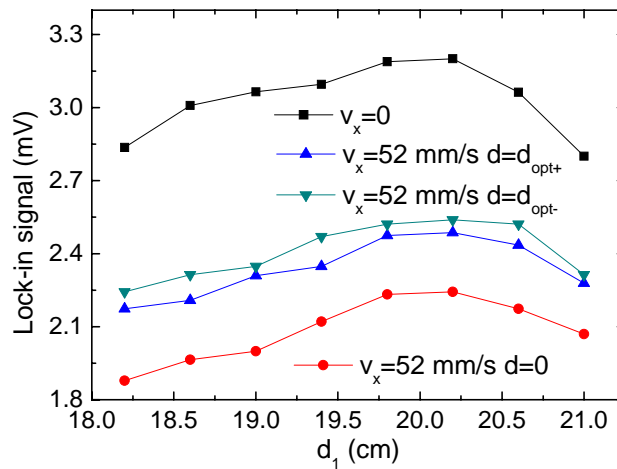
Figure 44: TL signal as a function of d_1 for v_x=0 and 52 mm/s at a_{e0}=2 μm.

4.2.3.4 Dependence of TL signal on the flow velocity

In Fig. 45, TL signals as a function of the flow velocity in the microchannel for two pump beam waist radii of 0.7 and 2 μm are shown. Both the signals at the beam offsets of 0 and d_{opt} were measured. From the figure we can see that the TL signal decreases faster with the flow velocity than the theoretical predictions. This is because of the inconsistency of the flow profiles between the experiment and the theory: in experiment, the flow in the microchannel is laminar flow, and the flow velocity used in the abscissa of the figure is the average value of the flow distribution in the cross section of the microchannel; while in theory, the flow was assumed to be homogeneous. This means that the flow velocity of the most central part of the fluid, where the excitation power density is the highest and major part of the TL signal is generated, is larger than the average flow velocity v_x. Therefore, in experiment, at certain v_x, a bigger reduction of the signal compared to theoretical prediction occurred. On the other hand, we can see that the TL signal at a_e=2 μm is about 1.4 times higher than that at a_e=0.7 μm, which has been demonstrated in section 4.2.2.2. At low flow velocities, such as v_x<1 cm/s, the detection scheme can be kept unchanged, but if the flow velocity increases to a high value (such as above 2 cm/s), it is necessary to readjust the detection scheme to achieve the maximum TL signal.
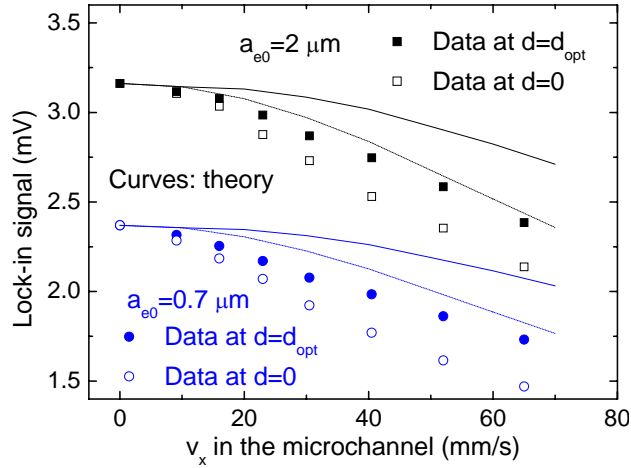
Figure 45: TL signal as a function of flow velocity in the microchannel for two pump beam profiles at two beam offsets.

4.2.3.5 Dependence of TL signal on the offset of the pump beam waist relative to its optimum location

The change of the TL signal with the offset of the pump beam waist relative to its optimum location is shown in Fig. 46. In the abscissa axes of Fig. 46, the change of the focusing position of the pump beam with respect to the movement of the microchip has been considered according to section 4.1.2. According to the signal-contributing length of $6z_{ce}$ for a certain pump beam waist a_{e0} given in section 4.2.2.3, at $a_{e0}=2$ μm, the TL signal doesn't change by more than 20% even when the cell was moved upward or downward by 100 μm, but in flow mode of $v_x=52$ mm/s, the decrease is about 3 times higher than in static mode. This is because when the pump beam waist is moved away from the optimum position, the function of d_{opt} is also broken to some extent. The non-symmetric shape of the curves with respect to the optimum position z_{opt} is due to the fact that when the sample cell moves upward or downward, the center of the TL element is shifted, and correspondingly, one of the probe beam parameters, i.e. z_1, is changed. At $z_1<0$, $|z_1|$ is larger when the microchip moves upward than that when the microchip moves downward, vice versa for $z_1>0$. For $a_{e0}=0.7$ μm, the TL signal is localized in a much shorter sample length of ca. 40 μm. We can see that when the microchip was moved upward or downward by 30 μm with respect to the center of the microchannel, the TL signal changes less than 25%, but when the pump beam waist goes out of the channel, the signal decreased to zero rapidly.
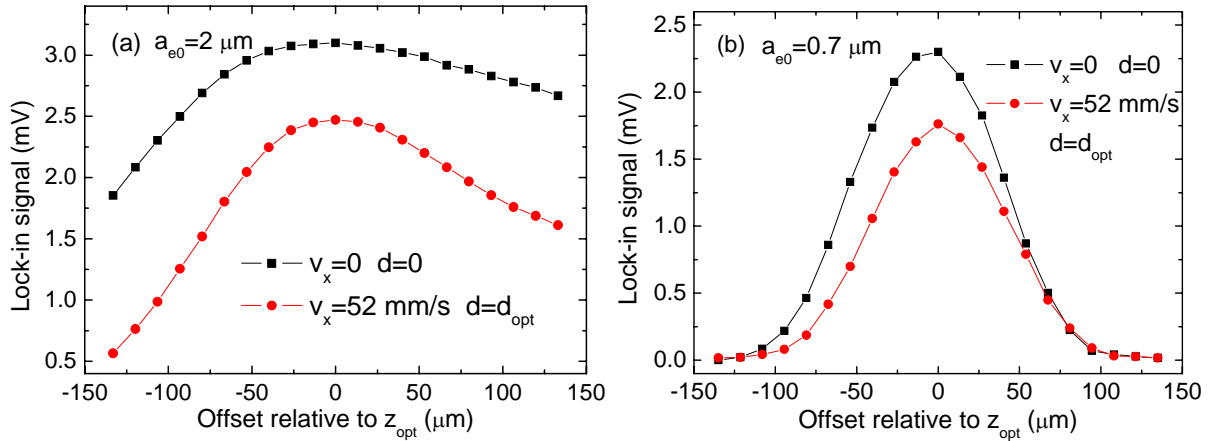
Figure 46: TL signal as a function of offset of the pump beam waist radius relative to its optimum location in the microchannel at (a) $a_{e0}=2$ μm and (b) $a_{e0}=0.7$ μm.

68

4.2.3.6 Influence of the sample flow on the TL signal

Liquid flow in the microchannel deteriorates the TL signal from different aspects: one is that the flow moves the heat out of the detection area, which decreases the TL signal amplitude, as shown in Fig. 45. Another aspect is the fluctuation of the flow of the liquid, which not only makes the TL element unstable, but also interferes with the probe beam even if there is no pump beam excitation. As shown in Fig. 47(a), when the pump beam was blocked, the S.D. of the probe beam noise at different flow rates was checked. The figure shows that when the flow rate is less than 10 μL/min, there is slight deterioration of the probe beam noise, but at higher flow rates, the deterioration becomes very obvious. This deterioration comes from the disturbance of the liquid flow on the propagation of the probe beam through the microchannel, which can be induced by the fluctuation of the flow and/or the presence of some kind of micro- or nano-bubbles in the fluid. The flow-induced noise behaves like the noise caused by the beam pointing instability of the light source. As indicated by the black curve in Fig. 47(b), the probe beam noise varies with pinhole aperture-to-beam size ratio $[d_{ph}/(2w_2)]$ in a way similar to the case of beam pointing instability-induced noise [Fig. 1 in Ref. 109] except for less pronounced decreasing of the noise at large $d_{ph}/(2w_2)$. This is because in comparison to the only beam pointing instability-induced noise, there are other noises such as flicker and shot noises in the noise curve in Fig. 47(b), in which the shot noise becomes the major noise source at large $d_{ph}/(2w_2)$. Correspondingly, as predicted in Fig. 1 in Ref. 109 that the signal-to-noise ratio would not change with $d_{ph}/(2w_2)$ if only the beam pointing instability-induced noise exist in TLS sytem, the signal-to-noise ratio [red curve, Fig. 47(b)] doesn't change a lot (<35%, which is probably due to measurement error) at relatively small $d_{ph}/(2w_2)$ (such as <0.6) where the flow-induced noise dominates and then decreases at large $d_{ph}/(2w_2)$ where the shot noise is dominant. From the figure we can see that in flow-induced noise-limited TLS experiments, $d_{ph}/(2w_2)$ could be selected between 0.1 and 0.4 for high signal-to-noise ratio.
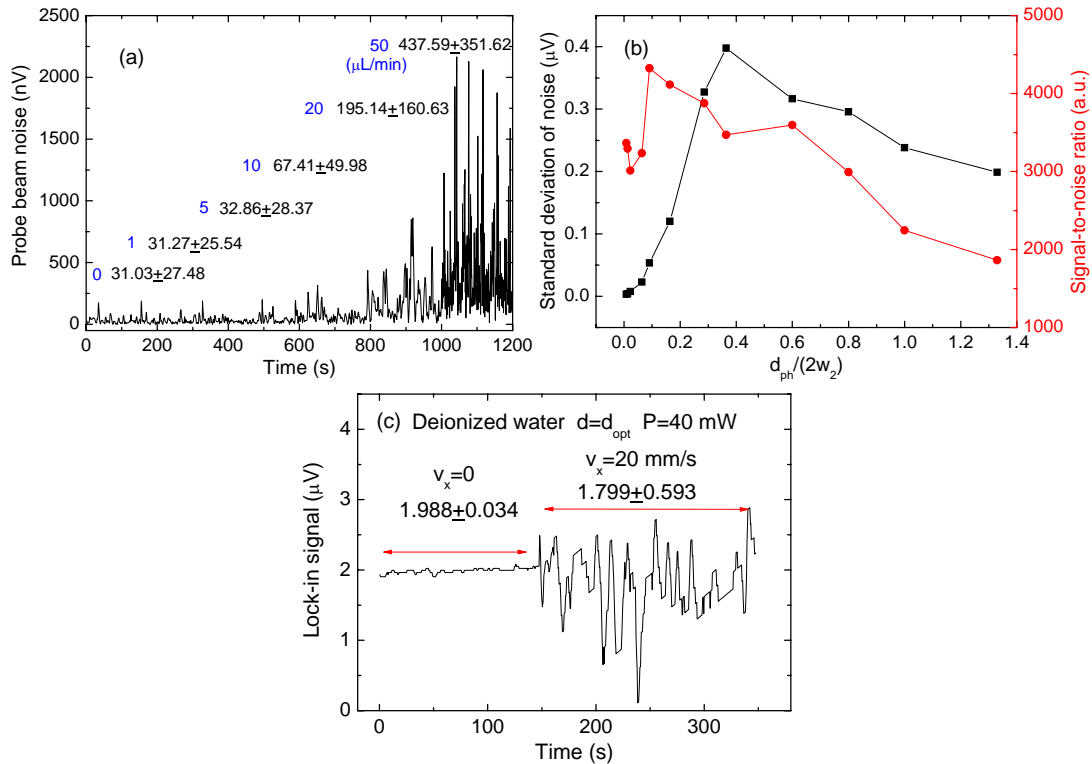
Figure 47: (a) Probe beam noise at different flow rates at $d_{ph}/(2w_2)$ of 0.3 when the pump beam is blocked, (b) probe beam noise and signal-to-noise ratio as a function of $d_{ph}/(2w_2)$ at flow rate of 20 μL/min, and (c) TL signal of deionized water at flow rates of 0 and 20 μL/min under excitation power 40 mW.

In Fig. 47(c), TL signal of deionized water was recorded, where the S.D. of the signal at flow rate of 20 μL/min (corresponding to flow velocity of 20 mm/s in microchannel) is about 0.6 μV. Part of this noise comes from fluctuation of the TL element resulted from the pump beam instability (power fluctuation, flow disturbance). Changing to smaller z_1 didn't decrease the noise as much as predicted in Fig. 42(a). This may be because in contrast to the infinitesimal pinhole hypothesis in theory, the finite aperture of the pinhole impairs the insensitivity of TL scheme with smaller mode-mismatching degree to the influence of flow disturbance, and furthermore, the noise from the pump beam instability at smaller mode-mismatching degree becomes higher [Fig. 42(b)].

4.2.3.7 TL signal linearity

In Fig. 48(a), the signal linearity for static and flowing sample modes is presented. The concentration range of ferroin used here is from 3 to 300 μM. In static mode, the signal increases linearly with the concentration of the sample. While for a relatively high flow velocity, as predicted theoretically in Fig. 48(b), the response at $d=0$ is not linear over a relatively large concentration range, a linear response is obtained at $d=d_{opt}$.
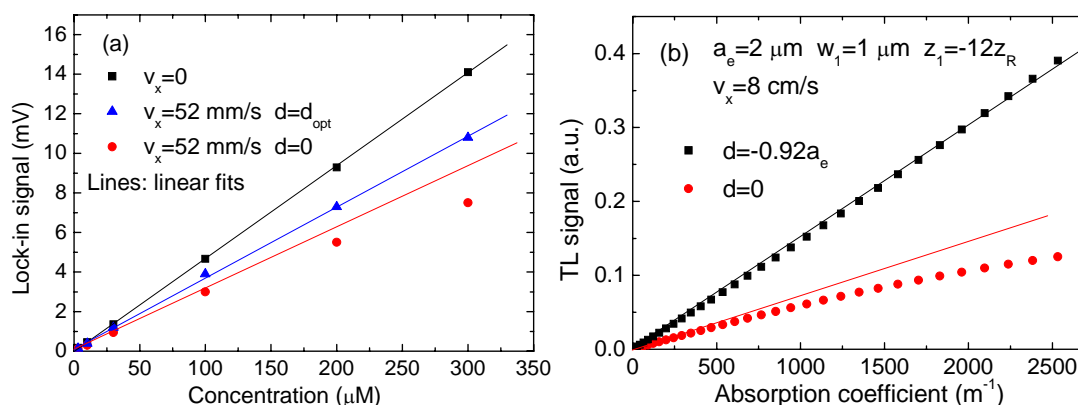
Figure 48: (a) TL signal linearity for $v_x=0$ and 52 mm/s without ($d=0$) and with beam offset ($d=d_{opt}$), $a_{e0}=2$ μm, $P=20$ mW. (b) Theoretically calculated TL signal as a function of absorption coefficient at $v_x=8$ cm/s for both beam offsets of 0 and -0.92a_e.

Therefore, during the experiment, it is quite desirable to move the pump beam to the optimum position to assure a linear response of the TLM to a certain range of sample concentration when the flow velocity of the sample is relatively high. The LOD for 100 μm ferroin solution at $v_x=52$ mm/s can be evaluated to be 6×10^{-8} M at $P=20$ mW, corresponding to an absorbance of 7×10^{-6} AU.

4.2.4 Microfluidic-FIA-TLM for the detection of Cr(VI)

Cr(III) is considered as an essential micronutrient for humans, whereas Cr(VI) is a potential carcinogenic agent. Total Cr content in surface water is typically between 0.3 and 6.0 μg/L. This leads to a great interest in the speciation and determination of chromium in biological and environmental samples. Spectrophotometry is often favored for detection of Cr(VI) species due to its simplicity and high selectivity, but the applicability of this technique is limited due to its relatively low sensitivity. Cr(VI) reacts with diphenylcarbazide (DPC) to form reddish violet complex Cr-DPC. The formation of the complex is completed within 20 min. TLS has proven to provide better sensitivity and in principle lower LODs compared to spectrophotometry and enables detection of absorbance as low as 10^{-7} using the Cr-DPC complex as the analyte [170]. Because the complex is photolabile, to avoid decomposition of Cr-DPC induced by an intensive excitation laser (such as ~100 mW at 514.5 nm for an Argon ion laser), on-line generation of Cr(VI)-DPC complexes in FIA mode was exploited for

detection in a conventional TLS. A LOD of 0.067 µg/L was achieved. It also indicated that in the case of Cr(VI) determination by on-line generation of Cr(VI)-DPC complexes the time of analysis and the consumption of reagent were significantly reduced.

To miniaturize the analytical instrument used in FIA-TLS, a microfluidic-FIA-TLM setup was constructed to realize online detection of Cr(VI)-DPC complex. In the following, we can see that not only the analysis time was reduced, but also much smaller sample/reagent were needed, and the long reaction coil in conventional TLS setup was also replaced by a simple 15 cm extension loop with ID 200 µm.

4.2.4.1 Microfluidic-FIA-TLM system

The TL signal is determined by the concentration of the product at the detection point. In the microfluidic-FIA-TLM system, the FIA-TLS peak is correlated with the product distribution along the microchannel, which is determined by (1) chemical/physical properties of the sample and reagent, such as reaction rate, volume ratio and respective concentration, and (2) the reaction environment, such as the size of reaction space, reacting in batch mode or flowing mode, reacting by diffusion or mixing, driving mode of the fluid (by electroosmosis, mechanical force, air pressure or gravity). Therefore, at given reagent concentration, influences of the injected sample volume, reaction time, flow velocity and sample concentration on the TL signal of Cr(VI)-DPC in a gravity-driven microfluidic-FIA-TLM system were investigated.

Here, for better understanding of the impact of the driving mode of the fluid on the reaction between sample and reagent, a qualitative analysis of the reaction under different driving force is presented:

(1) If the flow is driven by a microsyringe pump, an interface will form between the carrier and the injected sample, such as in Fig. 49. The reaction is mainly due to diffusion at the interface. In this case, the concentration of formed complex will be low if we detect at the right hand side of the straight channel of the Y junction. To obtain a higher TL signal, a reaction loop would be needed, which connects the Y junction and a second straight channel on the microchip, such as shown in Fig. 51.

Figure 49: Flow characteristic of parallel flow in microchannel (taken from microchip specification) for 0.5 µL/min.

(2) If a gravity-driven pump is used, due to its susceptibility to external pressure change, the sample-reagent mixing is different. At the junction, if the pressure (viscous resistance ± fluid pressure, "+" when the liquid interface is above the junction and "–" when it is below the junction) before the junction of the system is smaller than that after the junction, a large portion of the sample will go to the carrier channel and further to the carrier tubing, as shown in Fig. 50. This was observed in experiments. In this case, the mixing between the reagent and sample is better than in the former case.
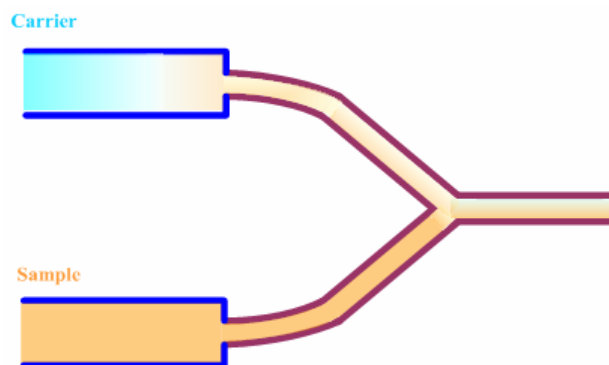
Figure 50: Schematic diagram of sample distribution in a gravity-driven microfluidic system when inject sample manually.

To realize detection of Cr(VI) on a microchip, as shown in Fig. 51, "Connection II", which has already been defined in the "**Gravity-driven pump**" in section 3.1, was employed. One straight channel and the Y-junction channel was connected by a tubing (length 15 cm and ID 200 μm). This tubing is used to transfer the reaction product to the detection point and can also act as a buffer loop to allow certain time for the reaction between the sample and reagent. The length and diameter of the tubing can be chosen as a compromise between the reaction time, analysis time and flow velocity. To reduce dead volume at the interface, the diameter of the tubing is better to be similar or comparable to the size of the microchannel.
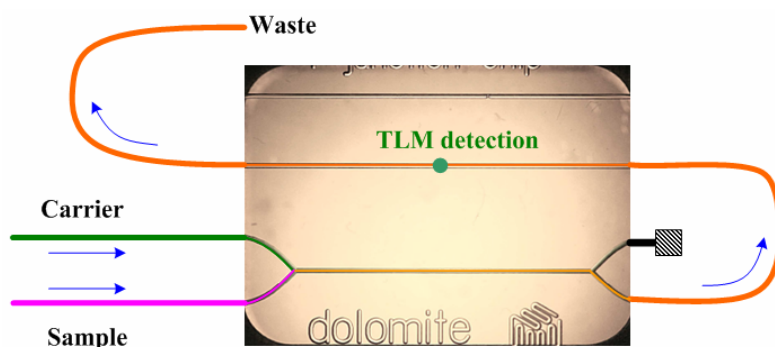
Figure 51: Connection of the microchip and tubings for realization of microfluidic-FIA-TLM detection, where the green spot denotes the TLM detection site.

Due to the extension of the channel length by adding one straight channel and one extension loop in comparison with the previous Connection I, the flow velocity is greatly reduced for the same ΔH, such as for v_x=2 cm/s, ΔH=47.5 cm is needed in Connection II while ΔH=13.5 cm for Connection I. Flow rates of $10-37$ μL/min [corresponding flow velocities of $1-4$ cm/s in the microchannel (205 μm width × 100 μm depth)] are obtained at different ΔHs from $25-67$ cm.

4.2.4.2 Influence of the liquid flow on the TL signal

To check the noise caused by the liquid flow in Connection II, the TL signal of deionized water at both static and flowing modes under the same excitation power was investigated, as shown in Fig. 52. The S.D. of TL signal is similar to that in Connection I for the static and for the flowing mode.

72
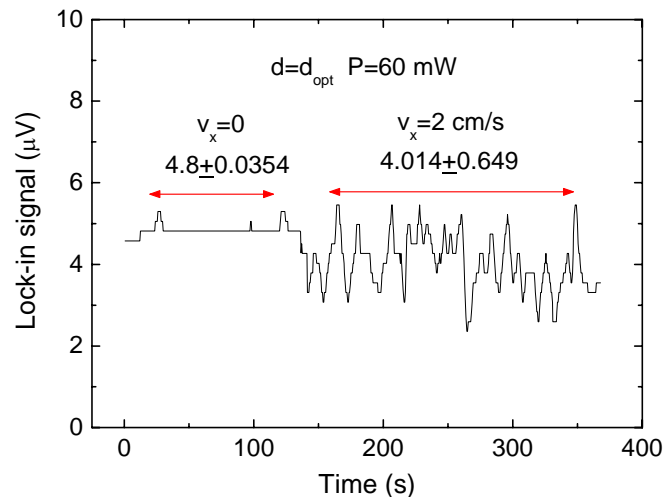
Figure 52: TL signal for deionized water at v_x= 0 and 2 cm/s.

4.2.4.3 Procedure of microfluidic-FIA-TLM detection

In the previous detection of Cr(VI) by conventional FIA-TLS setup [170], some additional measures were needed to obtain a satisfactory FIA-TLS signal: (1) A reversed FIA (rFIA) was employed. The rFIA consists of injecting a certain volume of reagent into the flowing sample stream. By the reversed roles of sample and reagent, the sensitivity increased approximately 3 times relative to conventional FIA, at the cost of much larger consumption of sample and complicated handling in case of multi-sample analysis. The sensitivity enhancement comes from the more efficient mixing between the sample and reagent. In the conventional FIA-TLS setup, an injection loop is used to load the sample (or the reagent in rFIA). The longer the injection loop, the worse the mixing between the sample and reagent will be. In FIA, an injection loop of ~200 μL is needed while in rFIA, a loop of only 20 μL is enough. (2) Also due to the use of the injection loop, 8% acetone and 4% H_3PO_4 were added to the flowing sample (carrier solution) to match the physical properties of the injected reagent, otherwise the nonhomogeneous solvent composition would distort the FIA-TLS signal peak. In the microfluidic-FIA-TLM setup, both additional measures were eliminated due to the much better mixing between the sample and reagent in the microchannel with large specific interface area (Fig. 9).

For best performance, the experiments were performed according to the following procedure:

(1) Clean the tubings and microchip by flushing with water first and then with water/acetone (50:50) mixture and then with deionized water, after which the liquid is forced out of the system with air. Because the flow in the channel is too slow for cleaning under the gravity-driven pump, a pipette or a syringe with plunger can be used to make the flow much faster, which not only saves time for cleaning but also increases the cleaning efficiency.

(2) Tightly connect the sample tubing with the sample syringe. Inject 1 mL of 100 μM ferroin solution into the carrier syringe; make it go through the system and to the waste syringe. Put the two syringes on the optical table. They are at the same horizontal level so there is no flow in the channel. Under certain pump laser power (such as 36 mW), adjust the alignment of the two lasers and the height of the microchip to get the maximum TL signal. Then heighten the carrier syringe by ΔH onto the elevator plane, and adjust mirror M3 to change d to d_{opt} at this flow velocity.

(3) Repeat step 1 to clean the microchannel. Disconnect the sample syringe and the tubing, introduce the carrier into the carrier syringe, enhance the height of the carrier syringe, then the

carrier solution will go through the tubings and microchip. When the carrier flows out from the end of the sample tubing, fill the sample syringe and connect it to the end of the sample tubing tightly. Be careful not to introduce air into the tubing. Avoiding bubbles is very important for gravity-driven pump system because even a small bubble in the channel will greatly change the flow of the liquid and then make the FIA fail. The volume of the sample tubing is about 50 μL. Inject 2 syringes of sample (ca. 200 μL, much larger than the tubing volume 50 μL) into the sample tubing to fill the tubing with sample and to assure that the sample is not diluted by the previous solution in the tubing.

(4) Put the carrier syringe to the former height ΔH in step (2). Make the carrier run to take the redundant sample to the waste syringe, and then record the baseline for a certain time. Then inject a certain amount of the sample, and record the FIA-TLM signal. Repeat injection a few times (usually 2-3 times) for the same sample concentration. Keep in mind that the carrier syringe should be filled in time to assure the measurements runs continuously.

(5) Repeat step 4 with other concentrations and also the blank, then a calibration to the experimental data can be made, and then the LOD and other characteristics can be analyzed.

When a high power is used, avoiding long-term irradiation on an analyte (especially with a high concentration) in static mode is quite necessary to avoid the burnt analyte sticking onto the inner wall of the microchannel, which will contaminate the microchannel and make the temporal TL signal unstable.

4.2.4.4 Influence of the injection volume of the sample on the TL signal

The FIA-TLM signals of the Cr(VI)-DPC for different injection volumes were measured. As shown in Fig. 53, when the sample volume increases higher than 6 μL, such as 8 μL, the TL signal is distorted (as shown in the circled area) due to the insufficient reaction between Cr(VI) and DPC in the central part of the injected sample, which is more evident for the 10 μL sample injection. To make a compromise between the TL signal and sample consumption, 4 μL was used as the injection volume, which is ∼100 times smaller than that used in conventional FIA-TLS setup.
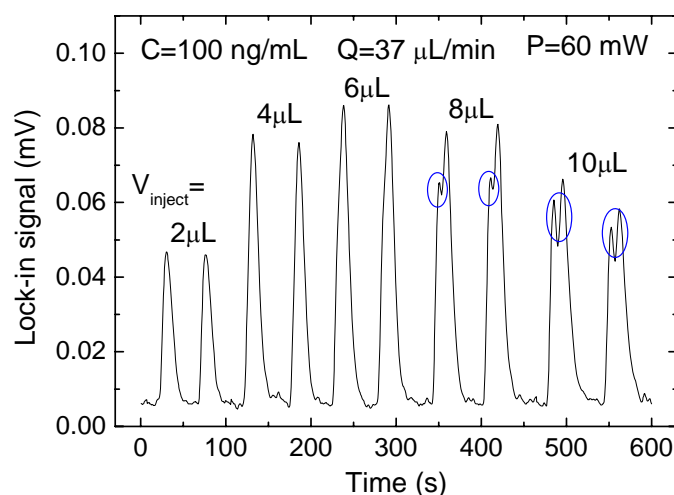
Figure 53: Influence of different injection volumes on FIA-TLM signal for the sample concentration of 100 ng/mL, at excitation power 60 mW and flow rate 37 μL/min.

4.2.4.5 Influence of the flow rate on the TL signal

To investigate the reaction rate between the Cr(VI) and DPC, TL signals at different flow rates were recorded, as drawn in Fig. 54. Considering the impact of the sample flow on the TL

signal amplitude (section 4.2.3.4), we can see that there is little difference between the TL signals at different flow rates. Due to the largely reduced diffusion time in the microchannel, the reaction is done within 10 s, and the analysis time for one injection is around 50 s at flow rate 37 μL/min.
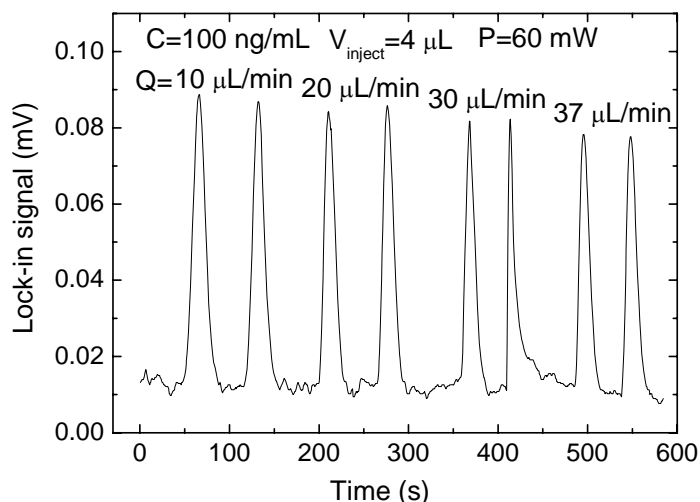
Figure 54: Influence of different flow rates on FIA-TLM signal for the sample concentration of 100 ng/mL, at excitation power 60 mW.

4.2.4.6 Influence of the excitation power on the TL signal

TL signals at different excitation powers are given in Fig. 55. From the figure we can see that with the increase of the laser power, the TL signal reached saturation due to photodegradation of the Cr(VI)-DPC complex by intensive laser excitation. The photodegradation was confirmed by the fact that at high pump power, there is not much signal enhancement observed when the sample is pumped through the illuminated area of the pump beam in comparison with the sample in static mode. The lower the pump power, the higher the signal enhancement will be. In this experiment, 60 mW was chosen as the excitation power.
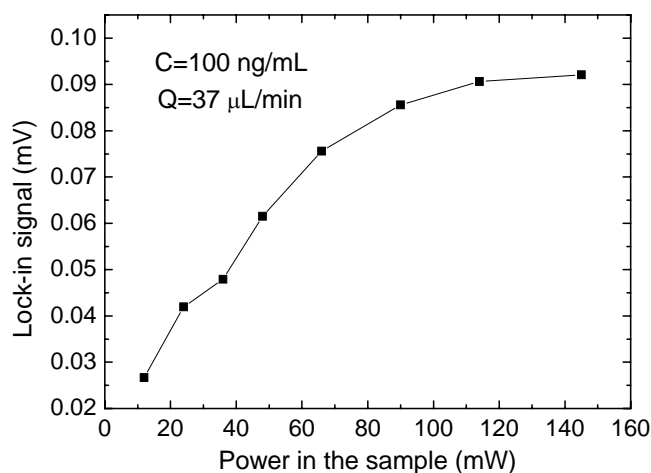
Figure 55: Influence of excitation power on FIA-TLM signal for the sample concentration of 100 ng/mL, at flow rate 37 μL/min.

4.2.4.7 LOD of detecting Cr(VI) in the microchip

In Fig. 56(a), TL signals for three concentrations of Cr(VI) were recorded, and for every concentration two injections were made. The good reproducibility of the TL signal at one

concentration demonstrates that the FIA can be realized on a microchip even with a manual injection syringe. In Fig. 56(b), a calibration curve is given for Cr(VI). Standard deviation of the TL signals of the blank is around 0.8 μV. Therefore, at the power of 60 mW, we get a LOD of 3.5 ng/mL for Cr(VI), corresponding to an absorbance of 1.85×10^{-5} AU for Cr(VI)-DPC at 514.5 nm. By comparison with the absorbance LOD in section 4.2.3.7, we can find that the LOD obtained here is over 2 times higher even if a three times higher pump power is used. This means that at power 60 mW, Cr(VI)-DPC has already degraded to some extent.
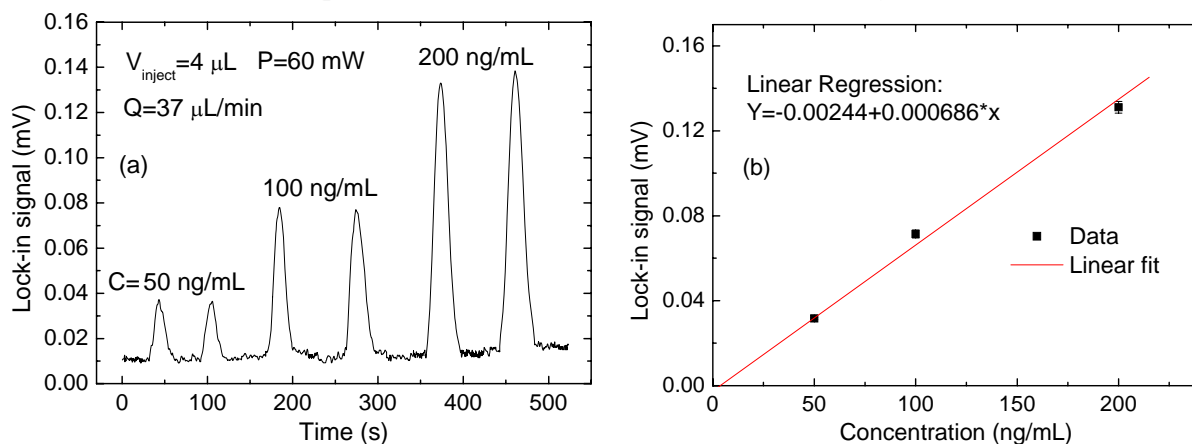
Figure 56: (a) FIA-TLM signal of the Cr(VI)-DPC complex for three Cr(VI) concentrations, and (b) a calibration curve for FIA-TLM determination of Cr(VI).

From the above discussion, we can conclude that the detection of Cr(VI) in a homemade microfluidic-FIA-TLM setup was successively realized. Though the concentration detection limit is not so impressive, the amount of Cr(VI) which can be detected in a confocal TL volume of 300 fL is only 20 zeptomole. By performing a similar experiment at the pump beam radius of ~ 0.7 μm and power 8 mW, a LOD of 22.5 ng/mL was obtained with a TL confocal volume of 5 fL. Then, the quantity of detected molecule is about 2 zeptomole. This demonstrates that this microfluidic-FIA-TLM setup is particularly suited for small volume samples and can be performed for online detection of analyte in a short time.

4.3   An ILS-excited TLM

In the previous section, a laser-excited TLM was built for detection in a sample cell or in a microfluidic chip to realize batch-mode or FIA measurements. However, when highly focused by an OL, cw or pulsed lasers with high power/energy may cause many unexpected consequences especially for biological or bioanalytical assays, such as convective noise, nonlinear absorption effects, optical saturation or bleaching and photodegradation [171]. These side effects would compromise the sensitivity brought by the high power of lasers. Another severe drawback is the limited number of laser emission lines available for excitation, which is the key factor restricting the TLS/TLM to become a method for routine chemical analysis. Therefore, it is important to develop TLS instruments based on lower-power broad-band light sources and to investigate the related TL signal. As already reviewed in the chapter on theoretical background, the LOD of ILS-excited TLS is relatively low especially when the sample is in aqueous solution and the sample length is short (such as 100 μm). Therefore, it is much desired to improve the sensitivity of the ILS-based TLS. From the definition of the enhancement factor, we can see that the most commonly used approach is to increase the power or to improve the thermal properties of the sample. But the possible power enhancement of the ILS is very much limited. For example a maximum power of ~10 mW for a 10-nm bandwidth could be obtained after a grating for a xenon lamp between 250 to 1100

nm (Tunable Illuminator, OBB Corp.). On the other hand, the thermal properties of aqueous sample solution can only be improved to some degree, governed by the achievable mixing ratios and corresponding dilution factors. Therefore, it seems very difficult to improve the sensitivity just from the viewpoint of the enhancement factor.

In this section, the TL signal was studied under an ILS-excited TLM both theoretically and experimentally. An optimized optical configuration was found, and more importantly, a three-layer sample system was introduced to enhance the sensitivity.

4.3.1 Numerical simulations

Some parameters used in the numerical simulations are assumed as follows: power of the excitation light is 10 mW; absorption coefficient of the analyte is 25.32 m^{-1}. Convective heat transfer coefficients on both boundaries are 8 W/m^{2}K. Thermophysical parameters of materials used in this section were given in Table 3.

4.3.1.1 Temperature distributions under excitation of a divergent ILS

To determine the effective excitation length of the ILS for TL generation, numerical simulations were performed for a sample much longer than usually used in TLM. Figure 57 gives the temperature profiles under ILS excitation in a 5-mm cell, at modulation frequencies of 100 and 10 Hz. The excitation beam radius profile was already presented in Fig. 30. When a 100-μm excitation beam excites the sample at a frequency such as 100 Hz, the induced temperature maintains not only the top hat profile of the light intensity but also the divergence of the excitation beam along z-axis. When the frequency goes down to 10 Hz, the temperature doesn't show a "top-hat" profile anymore because of much larger thermal diffusion compared to that at 100 Hz. In later experiments, the effective length of the ILS or the effective temperature region contributing to the TL signal will be determined
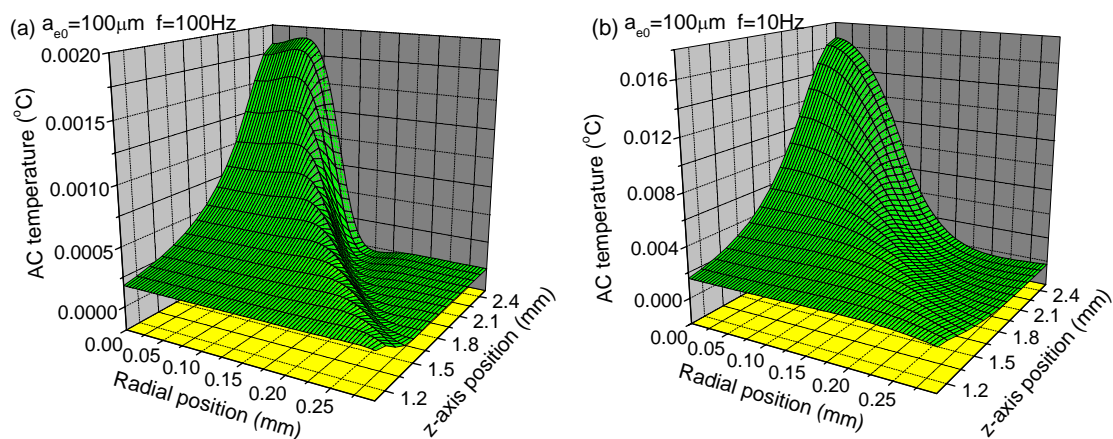
Figure 57: **Temperature profiles in a sample with 5 mm sample length under excitations of top-hat beams of 0.1 mm, at (a) 100 Hz and (b) 10 Hz.**

4.3.1.2 Temperature distributions and TL signal in a three-layer sample system

In this section, impacts of top- and bottom-layer with different thermophysical properties on the TL signal are simulated. To make a comparison, both 1-μm scale (laser excitation case) and 100-μm scale (ILS excitation case) excitations are considered. Regarding the sample layer, besides an aqueous sample, a sample in organic solution (methanol) is also considered. Top- and bottom-layer of different materials, including fused silica, polystyrene and n-octane, were used for calculation.

Temperature distributions in the axial and radial directions are shown in Fig. 58. "Adiabatic" in the figure means that there is no heat entering into the top/bottom layers.
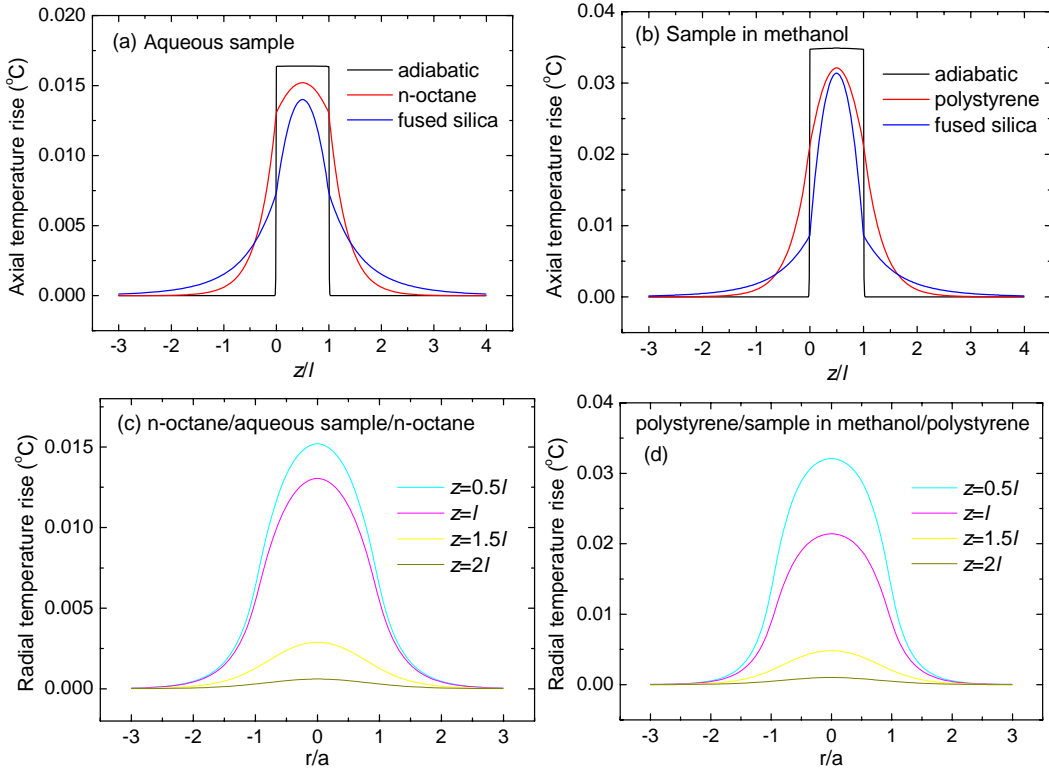
Figure 58: Axial (z-direction) temperature distributions of 3-layer systems with the central layer of (a) aqueous sample and (b) sample in methanol, and radial temperature distributions of (c) n-octane/aqueous sample/n-octane and (d) polystyrene/sample in methanol/polystyrene systems, under the top-hat beam excitation. Both l and a_e are 100 μm and the modulation frequency is 20 Hz.

From this figure we can see:

(1) Under the same pump parameters, portion of heat entering into the surrounding layers is larger when the central layer is aqueous sample solution than when it is in methanol due to higher thermal conductivity of water.

(2) When the material surrounding the sample is n-octane, the temperature rise in the sample and around the interfaces is larger than that for the case of fused silica, and the heat in a modulation cycle can conduct as far as 200 μm when the modulation frequency is 20 Hz. A lower frequency can further increase this region. By further considering favorable thermal properties (higher $\partial n/\partial T$ and lower k) of n-octane, it can be anticipated that the TL signal for n-octane as the top/bottom layers should be greater than that when the sample is contained in a fused silica cell. This prompts us to compare the TL signals with different materials used as the top/bottom layers. Because the $\partial n/\partial T$ of n-octane is negative, the TL elements formed in the three-layer system would be like those shown in Fig. 59.
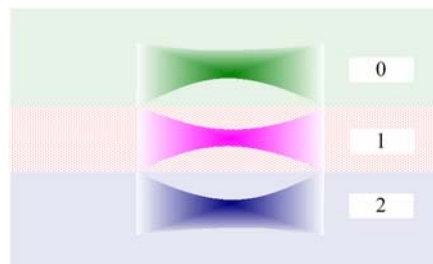
Figure 59: TL effect of a three-layer system if $\partial n/\partial T$s of all three layers are negative.

Because the excitation beam radius in the sample under an ILS-excited TLM is much larger than that in a laser-excited TLM, the detection scheme should be carefully optimized to achieve maximum sensitivity. Here, variations of the TL signal under different (w_1, z_1)s are given. Figure 60(a) shows the TL signals as a function of z_1 (distance from the probe beam waist to the sample, $z_1<0$ means the waist is behind the sample) for several beam waist radii (w_1). From the figure we can see that smaller w_1 corresponds to higher TL signal at an appropriate z_1. The TL signals at $w_1=30$ μm are quite close to those at $w_1=20$ μm, so it is not necessary to decrease w_1 to less than 20 μm. And also, it is very difficult to realize large $|z_1|$ at very small w_1 under a high NA OL, which requires the beam waist radius (w_0) before the OL to be very small. Experimentally, probe beam parameters of $(w_1=20\sim30$ μm, $z_1=-5\sim-7$ cm) will be used as the detection scheme. In the next simulation part, a probe scheme of $(w_1=25$ μm, $z_1=-6$ cm, $z_2=50$ cm) is used for ILS-induced TL signal calculation.
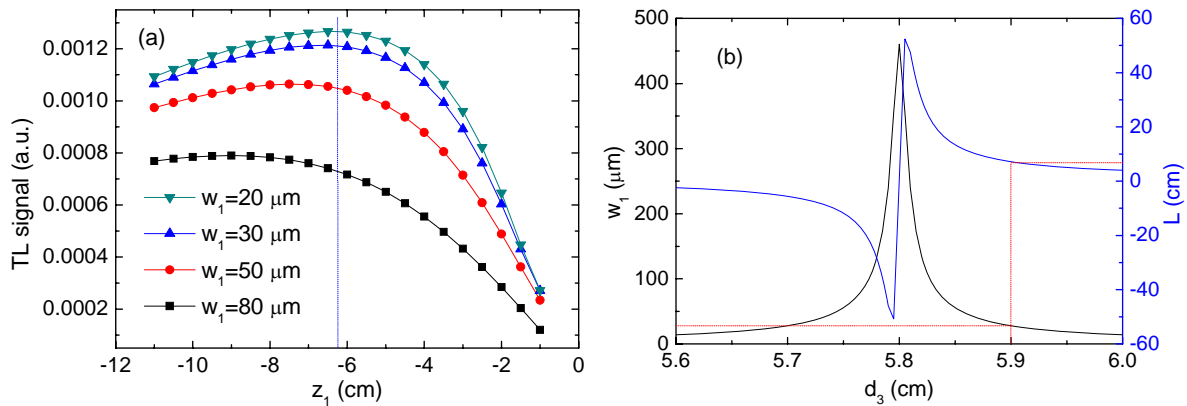
Figure 60: (a) TL signal as a function of probe beam parameter (w_1, z_1) in ILS-excited TLM. The top- and bottom-layer are fused silica, and the sample length is 100 μm. (b) Probe beam parameters after a 20×/NA 0.40 OL with the change of d_3, where d_0=0.05 m, f_1=0.03 m, d_1=0.23 m, f_2=0.2 m, d_2=0.25 m, f_3=0.05 m (see section 4.1.1.1 for the definitions of d_0, f_1, d_1, f_2, d_2, f_3, d_3 and L).

To obtain such probe beam parameters of $(w_1=25$ μm, $z_1=-6$ cm), in beam expander IV (Fig. 11), focal lengths of the three lenses L10, L11 and L12 were carefully selected as 3, 20 and 5 cm, respectively. As shown in Fig. 60(b), the two parameters of w_1 and z_1 of the probe beam can not be changed independently in coaxial TLM.

Figure 61 presents the frequency-dependent TL signals for a sample in methanol or in water with different materials as the top/bottom layers. For comparison, both the TL signals in a laser-excited TLM at a_e=3 μm and in an ILS-excited TLM at a_e=100 μm were calculated. It should be noted that the detection scheme for the laser-excited TLM is taken as $(w_1=2$ μm, $z_1=-15z_R$, $z_2=2$ cm).

From Figs. 61(a) and 61(b) we can see that due to the small pump beam radius compared to the sample length (l=100 μm) in the laser-excited TLM, the surroundings (top/bottom layers) can only slightly influence the TL signal. Even for the sample in water at 5 Hz, the TL signal with octane as the top/bottom layers is only 1.4 times higher than that with fused silica as the top/bottom layers. For ILS-excited TLM, when polystyrene is used as the top-/bottom-layer material, it can bring a signal enhancement of about 2 times higher for sample in methanol and 4 times higher for sample in water comparing to the fused silica case at 5 Hz. If octane is used as the top/bottom layers for the sample in water, the signal enhancement at 5 Hz is about 10 times higher comparing to the fused silica case. An interesting result is that in the low-frequency region (<10 Hz), for the sample in water with octane as the top/bottom layers, the TL signal at a_e=100 μm is even larger than that at a_e=3 μm. This means that for an aqueous sample solution, the sensitivity of an ILS-excited TLM could be higher than that in a laser-

excited TLM. Therefore, in experiment, a 3-layer system can be proposed to enhance the sensitivity of an ILS-excited TLM.
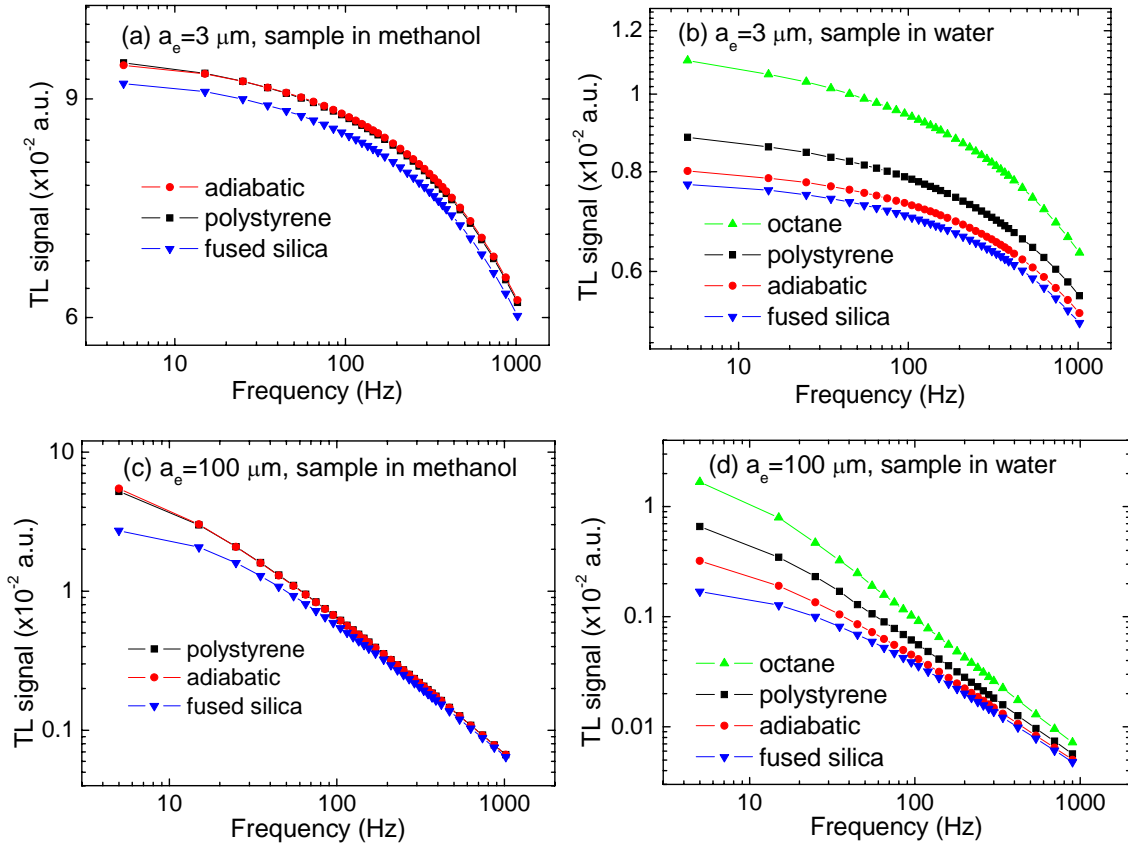
Figure 61: Frequency-dependent TL signals for 3-layer systems at a_e=3 µm when sample is (a) in methanol or (b) in water, and at a_e=100 µm when sample is (c) in methanol or (d) in water, with l=100 µm.

If organic solvents with better thermal properties such as CS_2 are used as the top/bottom layers, the signal enhancement can reach 15 times for a_e=100 µm and f=5 Hz, as shown in Fig. 62, where the signal enhancements induced by different organic solvents are given.
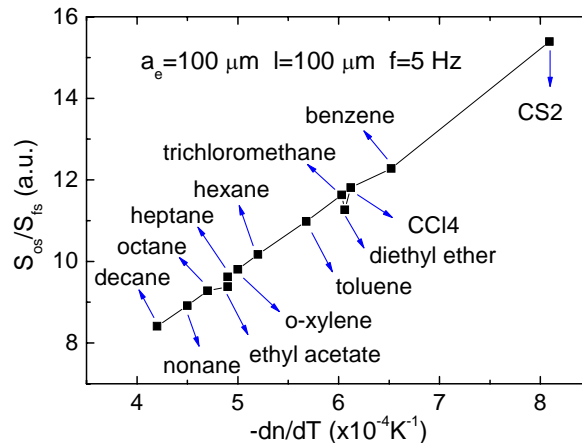
Figure 62: TL signal enhancement caused by top/bottom layers of different organic solvents (os) in comparison with top/bottom layers of fused silica (fs).

Another parameter influencing the signal enhancement is the sample length. In Fig. 63, it is revealed that the thinner the sample is, the larger signal enhancement can be achieved. When the sample is ~50 µm, 30 times signal enhancement is expected. This is especially

advantageous for the micro-volume sample analysis. However, when the sample is thicker than 1 mm, the top/bottom layers will contribute little to the TL signal improvement.
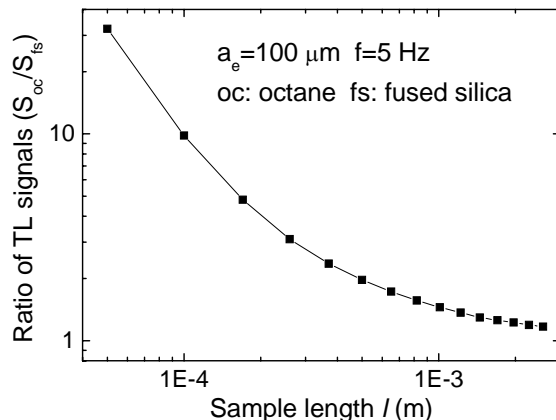
Figure 63: Ratio of TL signals for an aqueous sample based system with octane as top/bottom layers with respect to a system with fused silica as top/bottom layers, at different sample lengths.

4.3.1.3 Temperature distributions and TL signal considering the effect of sidewall

Effects of several sidewall materials with different thermal conductivities on the temperature distributions and TL signals are discussed in this section. Dimensions of the well-type cell of (a=150 μm, b=5 mm) shown in Fig. 29(d) are used in numerical simulations discussed below. To better show the influence of the sidewalls on a top-hat beam-induced temperature, the excitation beam radius is assumed to be the same size as the well radius, i.e. a_e=150 μm. In TLS, a probe beam with Gaussian intensity distribution in the detection plane is preferable to assure a linear response of TLS to analytes with different concentrations. From Fig. 64, we can see that strong interference with the probe beam intensity in the detection plane is introduced by the sample cell sidewall when the sample cell radius (r_s) is smaller than the probe beam radius in the sample plane (w_s). When r_s>2w_s, a Gaussian intensity distribution in the detection plane is kept. Therefore, to avoid the interference and its further influence on the TL signal, it is better to choose an appropriate sample cell or change the probe beam parameter so that a preferable condition of r_s/w_s >2 can be met. To avoid the interference from the sidewalls of the sample cell with radius 150 μm, the probe parameters of (w_1=25 μm, z_1=-0.9 cm, z_2=10 cm) were used.
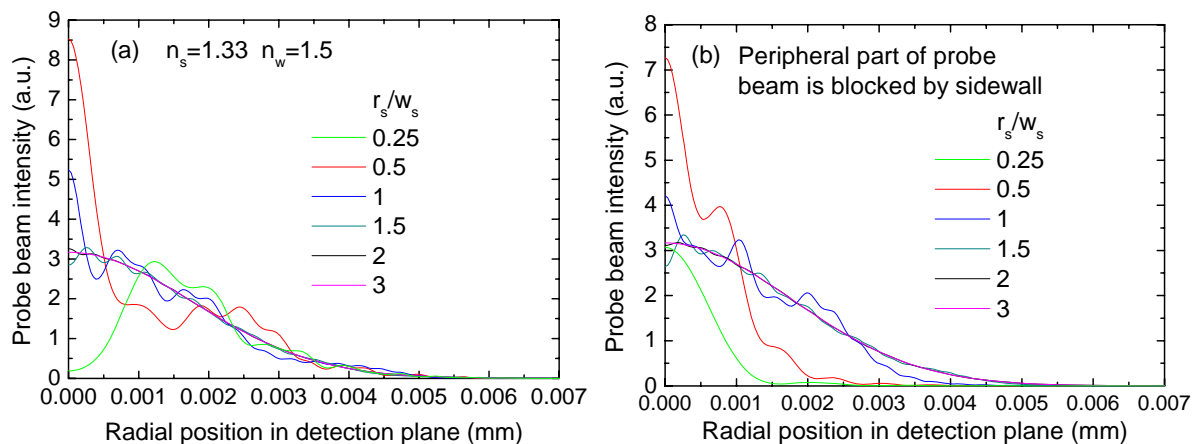
Figure 64: Probe beam intensity in the detection plane (a) when the sidewall (with refractive index n_w=1.5) is transparent to the probe beam, or (b) when it is opaque to the probe beam, with probe beam parameters of (w_1=25 μm, z_1=-6 cm, z_2=50 cm). n_s: refractive index of the sample, r_s: radius of the sample cell, w_s: probe beam radius in the sample plane.

From Fig. 65(a) we can see that the temperature distributions are different due to the difference in thermal properties of the sidewall materials. For the polystyrene sidewall, the effect of the wall on the thermal conduction of the heat out of the excited sample is the smallest, and the temperature profile looks like a top hat. For stainless steel wall, the temperature is more parabolic due to its high thermal conduction. But for the fused silica wall, the temperature inside the cell is similar to that of the sample system (without sidewall) but different outside the cell.

In Fig. 65(b), impact of the modulation frequency on the temperature distributions of sample-stainless steel system is shown. With the increase of modulation frequency, the temperature profile changes rapidly from a parabolic curve to a top-hat one.
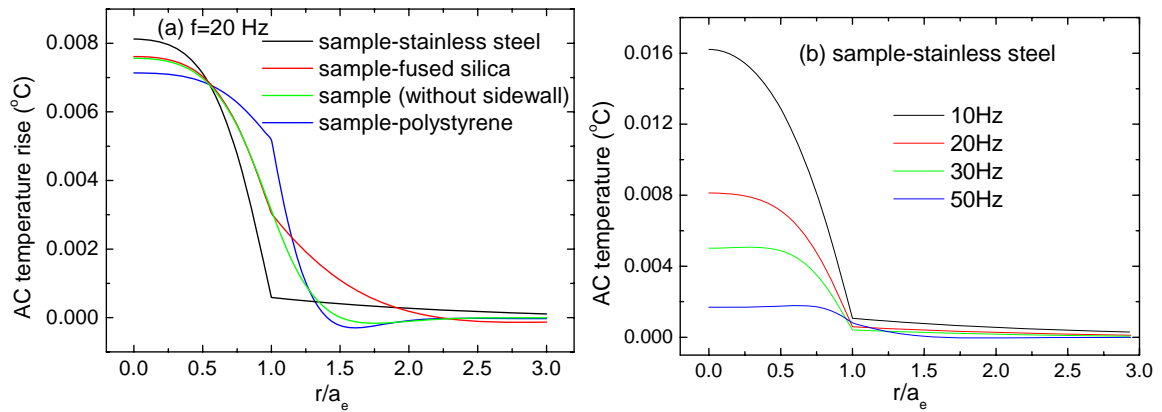
Figure 65: (a) Temperature distributions in a well-type sample cell at f=20 Hz, with different materials as sidewall, and (b) temperature profiles of water-stainless steel system, at different frequencies.

In Fig. 66, numerical simulations for influences of the sidewalls on the TL signal are displayed. The TL signal of the sample-fused silica system is similar to that of the sample system (without sidewall), which can be anticipated from their temperature distributions. At From 5 to 50 Hz, the TL signal decreases by two orders of magnitude. This large difference results not only from the quite different temperature profiles as shown in Fig. 65(b), but also from the probe beam parameters assumed above, at which the probe beam is diffracted to a less extent by a top-hat-like profile. The TL signals of the sample-polystyrene and sample-stainless steel systems are 2.4 times lower and 1.5 times higher, respectively, with respect to that of the sample-fused silica system. It should be noted that the above conclusions are only valid when the thermal diffusion along z-axis is negligible, otherwise the influence from the top/bottom layers should be considered.
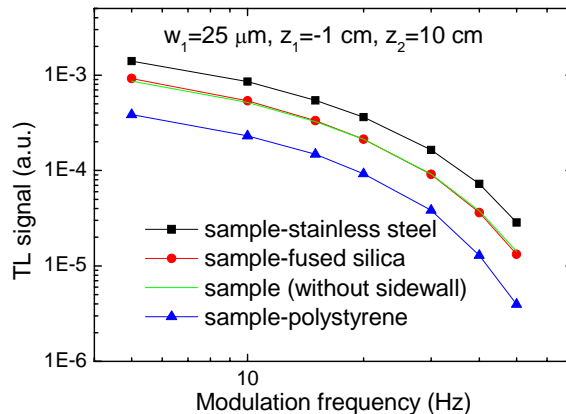
Figure 66: TL signal as a function of frequency for different sample-sidewall combinations.

82

The TL signal in the ILS-excited TLM is experimentally discussed. Corresponding optimization is made and sensitivity enhancement brought by the top/bottom layers as indicated in the theoretical part is verified. The alignment of the system is quite similar to that in laser-excited TLM. Relative power spectrum of the ILS and its equivalent excitation power (1.05 mW) at 514.5 nm for ferroin solution were already given in the "**Power meter**" in section 3.1. Thermal time constant of the TL element in aqueous solution is 0.02 s at a_e=107 μm. Some experimental parameters, unless otherwise stated, are as follows: the sample is 1 mM ferroin, the detection distance is 50 cm, the probe beam radius in the detection plane is about 2 cm and the signal from the photodiode before excitation (S_{dc}) is 1 V.

4.3.2 TLS experiments in a sample cell

In the first step, experiments in a 100-μm sample cell were performed, in which impacts of the noise source, detection scheme and sample length on the TLS signal are investigated.

4.3.2.1 Sources of noise

Due to low power of the incoherent light source, the ILS-excited TLM usually works at low modulation frequency (such as 5～10 Hz) to obtain an acceptable sensitivity. The main drawback when working at low frequencies is the relatively large noise on the TL signal, which severely limits the LOD of the instrument. Diverse noise sources (electronic noise of the detector, power or beam fluctuations of the light sources, convective or flow noises in the sample) would influence the signal to different extents. The influence of the power fluctuation can be compensated by on-line recording of the power change and accounting for it in TL signal. An optical isolator composed of a linear polariser and a λ/4 waveplate at 632.8 nm is used to stop the reflected probe beam back into the laser cavity. For the convective or migration noise in the sample, it is better to start measurement when the sample reaches equilibrium after sample preparation [Fig. 67(a)], since there may be turbulence inside the sample due to insufficient contact time between the sample and the sample cell. This strongly affected the TL signal as shown by the dark curve. When the sample reached stabilization, the signal was steady, as indicated by the red curve. In addition, noises from the environment should be considered. All the electrical instruments are better to be connected to a regulated power supply. The reference signal cable is away from the TL signal cable to avoid coupling the modulation signal from the chopper to the TL signal. Besides, walking of personnel or air conditioning should be avoided. As shown in Fig. 67(b), the probe beam noise when air conditioning is on is about 10 times higher than that without air conditioning. In Fig. 67(c), probe beam noise and signal-to-noise ratio (S/N) as a function of $d_{ph}/(2w_2)$ are given. When comparing the changes of the noise and the S/N at different $d_{ph}/(2w_2)$s with those given in Fig. 2 in Ref. 109, we can see that at low modulation frequencies (5 Hz), the noise is dominated by flicker noise. At very small $d_{ph}/(2w_2)$, the S/N drops, such as indicated by the two initial measurement points on the left. This is because at very small $d_{ph}/(2w_2)$ values, the shot noise and/or background noise of the detector [Fig. 21(e)] have a bigger effect on the S/N over the flicker noise. The maximum signal-to-noise ratio occurs at $d_{ph}/(2w_2)$ of 0.05. Therefore, for the probe beam size of 2 cm in the detection plane, a pinhole of 1 mm can be selected for the best signal-to-noise ratio.
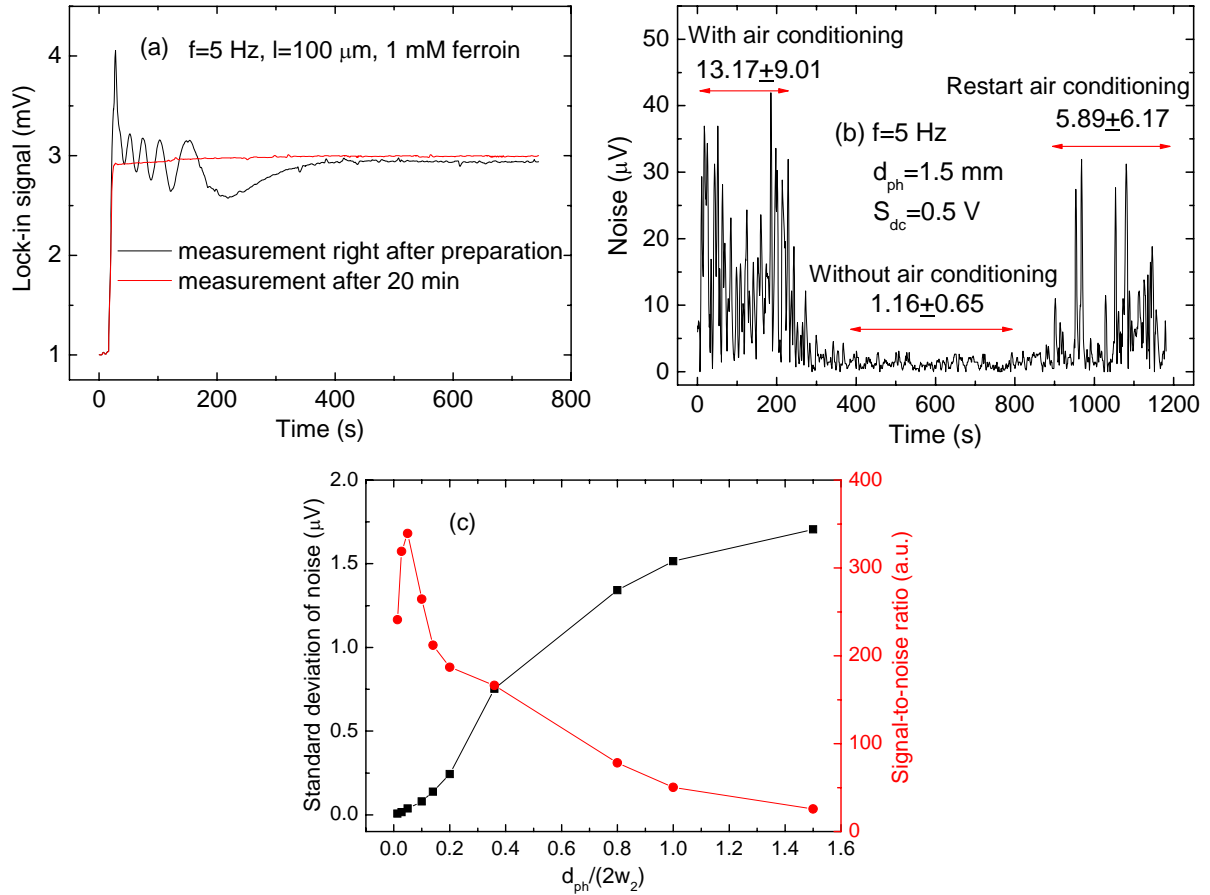
Figure 67: (a) Time-dependent lock-in signals of the sample measured right after the preparation in the sample cell or 20 min later, (b) influence of the air conditioning on the probe beam noise, and (c) probe beam noise level and signal-to-noise ratio as a function of $d_{ph}/(2w_2)$.

4.3.2.2 Influence of probe beam parameters on the TL signal

By adjusting the distance between lenses L10 and L11, the beam waist w_0 after lens L12 can be changed; then shifting L12, the probe beam parameters after the OL at this w_0 can be altered correspondingly.

Figure 68 gives the TL signals at different probe beam parameters. The sample is in a conventional 100 μm quartz sample cell, which is called "one-layer" system. Exactly speaking, this is a three-layer system with quartz plates as top/bottom layers, but to differentiate it from the following two- or three-layer systems with additional signal-enhancement layers, it is called one-layer system. Here, to make a comparison with theory, not the lock-in signal but the TL signal should be calculated, because when the probe beam waist w_1 changes, the DC light intensity S_{dc} is changed correspondingly. According to the definition of the TL signal ($S=S_{ac}/S_{dc}$), the experimental TL signals were calculated like this: S_{ac} is obtained by the lock-in signal multiplied by "3", which is a proportionality constant between the peak-to-peak value of the input AC signal and the displayed amplitude on the lock-in panel; S_{dc} is the output signal of the detector before excitation measured with a multimeter. It is revealed that the experimental data are in good agreement with the theory. Therefore, in next experiments, the detection parameters of (w_1=25 μm, z_1=-5 cm) were used.

84
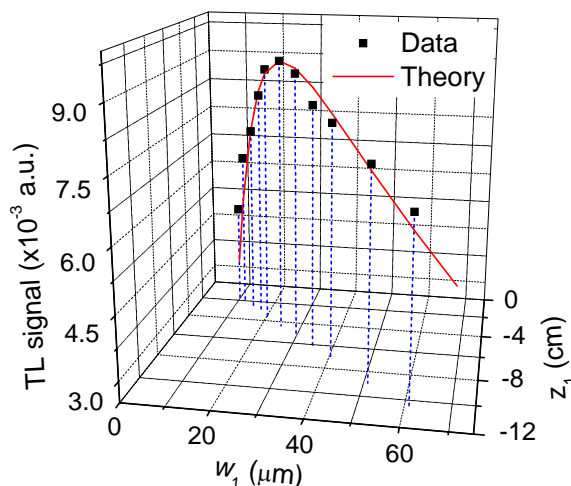
Figure 68: TL signals at different probe parameters (w_1, z_1) after the OL when w_0=3.5 μm. Dark square: experimental data; red curve: theoretical curve.

4.3.2.3 Sample length-dependent TL signal

Figure 69 gives the sample length-dependent TL signals as well as theoretical predictions. It is shown that the experimental data are in good agreement with the theory, and the effective sample length l_{eff} for this ILS light source is about 1.5 mm.
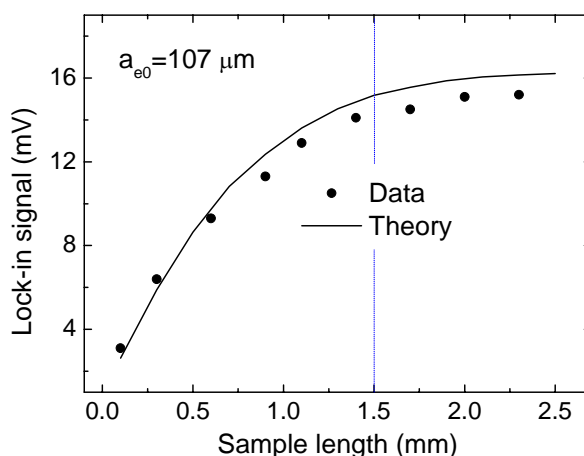
Figure 69: Sample length-dependent TL signals in the ILS-excited TLM.

4.3.3   Sensitivity enhancement in ILS-excited TLM

In Section 4.3.2, the probe beam parameters were optimized and the effective sample length for the used xenon lamp was obtained. However, the sensitivity of this one-layer system is not enough for practical applications (its LOD will be given later). According to theoretical prediction in section 4.3.1.2, a three-layer sample system with high $\partial n/\partial T$ and low k top/bottom layers could be a choice to enhance the detection sensitivity. Here, n-octane is used as the material of top/bottom layers.

At first, to check the solubility of ferroin in octane, 1.5 mL 1 mM ferroin solution and 3 mL of octane were injected into a vial [Fig. 70(a)], which was sealed tightly and kept for two days. Then, 2 mL octane was taken out from the vial and put into a 1-cm glass sample cell. Absorption spectra of the octane from the vial was measured by spectrophotometer and compared with the octane from original solvent bottle. As shown in Fig. 70(b), except for some measurement noise, there is no difference for absorption spectra in visible region between the octane in contact with ferroin and the original octane. The measurement noise

may come from the absorption of impurity in the vial and/or the absorption of a very small amount of ferroin in octane below the detection limit of the spectrophotometer. Here, if we assume the absorbance of the ferroin in octane at 514.5 nm is 10^{-3} AU in 1-cm cuvette (corresponding to an absorption coefficient of 0.23 m^{-1}) and the effective sample length is 1.5 mm (Fig. 69), the TL signal can be theoretically calculated as 8.46×10^{-4} at pump power 1 mW and pump beam radius of 100 μm. Under the same pump beam and probe beam parameters, for a three-layer sample system with 100 μm of 0.1 mM ferroin as the sample [the lowest concentration of ferroin used in three-layer systems as shown in Fig. 72(b), with absorbance of 1.0 AU in 1-cm cuvette, corresponding to an absorption coefficient of 253.2 m^{-1}], the TL signal is theoretically calculated as 1.55×10^{-2}. This means that the contribution of the octane-soluble ferroin-induced thermal lens effect to the signal enhancement is only 5.5%. Practically, considering that the pump beam radius in the octane (top/bottom layer) is larger than 100 μm (Fig. 30, page 47) and the real absorbance of octane-soluble ferroin could be less than 10^{-3} AU, less contribution from the octane-soluble ferroin than 5.5% can be expected. Therefore, octane is an appropriate kind of material as the top/bottom layers for sensitivity enhancement.
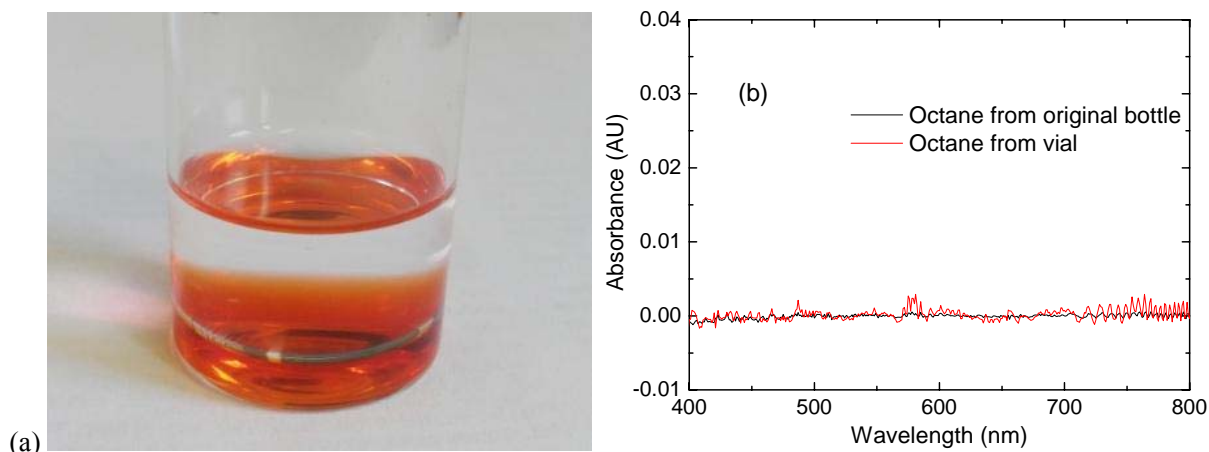
Figure 70: (a) Octane and ferroin in a vial after two days, and (b) absorption spectra of octane from the vial and from the original solvent bottle.

4.3.3.1 Sample length determination in the two- and three-layer sample systems

Due to the change of the sample mount from a standard sample cell to a home-made sample well, some tips should be mentioned before finding the TL signal:

(1) After mounting the sample well on the sample stage, adjust the *z*-axis to approximately put the sample (middle layer) in the beam waist of the excitation beam. This can be judged by the distance between the top surface of the well and the bottom of the OL, which should be about 1 mm for the two-layer sample system or 3 mm for the three-layer sample system;

(2) Then adjust the *x*- and *y*-position of the sample well through the 3-D stage to let the beams go through the center of the well. At this time, the probe beam after the sample may be deflected a little bit with respect to the initial pinhole because of the curved interface of the sample, so it is necessary to adjust the detector stage to make the pinhole back to the center of the probe beam.

(3) Adjust the system finely with a procedure similar to the one used in laser-excited TLM to achieve the maximum TL signal.

At first, the TL signal in a two-layer sample well was checked. The lock-in signal for a certain two-layer system was recorded as a function of time at different frequencies, as displayed in Fig. 71(a). From the figure we can see that the signal is relatively stable. As we know from

the theoretical part that the contribution of the organic layer to the TL signal enhancement is not only dependent on the sample thickness but also on the modulation frequency, we can deduce the thickness of the sample from the frequency-dependent TL signals. Thus, the change of the experimental signals with frequency was fitted to the theory, as in Fig. 71(b), and for the given experimental conditions at l=105 μm, the best fit was reached. This demonstrates that a frequency-dependent TL signal fitting to the theory could be a way to estimate the sample length in the system.

However, curve fitting needs computer-based calculation, which takes time. To realize an instant judgement in experiment, the sample length can also be calculated according to the ratio of the TL signals at two discrepant frequencies (such as 5 and 140 Hz), which is different for different sample lengths, as shown in Fig. 71(c). At l=100 μm, this ratio is sensitive to the change of the sample length especially for the three-layer system. By comparing the experimental signal ratio with the theoretical ratio in this sensitive region, the sample length can be estimated. This method has been verified to be effective on the standard 100 μm sample cell. For the two- and three-layer systems, the theoretical ratios of the TL signals at l=100 μm are 26.4 and 36.0, respectively. In later experiments, only those prepared sample systems with S(5 Hz)/S(140 Hz) of around 26.4±0.8 for two-layer system or 36.0±1.5 for three-layer system, corresponding to sample lengths of 100±25 μm, were chosen for TL measurements related to comparison of calibration lines for one-, two- and three- layer systems. For sample lengths longer than 300 μm, the ratio is not so sensitive to the sample length change. In these cases, we can simply determine the thickness according to the injected sample volume, as presented in Eq. (18)-related context in section 3.1.
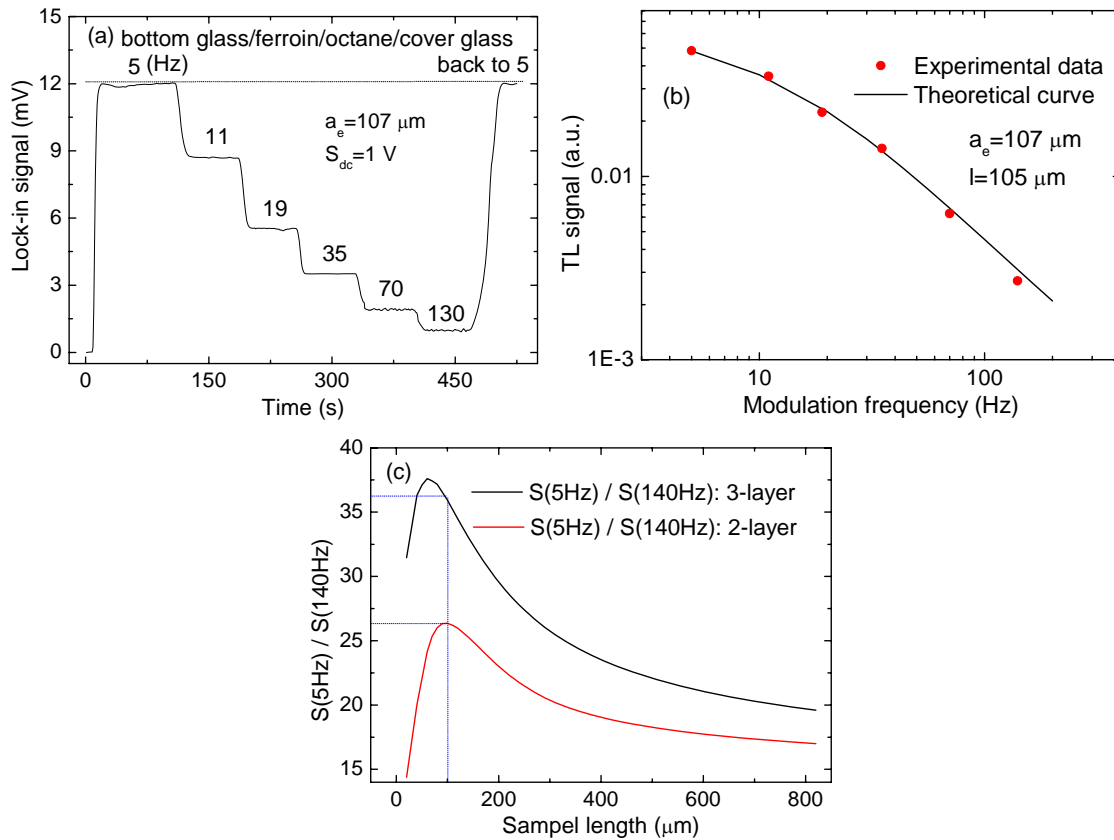
Figure 71: TL signal as a function of modulation frequency: (a) time-dependent lock-in signals at different frequencies and (b) comparison between experimental data and theory. (c) Ratio of signals at 5 and 140 Hz for octane as top or bottom layer for two-layer and three-layer systems, as a function of sample length.

4.3.3.2 Influence of sample length and top/bottom layers on the TL signal

From section 4.3.1.2 we knew that when the sample is in organic solvent or organo-aqueous mixed solvent (such as 80% HPLC grade methanol and 20% deionized water [146]), the signal enhancement brought by the top/bottom layers are not as obvious as for aqueous sample. Hence, in the following experiment, the influence of the top/bottom layers was investigated only on an aqueous sample.

In Fig. 72(a), the sample length-dependent TL signal in a two-layer system, as well as a theoretical curve normalized to the experimental data at l=100 μm, is shown. It is revealed that the signals at large thicknesses depart from the theory. This is because the theoretical curve was calculated according to a model (Section 4.1.3.3) in which the beam divergence of the ILS in the sample is not considered. Actually, the divergence of the excitation beam has a big impact on the TL signal. We can see that the effective sample length (or say the effective pump beam region) contributing to the TL signal is about 1 mm around the center of the focused ILS, which is in agreement with that for the one-layer system given in Fig. 69. It should be noted that if signal enhancement layers are used, the optimal sample length is less than 500 μm to assure that there is enough heat transferred to the top/bottom layers in a modulation cycle to form additional TLs.
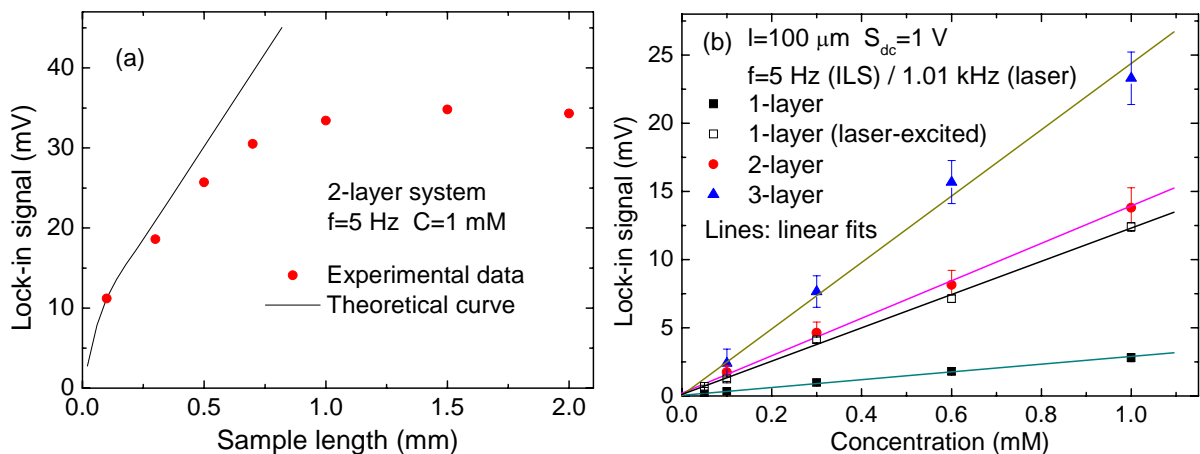
Figure 72: (a) Sample length-dependent TL signals in a two-layer system and (b) comparison of TL signals for one-, two- and three-layer systems.

In addition, the TL signals as a function of sample concentration for the three systems, one-, two- and three-layer systems were compared, as shown in Fig. 72(b). From the presented results we can clearly see the enhancement of the TL signal by organic layers of octane [k=0.128 Wm^{-1}K^{-1}, $\partial n/\partial T$=-4.7×10^{-4} K^{-1} (Table 3)], which is 4.7 and 8.5 times for the two- and three-layer systems compared to that in a standard 100 μm cell, respectively. This is in good agreement with the theoretical values of 5.5 and 10.6 times. The discrepancy from the theory and the relatively large error bars in the well experiments (two- and three-layer systems) is believed to arise partly from the effect of the curved interface between sample and organic layers, which slightly changes optical configuration, and from the uncertainty of the sample length determination.

For this ILS excitation, an equivalent excitation power of 1.05 mW at 514.5 nm was already estimated in the "**Power meter**" part in section 3.1. After comparing the sensitivity of the three-layer ILS-excited TLM and the laser-excited TLM (single-layer) at the same power of 1.05 mW, we can find that the former is about 2 times higher. However, the noise (especially 1/f noise of the detector) of ILS-excited TLM at low frequencies is higher than in the case of laser-excited TLM, which can be operated at high frequencies. This is because the pump laser

beam can be focused to ~1 μm at which the TL signal will not decrease much by the reduced irradiation time at high frequencies (less than 2 times decrease in TL signal at 1 kHz compared to that at 5 Hz). This is not the case for ILS-excited TLM with pump beam radius of 100 μm, at which the TL signal at 1 kHz would be over 100 times lower than that at 5 Hz. Therefore, ILS-excited TLM is performed at low modulation frequencies which result in higher $1/f$ noise of the detector. In the described TLM systems, three times standard deviation (3σ) of TL signals of the blank (deionized water) is about 3.9 μV in ILS-excited TLM at 5 Hz and 0.3 μV in laser-excited TLM at 1.01 kHz. The LOD for 100-μm ferroin solution is calculated to be 1.3×10^{-6} M (1.45×10^{-4} AU) without signal-enhancement layers or 1.95×10^{-7} M (2.18×10^{-5} AU) with signal-enhancement layers at P=1.05 mW and f=5 Hz. If the sample is in organic solution, the LOD could go down to ~10^{-6} AU even without signal-enhancement layers.

Although this is still 6 times higher than the LOD of the laser-excited TLM used in this work, it compares favorably with the LOD reported for microchannel assisted TLM in Ref. 131, where LOD = 2×10^{-5} AU was achieved with the excitation power of 42 mW as opposed to 1.05 mW used in this work. Furthermore the sample in Ref. 131 was dissolved in methanol and not in water as the ferroin sample in experiments described above, thus contributing to 13 times higher TLS enhancement factor. In a practical experiment, by using excitation power of 10 mW such as in the Tunable Illuminator (OBB corp.) for a 10-nm bandwidth, the LOD of the ILS-excited TLM is expected to reach 2.18×10^{-6} AU, which is sufficiently low for sensitive routine analysis.

4.3.4 Other factors influencing the TL signal

In addition, there are some other factors influencing the TL signal, such as the shape of the sample cell or its orientation relative to the aligned pump or probe beams, the flow of sample, the lateral size of the sample cell relative to the size of the probe beam in the sample.

These additional effects on the TL signal may come from:

(1) Photodeflection signal when the sample cell is titled or the sample cell is not rectangular. This may happen when the sample length is large (such as ~mm), and/or the tilted angle is large, especially when the alignment of the two beams is not perfect. This will cause that the central axis of the probe beam moves out of the center of the pinhole, as shown in Fig. 73. In this figure, the black curve represents the intensity profile of the probe beam in the detection plane before excitation in a modulation cycle, while the red curves denote the intensity profiles after excitation. The arrows mean the probe beam intensity change in the center of the detection plane. In experiment, this effect can be suppressed by using less tilted sample cell, better optical alignment and a relatively large pinhole.
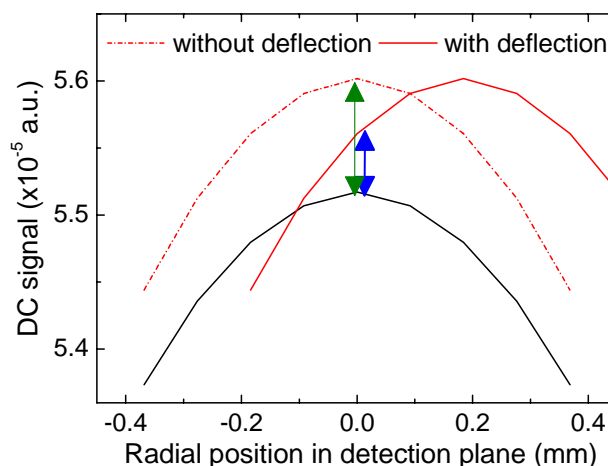
Figure 73: Schematic representation of the probe beam's shift away from the initial position due to photothermal deflection.

(2) The influence of the flow. In the ILS-excited TLM working at low frequency, the temporal response is on 0.1 s timescale. If the system is used in flowing samples, the flow velocity can not be very high. In Fig. 74, temperature profiles for different flow velocities are shown. At v_x=1 cm/s, the maximum temperature shifts about $1.5a_e$ along the direction of the flow. Thus in experiment, it is better to limit the flow velocity to less than 1 cm/s, especially for those cases using signal enhancement layers because the liquid flow will reduce the portion of heat diffusing to the top/bottom layers. However, this relatively low signal response (0.1~1 s) and low flow velocity would be not fast enough to enable on-line detection of analytes in liquid flows in such as HPLC, CE, IC and FIA, where the flow rate is usually about 1 mL/min, corresponding to 1 m/s in the microchannel of our microchip. Therefore, if we want to use the TLM in these systems, a higher modulation frequency should be used at the cost of much lower sensitivity.
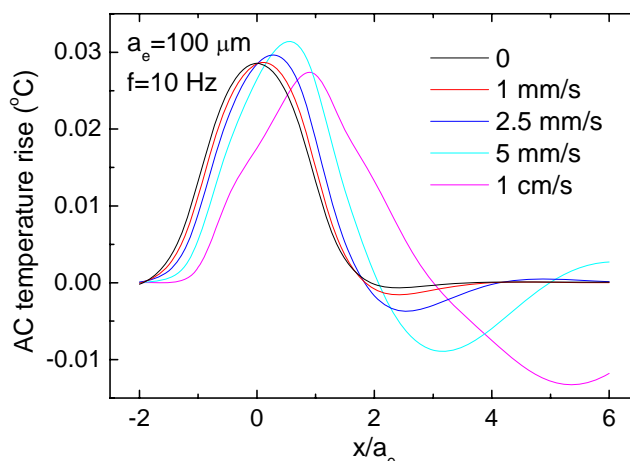
Figure 74: Temperature distributions for flow velocities of v_x=0, 1 mm/s, 2.5 mm/s, 5 mm/s and 1 cm/s, under top-hat beam excitation at a_e=100 μm, f=10 Hz.

(3) Interference of the cell boundary with the propagation of the probe beam. To assure that the propagation of the probe beam is not interfered by the boundary, for the size of the probe beam in the sample under the optimal detection scheme, the diameter of the sample cell is suggested to be larger than 500 μm.

4.4 Performance comparison between the laser- and ILS-excited TLMs, and conventional TLS

To make a comparison, the performances of the three TLS systems used in this work both in static mode (SM) and flowing mode (FM) are summarized in Table 5.

Table 5: Comparison between the ILS- and laser-excited TLMs, and conventional TLS.

Type	Applicable sample length	Sensitivity (ferroin in water)	Noise in DW (S.D.)	LOD (ferroin in water) (3σ criteria)	Comments (advantages, disadvantages, application fields)
Laser-excited TLM	<500 μm	SM: 11 V/M (l=100 μm) or 19 V/M (l=300 μm). f=1.01 kHz, P=4 mW, S_{dc}=0.16 V	0.032 μV at d_{ph}=4 mm	8.7×10^{-9} M (9.57×10^{-7} AU) (l=100 μm) or 5.04×10^{-9} M (1.66×10^{-6} AU) (l=300 μm)	Advantages: high sensitivity and temporal resolution (~ms), applicable to both batch-mode and flow-mode detection of sample in micro space.
		FM: v_x=5 cm/s, 7 V/M (l=100 μm), f=1.01 kHz, P=4 mW, S_{dc}=0.16 V	0.75 μV at d_{ph}=4 mm	3.2×10^{-7} M (3.52×10^{-5} AU) (l=100 μm)	Disadvantages: limited laser lines available for excitation, potential photodegradation of the sample under high power excitation.
ILS-excited TLM	<2.5 mm	SM (one-layer): 8 V/M for l=500 μm. f=5 Hz, P=1 mW, S_{dc}=1 V	1.3 μV at d_{ph}=1 mm	4.87×10^{-7} M (2.4×10^{-4} AU) (l=500 μm)	Advantages: broad-band and low-cost detection in sample cell with relatively large sample length in static or low flow-rate medium.
		SM (three-layer): 24 V/M for l=100 μm. f=5 Hz, P=1 mW, S_{dc}=1 V	1.3 μV at d_{ph}=1 mm	1.95×10^{-7} M (2.18×10^{-5} AU) (l=100 μm)	Disadvantages: inadequate sensitivity for some applications due to low pump power; susceptible to noises; slow temporal response (~0.1 s).
Conventional TLS	~1mm—~1cm	SM: 560 V/M (l=1 cm). f=29 Hz, P=4 mW, S_{dc}=0.16 V	0.4 μV at d_{ph}=4 mm	2×10^{-9} M (2.2×10^{-5} AU) (l=1 cm)	Advantages: high sensitivity, applicable to both batch-mode and flow-mode detection.
		FM: 450 V/M (l=1 cm). f=29 Hz, P=4 mW, S_{dc}=0.16 V	0.8 μV at d_{ph}=4 mm	5×10^{-9} M (5.5×10^{-5} AU) (l=1 cm)	Disadvantages: limited laser lines available for excitation, large sample/reagent consumption.

(1) DW: deionized water; S.D.: standard deviation;

(2) LOD is calculated at the given systematical parameters (power, frequency, sample length, pump laser, sample and detector). Change of one of these parameters may change the LOD.

In addition, some comments should be added:

(1) In laser-excited TLM or conventional TLS, the optimum a_{e0} is determined by Eq. (90), and the probe beam waist radius is suggested as follows: if $l < z_{ce}$, w_1 can be chosen in the range of $0.5a_{e0}\sim a_{e0}$, otherwise w_1 should approach a_{e0} (such as $0.7a_{e0}\sim a_{e0}$). And then an appropriate OL or focusing lens and beam expander should be chosen to get the w_1 and z_{1opt}. If a low mass LOD is required, the excitation beam should be focused as tightly as possible as long as no negative effects (such as photodegradation) take place. In this case, w_1 would be comparable to or larger than a_{e0}. In ILS-excited TLM with a_{e0} ~100 μm, the probe beam should have both a small w_1 (~25 μm) and a large $|z_1|$ (~6 cm) to maximize the sensitivity. Besides, a proper pinhole should be selected for different TLS setups to obtain a low LOD.

(2) In microfluidic applications, laser-excited TLM is the best choice. Its high temporal resolution (～ms) can not only depress the influence of the flow of the medium but also allows real-time monitoring of sample change in the medium. Its capability of micro-space detection makes it possible to detect sample in a volume of pL or less. Besides, the microchannel can be designed to make the flow direction along the pump or probe beam axis to reduce the influence of the flow of the sample.

(3) In batch-mode or low flow-rate applications, ILS-excited TLM may be a choice. Its broad-band detection makes it possible to perform spectroscopic characterization of a sample or to realize specific detection of an analyte of interest. In flowing mode, the time response of the TLM system should be considered when choosing the flow rate. In addition, for the sample in organic solution or in a sample cell with relatively long path length ($l \sim$ mm), the ILS-excited TLM can be applied directly for detection; while for the aqueous sample with short path length ($l \sim 100$ μm), two water-immiscible layers (the top and bottom layers) with high $\partial n/\partial T$ could be used to enhance the sensitivity. To facilitate the measurement with signal-enhancement layer, a special fluidic channel should be designed to accommodate the three layers especially when the top/bottom layers are liquids. If a transparent solid material with high $\partial n/\partial T$ can be found, the inner wall around the detection point can use this material. One possible kind of this material is linear polysiloxane, whose $\partial n/\partial T$ is in the range of -3.5×10^{-4} ~ -5×10^{-4} K^{-1} [172].

5 CONCLUSIONS

In this dissertation, thermal lens spectrometry in micro space was investigated theoretically and experimentally to promote its wider application in microfluidics and microchip chemistry for environmental analysis.

Theoretically, temperature distributions within a sample in micro space were given for the first time by including experimental parameters which were not considered or were oversimplified in previous theories, and were described herein for excitation by a cw modulated laser (with Gaussian intensity profile) and by an ILS (with top-hat intensity profile). The factors influencing the temperature distribution in micro space include the pump beam divergence, flow of the sample, impacts of the top/bottom layers and of the side walls. The Fresnel diffraction theory was employed to describe the TL signal. Numerical simulations on the temperature and TL signal in micro space brought the following predictions:

(1) There exists an optimum pump beam waist radius for a given sample length for the maximum sensitivity.

(2) In flowing mode, an appropriate beam offset between the pump and probe beams could improve the sensitivity and also assure a linear signal response.

(3) For a micro space with dimensions of such as 200-μm width × 100-μm depth, the top/bottom layers have slight influence on the temperature and TL signal for laser-excited TLM where the pump beam radius is ~1 μm, but a big impact on temperature and TL signal was predicted for ILS-excited TLM where the pump beam radius is ~100 μm. Especially, when the sample is placed in between layers of a material with high $\partial n/\partial T$ and low k, sensitivity enhancement of up to 10 times could be expected. The sidewalls will additionally impact the TL signal when thermal conductivity of the sidewall material is much larger or smaller than that of the sample.

In the experimental part of this research, two TLM systems built in house, namely a laser-excited TLM and an ILS-excited TLM, were tested and used in selected applications. To optimize the systems, various experiments were performed to verify the theory and more importantly, to provide some useful information for maximization of detection sensitivity and lowering of noises. For the laser-excited TLM working at 1.01 kHz, it was found that:

(1) The sensitivity of TLM measurements for a given sample length was increased by optimizing the pump beam waist radius as predicted by theory. For sample length of 100 μm, the TL signal at the optimum pump beam waist radius of 2 μm was 1.36 times higher than the signal at the diffraction-limited radius (commonly used in previous TLMs reported in literature) of 0.7 μm, while the power density in the sample is only 1/10 of that at the diffraction limit. For a finite TL element, appropriate probe beam parameters (with beam waist radius of $0.7a_{e0} \sim a_{e0}$ and beam waist-sample distance z_1 of $15z_R \sim 20z_R$, as opposed to $\sqrt{3}z_R$ which was predicted in previous theories [92] and was indeed accepted by some authors for the case of TLM [13]) were also determined to obtain higher detection sensitivity and good response linearity over a large range (over 2 orders of magnitude) of sample concentrations. The noise in the system was found to be dominated by the shot noise and the optimum pinhole aperture-to-beam size ratio [$d_{ph}/(2w_2)$] was obtained at 0.35 for the best signal-to-noise ratio. At 4 mW pump beam power in the sample, a LOD of 9.6×10^{-7} AU was obtained for only 100 μm thick ferroin solution.

(2) In flowing mode, an appropriate offset between pump and probe beams for a given flow velocity, which can only be determined empirically, can not only improve the sensitivity but also assure a linear signal response. In comparison with static mode, a much higher

noise induced by flow was found when the flow rate was over 10 μL/min [10 μL/min corresponds to 10 mm/s in the microchannel of Fig. 15(c)]. This kind of noise behaves like the noise induced by beam pointing instability and is believed to result from the fluctuation of the sample flow and/or the existence of micro- or nano-bubbles in the fluid. The noise was found to be dominated by the flow-induced noise at relatively small $d_{ph}/(2w_2)$ (such as below 1) and by shot noise when $d_{ph}/(2w_2)$ was larger than 1.2. The pinhole aperture-to-beam size ratio can be chosen between 0.1 and 0.4 for high signal-to-noise ratios. At 4 mW pump beam power in the sample, a LOD of 3.5×10^{-5} AU for 100 μm thick ferroin solution was achieved at flow velocity of 52 mm/s. This LOD is about 27 times higher than a calculated LOD of 1.3×10^{-6} AU for the experimental conditions used in this work (i.e. for 100 μm thick aqueous sample at 4 mW) from the original value of 3.5×10^{-8} AU reported in literature [146], which is actually given for a 200-μm thick sample in 80% methanol and 20% deionized water at 28 mW pump beam power. This large difference in LOD can be attributed to the much greater flow-induced noise compared to that in Ref. 146 where the relative standard deviation (RSD) of the TL baseline signal is 1.4×10^{-7}, which is comparable to the value of 2×10^{-7} achieved in this work for the static mode measurement. This is much smaller than the RSD value of 4.6×10^{-6} observed for flowing mode measurements in this work. Since the factors influencing the signal RSD such as the power stability of the probe beam, are the same in static and flow conditions, higher RSD and the related LOD can only be attributed to the much greater flow-induced noise at high flow velocities (such as the above mentioned 52 mm/s). In Ref. 146, a flow cell with much larger dimensions (~mm, with flow velocity of 10 mm/s or less, in comparison to the above mentioned 52 mm/s in a 200 μm×100 μm U-shaped channel shown in Fig. 15(c) used in this work) and a dual-piston pump (in comparison to the gravity-driven pump in this work) were used and therefore a more stable, homogeneous and slow flow was assured there. It is expected that the noise can be further decreased if a more stable fluid pump (such as a pressure pump), a microchannel with larger lateral dimension (corresponding to less flow velocity in microchannel at the same flow rate), a degrasser for degassing the solution and a more stable probe laser (driven by a regulated power supply separately from high-power electrical supplies for the argon ion laser as was the case in this work) are used.

(3) As a practical application, a microfluidic-FIA-TLM system was employed to measure Cr(VI). Though the LOD is not as low as that in conventional FIA-TLS setup, the detection on microchip largely reduced the reaction time compared to spectrophotometric detection and the consumption of sample and reagent, and eliminated the necessity of adding solvents to the sample to match the physical properties of the carrier as was required in FIA-TLS.

For the ILS-excited TLM working at 5 Hz, its optical configuration and sample cell configuration were optimized for higher sensitivity. It was found that:

(1) The dominating noise in the system was found to be flicker noise and the optimum pinhole aperture-to-beam size ratio [$d_{ph}/(2w_2)$] was obtained at 0.05 for the best signal-to-noise ratio. For the ILS the theoretically predicted distance between the probe beam waist and the sample was experimentally confirmed. At the pump beam radius of 107 μm in the sample and given probe beam parameters (w_1=25 μm, z_2=50 cm), this optimal distance was found at z_1= -5 cm, which is in good agreement with the theoretical value z_1= -19z_R. This is in clear contrast with -√3z_R, which was predicted in theories for conventional TLS [92]). For the given case the probe beam size in the sample (w_s) reaches 400 μm. According to the theoretical calculation given in section 4.3.1.3 the probe beam waist radius should be smaller than 2 times of the sample cell radius to avoid interference with

the probe beam by the sample cell boundary. Accordingly for the given case, the diameter of the sample cell should be larger than 1.6 mm. By using a smaller probe beam size in the sample which can be obtained at z_1=-0.55 cm (w_1=25 μm, the probe beam radius in the sample is 50 μm), this ILS-excited TLM could also be applied on the microchip with 200 μm width of the microchannel at the cost of sacrificing the detection sensitivity about 10 times.

(2) Materials with high $\partial n/\partial T$ and low k were used in a three-layer system to enhance the detection sensitivity up to 10 times. The LOD for 100-μm thick ferroin solution was obtained as 1.45×10^{-4} AU without signal-enhancement layers or 2.2×10^{-5} AU with signal-enhancement layers of n-octane at P=1.05 mW. This LOD compares favorably with the LOD of 2×10^{-5} AU reported for microchannel assisted TLM in Ref. 131 at excitation power of 42 mW as opposed to 1.05 mW used in this work. Furthermore the sample in Ref. 131 was dissolved in methanol and not in water as the ferroin sample in experiments described in this work, thus contributing to 13 times higher TLS enhancement factor. If the sample used in this work is in organic solution, the LOD could be reduced down to $\sim 10^{-6}$ AU even without signal-enhancement layers.

The laser-excited TLM coupled with microfluidic devices is expected to find new applications in cases where sensitive, rapid and high throughput detection of various analytes is required, while the ILS-excited TLM in microwells or microchannels is expected to be utilized where the priority is cost-effective and specific detection of toxic compounds.

6   OUTLOOK AND PROSPECTS

It has been demonstrated in this doctoral dissertation and previously by other investigators that TLM techniques can realize a sensitive, fast and specific detection of analytes in micro volume. However, these techniques still don't reach maturity and they have disadvantages and defects, such as the relatively high noise in flowing medium, lack of automation in adjustment of optical configuration and in measurements, lack of a high-power ILS and a monochromator to realize spectral scanning measurement in ILS-excited TLM, and only a few practical applications. Therefore, more researches on TLM need to be performed to further improve the selectivity and detection limit and to make it easier to operate in practical applications. Some possible improvements which could be made in future research are proposed below.

From the point of view of instrumentation, further progress could be made: (1) different pump sources (pulsed lasers, quasi-continuous high repetition laser, doped fiber lasers, LED) which could be introduced into TLM to meet specific detection requirements; (2) employing more automatic and powerful pressure pumps to drive the liquid flow in the channel which could not only facilitate the operation of the system but also decrease the flow-induced noises and then further decrease the detection limit; (3) coupling TLM into a more powerful microchip to realize the so-called lab-on-a-chip, on which different bioanalytical assays or chemical processes could be monitored, or into chromatographic techniques to realize highly sensitive and specific detection of analytes; (4) miniaturization of the TLM system by using more compact and automatic optical or mechanical elements such as optical fibres, motorized stages.

From the point of view of application, more practical measurements can be made: (1) the TLM should be used for the analysis of real samples, which frequently include quite complex matrices, and for the determination of new emerging pollutants in the environment, such as pharmaceuticals, plasticizers and allergens in foodstuffs. For these purposes, (photo)thermal control and acceleration of enzymatic reactions on a microchip, integrated immunoassays on the solid bead surface, and chemi-functional membranes on microchips, as well as glass-substrate microelectrode-microchannel chips could be utilized; (2) detecting single particle or molecule in cells could be another orientation of TLS detection, which would make the TLM applicable to extended nano fluidic systems [173]; (3) equally important is applying the system to the investigation of various phenomena, which could not be studied until now, e.g. diffusion in micro space that needs verification of theoretical predictions that differ from those for macrofluidic systems.

We believe that through further development of TLM and related instrumentations, the microscopic TLS could be capable of analyzing samples with complex matrices in microchips or for high throughput detection of analytes in miniaturized microtiter plates, and furthermore, it can be applied as a powerful detector in μ-TAS, which will be very promising for the future development in the field of analytical chemistry.

7 REFERENCES

1. Monitoring of pesticides residue in products of plant origin in the European Union, Norway, Iceland, and Liechtenstein, 2004 report, 2006, European commission, 72p.

2. Q. X. Li, B. D. Hammock, J. N. Seiber, "Development of an enzyme-linked immunosorbent assay for the herbicide bentazon," *J. Agric. Food Chem.* **39**, 1537-1544 (1991).

3. A. M. Branum, S. L. Lukacs, "Food allergy among U.S. children: trends in prevalence and hospitalizations," *US-NCHS* **10**, 1-7 (2008).

4. A. Kuroda, T. Nakashima, K. Yamaguchi and T. Oda, "Isolation and characterization of light-dependent hemolytic cytotoxin from harmful red tide phytoplankton *Chattonella marina*," *Comparative Biochemistry and Physiology Part C: Toxicology & Pharmacology* **141**, 297-305 (2005).

5. W. W. Carmichael, S. M. F. O. Azevedo, J. S. An, R. J. R. Molica, E. M. Jochimsen, S. Lau, K. L. Rinehart, G. R. Shaw, and G. K. Eaglesham, "Human fatalities from cyanobacteria: chemical and biological evidence for cyanotoxins," *Environmental Health Perspectives*. **109,** 663-668 (2001).

6. Heavy metals in waste-final report, European Commission DG ENV. E3, Feb 2002. http://ec.europa.eu/environment/waste/studies/pdf/heavy_metalsreport.pdf

7. A. Braithwaite and F.J. Smith, *Chromatographic method*s, Kluwer Academic Publishers, Dordrecht, Netherlands, 1999.

8. H. Whatley, "Basic principles and modes of capillary electrophoresis," in *Clinical and Forensic Applications of Capillary Electrophoresis*, edited by: J. R. Petersen and A. A. Mohammad, Humana Press Inc., Totowa, NJ, 2001.

9. J. M. V. Emon (Ed.), *Immunoassay and other bioanalytical techniques*, CRC Press, 2006.

10. A. Boškin, The application of high sensitivity laser methods for detection of organophosphorus pesticides and cholinesterase activity, PhD thesis, University of Nova Gorica, Nova Gorica, Slovenia, 2008.

11. B. Xiong, W. Wang, X. Miao, L. Liu, L. Wang, X. Zhou, J. Hu, "Simultaneous laser-induced fluorescence, coaxial thermal lens spectroscopy and retro-reflected beam interference detection for capillary electrophoresis," *Talanta* **88**, 168-174 (2012).

12. V. S. Dudko, A. P. Smirnova, M. A. Proskurnin, A. Hibara, T. Kitamori, "Thermal lens detection in microfluidic chips," *Russian Journal of General Chemistry* **82**, 2146-2153 (2012).

13. T. Kitamori, M. Tokeshi, A. Hibara, K. Sato, "Thermal lens microscopy and microchip chemistry," *Anal. Chem.* **76**, 52A-60A (2004).

14. V. K. Karamfilov, T. W. Fileman, K. M. Evans, R. F. C. Mantoura, "Determination of dimethoate and fenitrothion in estuarine samples by C-18 solid-phase extraction and high-resolution gas-chromatography with nitrogen-phosphorus detection," *Analytica Chimica Acta* **335**, 51-61 (1996).

15. J. Fenoll, P. Hellin, C. M. Martinez, M. Miguel, P. Flores, "Multiresidue method for analysis of pesticides in pepper and tomato by gas chromatography with nitrogen-phosphorus detection," *Food Chemistry* **105**, 711-719 (2007).

16. R. Rial-Otero, E. M. Gaspar, I. Moura, J. L. Capelo, "Chromatographic-based methods for

pesticide determination in honey: An overview," *Talanta* **71**, 503-514 (2007).

17. Y. Tsumura, K. Ujita, Y. Nakamura, Y. Tonogai, Y. Ito, "Simultaneous determination of aldicarb, ethiofencarb, methiocarb and their oxidized metabolites in grains, fruits and vegetables by high performance liquid chromatography," *J. Food Prot.* **58**, 217-222 (1995).

18. L. Monaci, A. J. van Hengel, "Development of a method for the quantification of whey allergen traces in mixed-fruit juices based on liquid chromatography with mass spectrometric detection," *J. Chromatogr. A* **1192**, 113-120 (2008).

19. C. Cordero, C. Bicchi, D. Joulain, P. Rubiolo, "Identification, quantitation and method validation for the analysis of suspected allergens in fragrances by comprehensive two-dimensional gas chromatography coupled with quadrupole mass spectrometry and with flame ionization detection," *J. Chromatogr. A* **1150**, 37-49 (2007).

20. J. L. Santos, I. Aparicio, E. Alonso, M. Callejón, "Simultaneous determination of pharmaceutically active compounds in wastewater samples by solid phase extraction and high-performance liquid chromatography with diode array and fluorescence detectors," *Analytica Chimica Acta* **550**, 116-122 (2005).

21. M. J. Gómeza, M. Petrović, A. R. Fernández-Alba, D. Barceló, "Determination of pharmaceuticals of various therapeutic classes by solid-phase extraction and liquid chromatography–tandem mass spectrometry analysis in hospital effluent wastewaters," *J. Chromatogr. A* **1114**, 224-233 (2006).

22. L. Gámiz-Gracia, A. M. García-Campaña, J. F. Huertas-Pérez and F. J. Lara, "Chemiluminescence detection in liquid chromatography: Applications to clinical, pharmaceutical, environmental and food analysis—A review," *Analytica Chimica Acta* **640**, 7-28 (2009).

23. Z. Spacil, J. Folbrova, N. Megoulas, P. Solich, M. Koupparis, "Simultaneous liquid chromatographic determination of metals and organic compounds in pharmaceutical and food-supplement formulations using evaporative light scattering detection," *Analytica Chimica Acta* **583**, 239-245 (2007).

24. A. Crecelius, M. R. Clench, D. S. Richards, "TLC-MALDI in pharmaceutical analysis," *Current Trends in Mass Spectrometry* **19**(5S), 28-34 (2002).

25. C. Hao, X. Zhao, P. Yang, "GC-MS and HPLC-MS analysis of bioactive pharmaceuticals and personal-care products in environmental matrices," *Trends in Analytical Chemistry* **26**, 569-580 (2007).

26. F. E. Ahmed, "Analyses of pesticides and their metabolites in foods and drinks," *Trends in Analytical Chemistry*, **20**, 649-661 (2001).

27. M. D. Hernando, I. Ferrer, A. Agüera, A. R. Fernandez-Alba, "Evaluation of pesticides in wastewaters. A combined (chemical and biological) analytical approach," *The Handbook of Environmental Chemistry* **5**, 207-209 (2005).

28. J. W. Jorgenson, K. D. Lukacs, "Zone electrophoresis in open-tubular glass capillaries," *Anal. Chem.* **53**, 1298-1302 (1981).

29. M. C. Carneiro, L. Puignou, M. T. Galceran, "Comparison of silica and porous graphitic carbon as solid-phase extraction materials for the analysis of cationic herbicides in water by liquid chromatography and capillary electrophoresis," *Analytica Chimica Acta* **408**, 263-269 (2000).

30. A. J. García, Guillermina Font, Yolanda Picó, "Quantitative analysis of six pesticides in fruits by capillary electrophoresis-electrospray-mass spectrometry," *Electrophoresis* **26**, 1550-1561 (2005).

31. N. Gasilova, A. Gassner, H. Girault, "Analysis of major milk whey proteins by immunoaffinity capillary electrophoresis coupled with MALDI-MS," *Electrophoresis* **33**, 2390-2398 (2012).

32. S. E. Gibbons, C. Wang, Y. Ma, "Determination of pharmaceutical and personal care products in wastewater by capillary electrophoresis with UV detection," *Talanta* **84**, 1163-1168 (2011).

33. N. Quek, W. Law, H. Lau, J. Zhao, P. Hauser, S. Li, "Determination of pharmaceuticals classified as emerging pollutants using capillary electrophoresis with capacitively coupled contactless conductivity detection," *Electrophoresis* **29**, 3701-3709 (2008).

34. B. Bucur, D. Fournier, A. Danet, J. Marty, "Biosensors based on highly sensitive acetylcholinesterases for enhanced carbamate insecticides detection," *Analytica Chimica Acta* **562**, 115–121 (2006).

35. E. Mauriz, A. Calle, J. J. Manclus, A. Montoya, A. M. Escuela, J. R. Sendra, L. M. Lechuga, "Single and multi-analyte surface plasmon resonance assays for simultaneous detection of cholinesterase inhibiting pesticides," *Sensors and Actuators B* **118**, 399-407 (2006).

36. L. Negroni, H. Bernard, G. Clement, J. M. Chatel, P. Brune, Y. Frobert, J. M. Wal, J. Grassi, "Two-site enzyme immunometric assays for determination of native and denatured β-lactoglobulin," *Journal of Immunological Methods* **220**, 25–37 (1998).

37. S. Jin, Z. Xu, J. Chen, X. Liang, Y. Wu, X. Qian, "Determination of organophosphate and carbamate pesticides based on enzyme inhibition using a pH-sensitive fluorescence probe," *Analytica Chimica Acta* **523**, 117-123 (2004).

38. B. Kuswandi, C. I. Fikriyah, A. A. Gani, "An optical fiber biosensor for chlorpyrifos using a single sol-gel film containing acetylcholinesterase and bromothymol blue," *Talanta* **74**, 613-618 (2008).

39. L. Pogačnik, M. Franko, "Detection of organophosphate and carbamate pesticides in vegetable samples by a photothermal biosensor," *Biosensors and Bioelectronics* **18**, 1-9 (2003).

40. M. Bavcon Kralj, P. Trebse, M. Franko, "Applications of bioanalytical techniques in evaluating advanced oxidation processes in pesticide degradation," *Trends in Analytical Chemistry* **26**, 1020-1031 (2007).

41. Y. Lee, R. G. Maus, B. W. Smith, and J. D. Winefordner, "Laser-induced fluorescence detection of a single molecule in a capillary," *Anal. Chem.* **66**, 4142-4149 (1994).

42. J. Z. Zhang, "Enhanced sensitivity in flow injection analysis using a long pathlength liquid waveguide capillary flow cell for spectrophotometric detection," *Analytical Sciences* **22**, 57-60 (2006).

43. L. Krockel, G. Schwotzer, H. Lehmann, T. Wieduwilt, "Spectral optical monitoring of nitrate in inland and seawater with miniaturized optical components," *Water Research* **45**, 1423-1431 (2011).

44. A. Gaspar, I. Bacsi, E. F. Garcia, M. Braun, F. A. Gomez, "Application of external micro-spectrophotometric detection to improve sensitivity on microchips," *Anal Bioanal Chem* **395**, 473-478 (2009).

45. Fu-Ren F. Fan and Allen J. Bard, "Electrochemical detection of single molecules," *Science* **267**, 871-874 (1995).

46. S. Nie and S.R. Emory, "Probing single molecules and single nanoparticles by surface-enhanced Raman scattering," *Science* **275**, 1102-1106 (1997).

47. J. P. Gordon, R. C. C. Leite, R. S. Moore, S. P. S. Porto, J. R. Whinnery, "Long-transient effects in lasers with inserted liquid samples," *J. Appl. Phys.* **36**, 3-8 (1965).

48. S. E. Bialkowski, *Photothermal Spectroscopy Methods for Chemical Analysis*, (Chemical Analysis, vol. 134, J. D. Winefordner, Ed.), John Whiley & Sons, Inc., New York, 1996.

49. M. Franko, C. D. Tran, "Analytical thermal lens instrumentation," *Rev. Sci. Instrum.* **67**, 1-18 (1996).

50. M. Franko, "Thermal lens spectrometric detection in flow injection analysis and separation techniques," *Appl. Spectrosc. Rev.* **43**, 358-388 (2008).

51. H. C. Fang, R. L. Swoford, The Thermal Lens in Absorption Spectroscopy, in *Ultrasensitive Laser Spectroscopy*, ed. D.S. Kliger, Academic Press, 1983,175-232.

52. N. J. Dovichi, "Thermo-optical spectrophotometries in analytical chemistry," *Crit. Rev. Anal. Chem.* **17**, 357-423 (1987).

53. R. Gupta, Theory of Photothermal Effect in Fluids, in *Photothermal Investigations of Solids and Fluids*, ed. J.A. Sell, Academic Press, New York, 1988, 81-126.

54. J. Harris, Thermal Lens Effect, in *Analytical Applications of Lasers*, ed. E.H. Piepmeier, Wiley Interscience, New York, 1986, 451-554.

55. N. J. Dovichi, J. M. Harris, "Laser induced thermal lens effect for calorimetric trace analysis," *Anal. Chem.* **51**, 728-731 (1979).

56. T.-K.J. Pang, M. D. Morris, "Liquid chromatography detection at the second harmonic of the modulated thermal lens," *Anal. Chem.* **56**, 1467-1469 (1984).

57. W. A. Weimer, N. J. Dovichi, "Time-resolved crossed-beam thermal lens measurement as a nonintrusive probe of flow velocity," *Appl. Opt.* **24**, 2981-2986 (1985).

58. S. J. Sheldon, L. V. Knight, J. M. Thorne, "Laser-induced thermal lens effect: a new theoretical model," *Appl. Opt.* **21**, 1663-1669 (1982).

59. S. R. Erskine, D. R. Bobbitt, "Obliquely crossed, differential thermal lens measurements under conditions of high background absorbance," *Appl. Spectrosc.* **43**, 668-674 (1989).

60. M. Franko, D. Bicanic, "Differential thermal lens spectroscopy in the infrared," *Israel Journal of Chemistry* **38**, 175-179 (1998).

61. D. M. Plumb, J. M. Harris, "Absorbance measurements in optically inhomogeneous samples using phase-conjugate thermal lens spectroscopy," *Appl. Spectrosc.* **46**, 1346-1353 (1992).

62. M. Xu, C. D. Tran, "Thermal lens-circular dichroism spectropolarimeter," *Appl. Spectrosc.* **44**, 962-966 (1990).

63. M. Qi, X. F. Li, C. Stathakis, N.J. Dovichi, "Capillary electrochromatography with thermo-optical absorbance detection for the analysis of phenylthiohydantoin-amino Acids," *J. Chromatogr. A* **853**, 131-140 (1999).

64. C. D. Tran, V. I. Grishko, "Thermal lens technique for sensitive and nondestructive determination of isotopic purity," *Anal. Biochem.* **218**, 197-203 (1994).

65. C. D. Tran, V. I. Grishko, M. S. Baptista, "Nondestructive and nonintrusive determination of chemical and isotopic purity of solvents by near-infrared thermal lens spectrometry," *Appl. Spectrosc.* **48**, 833-842 (1994).

66. M. Baptista, C. D. Tran, "Near-infrared thermal lens spectrometer based on an erbium-doped fiber amplifier and an acousto-optic tunable filter, and its application in the determination of nucleotides," *Appl. Opt.* **36**, 7059-7065 (1997).

67. C. D. Tran, V. Simianu, "Multiwavelength thermal lens spectrophotometer based on an acousto-optic tunable filter," *Anal. Chem.* **64**, 1419-1425 (1992).

68. B. Divjak, M. Franko, Mi. Novič, "Determination of iron complex matrices by ion chromatography with UV-Vis, thermal lens and amperometric detection using post-column reagents," *J. Chromatogr. A* **829**, 167-174 (1998).

69. M. Šikovec, M. Novič, V. Hudnik, M. Franko, "On-line thermal lens spectrometric detection of Cr(III) and Cr(VI) after separation by ion chromatography," *J. Chromatogr. A* **706**, 121-126 (1995).

70. M. Šikovec, M. Franko, M. Novič, M. Veber, "Effect of organic solvents in the on-line thermal lens spectrometric detection of chromium(III) and chromium(VI) after ion chromatographic separation," *J. Chromatogr. A* **920**, 119-125 (2001).

71. A. Madžgalj, M. L. Baesso, M. Franko, "Flow injection–thermal lens spectrometric determination of hexavalent chromium," *Eur. Phys. J. Special Topics* **153**, 503-506 (2008).

72. M. Šikovec, M. Novič, M. Franko, "Application of thermal lens spectrometric detection to the determination of heavy metals by ion chromatography," *J. Chromatogr. A* **739**, 111-117 (1996).

73. N. Ragozina, S. Heissler, W. Faubel, U. Pyell, "Near-field thermal lens detection at 257 nm as an alternative to absorption spectrometric detection in combination with electromigrative separation techniques," *Anal. Chem.* **74**, 4480-4487 (2002).

74. V. Guzsvány, A. Madžgalj, P. Trebše, F. Gaál, M. Franko, "Determination of some neonicotinoid insecticides by liquid chromatography with thermal lens spectrometric detection," *Environ. Chem. Lett.* **5**, 203-208 (2007).

75. A. Harata, T. Matuda, S. Hirashima, "Ultraviolet-laser excitation microscopic photothermal lens imaging for observing biological cells," *Jpn. J. Appl. Phys.* **46**, 4561-4563 (2007).

76. H. Katae, S. Hirashima, A. Harata, "Direct detection of gradient-eluted non-labeled amino acids using micro-HPLC with ultraviolet thermal lensing," *Journal of Physics: Conference Series* **214**, 012122-1~4 (2010).

77. K. Nakanishi, T. Imasaka, N. Ishibashi, "Thermal lens spectrophotometry of phosphorus using a near-infrared semiconductor laser," *Anal. Chem.* **57**, 1219-1223 (1985).

78. D. Bicanic, M. Franko, J. Gibkes, E. Gerkema, J. P. Favier, H. Jalink, "Applications of photoacoustic and photothermal non-contact methods in the selected areas of environmental and agricultural sciences," in *Progress in Photothermal and Photoacoustic Science and*

Technology, Vol. 3, Life and Earth Sciences, ed. A. Mandelis, SPIE-Optical Engineering Press, Bellingham, 131-180, 1996.

79. D. Bicanic, G. Močnik, M. Franko, H. A. G. Niederländer, P. Van de Bovenkamp, J. Cozijnsen, E. Van der Klift, "Separation and direct detection of long chain fatty acids and their methylesters by the nonaqueous reversed phase HPLC and silver ion chromatography, combined with CO laser pumped thermal lens spectrometry," *Instrum. Sci. Tech.* **34**, 129-150 (2006).

80. B. Li, S. Xiong, Y. Zhang, "Fresnel diffraction model for mode-mismatched thermal lens with top-hat beam excitation," *Appl. Phys. B* **80**, 527-534 (2005).

81. A. Chartier, S. Bialkowski, "Photothermal lens spectrometry of homogeneous fluids with incoherent white-light excitation using a cylindrical sample cell," *Opt. Eng.* **36**, 303-311 (1997).

82. S. Bialkowski, A. Chartier, "Photothermal spectrometry in small liquid channels," *Analytical Sciences* **17** supplement., i99-i101 (2001).

83. W. Faubel, S. Heissler, U. Pyell, and N. Ragozina, "Photothermal trace detection in capillary electrophoresis for biomedical diagnostics and toxic materials," *Rev. Sci. Instrum.* **74**, 491-494 (2003).

84. H. B. Kiml, T. Hagino, N. Sasaki, and T. Kitamori, "Ultrasensitive detection of electrochemical reactions by thermal lens microscopy for microchip chemistry," 7th lnternational Conference on Miniaturized Chemical and Blochemlcal Analysts Systems, Squaw Valley, Callfornla USA, 817-820 (2003).

85. L. Pogačnik, M. Franko, "Optimisation of FIA system for detection of organophosphorus and carbamate pesticides based on cholinesterase inhibition," *Talanta* **54**, 631-641 (2001).

86. W. A. Weimer, N. J. Dovichi, "Time-resolved thermal lens measurements in flowing samples," *Anal.Chem.* **57**, 2436-2441 (1985).

87. R. Vyas, R. Gupta, "Photothermal lensing spectroscopy in a flowing medium: theory," *Appl. Opt.* **27**, 4701-4711 (1988).

88. W. A. Weimer, N. J. Dovichi, "Optimization of photothermal refraction for flowing liquid samples," *Appl. Spectros.* **39**, 1009-1013 (1985).

89. N. J. Dovichi, J. M. Harris, "Thermal lens calorimetry for flowing samples." *Anal. Chem.* **53**, 689-692 (1981).

90. S. L. Nickolaisen, S. E. Bialkowski, "Pulsed laser thermal lens spectrophotometry for flowing liquid detection." *Anal. Chem.* **58**, 215-220 (1986).

91. S. Chanlon, J. Georges, "Pulsed-laser mode-mismatched crossed-beam thermal lens spectrometry within a small capillary tube: Effect of flow rate and beam offset on the photothermal signal," *Spectrochim. Acta A* **58**, 1607-1613 (2002).

92. S. J. Sheldon, L. V. Knight, J. M. Thorne, "Laser-induced thermal lens effect: a new theoretical model," *Appl. Opt.* **21**, 1663-1669 (1982).

93. J. Shen, R. D. Lowe, R. D. Snook, "A model for cw laser induced mode-mismatched dual-beam thermal lens spectrometry," *Chemical Physics* **165**, 385-396 (1992).

94. M. Franko, C. D. Tran, "Thermal lens technique for sensitive kinetic determinations of fast chemical reactions. Part I. Theory," *Rev. Sci. Instrum.* **62**, 2430-2437 (1991).

95. M. Franko, C. D. Tran, "Thermal lens technique for sensitive kinetic determinations of fast chemical reactions. Part II. Experiment," *Rev. Sci. Instrum.* **62**, 2438-2442 (1991).

96. P. R. B. Pedreira, L. R. Hirsch, J. R. D. Pereira, A. N. Medina, A. C. Bento, and M. L. Baesso, M. C. Rollemberg, M. Franko, J. Shen, "Real-time quantitative investigation of photochemical reaction using thermal lens measurements: Theory and experiment," *J. Appl. Phys.* **100**, 044906-1~7 (2006).

97. A. Harata, N, Yamaguchi, "Photothermal lensing signal enhancement by the transient absorption of photoexcited states in liquid solutions," *Anal. Sci.* **16**, 743-749 (2000).

98. A. Harata, K. Fukushima, Y. Harano, "Magnification in excess of 100-times of the microscopic photothermal lensing signal from solute molecules by two-color excitation with continuous-wave lasers," *Anal. Sci.* **18**, 1367-1373 (2002).

99. J. Georges, "Matrix effects in thermal lens spectrometry: Influence of salts, surfactants, polymers and solvent mixtures," *Spectrochimica Acta Part A* **69**, 1063-1072 (2008)

100. H. Cabrera, E. Sira, K. Rahn, and M. García-Sucre, "A thermal lens model including the Soret effect," *Appl. Phys. Lett.* **94**, 051103-1~3 (2009).

101. A. Marcano O., F. Delima, Y. Markushin, and N. Melikechi, "Determination of linear and nonlinear absorption of metallic colloids using photothermal lens spectrometry," *J. Opt. Soc. Am. B* **28**, 281-287 (2011).

102. J. Georges, N. Arnaud, and L. Parise, "Limitations arising from optical saturation in fluorescence and thermal lens spectrometries using pulsed laser excitation: Application to the determination of the fluorescence quantum yield of Rhodamine 6G," *Appl. Spectrosc.* **50**, 1505-1511 (1996).

103. G. Ramis-Ramos, J. J. Baeza Baeza, E. F. Simó Alfonso, "A model for optical saturation thermal lens spectrometry," *Analytica Chimica Acta* **296**, 107-113 (1994).

104. C. V. Bindhu, S. S. Harilal, V. P. N. Nampoori, C. P. G. Vallabhan, "Investigation of nonlinear absorption and aggregation in aqueous solutions of rhodamine B using thermal lens technique," *PRAMANA-journal of physics* **52**, 435-442 (1999).

105. A. Taouri, H. Derbal, J. M. Nunzi, R. Mountasser, M. Sylla, "Two-photon absorption cross-section measurement by thermal lens and nonlinear transmission methods in organic materials at 532 nm and 1064 nm laser excitations," *Journal of Optoelectronics and Advanced Materials* **11**, 1696-1703 (2009).

106. K. Takeshita, J. Shibato, T. Sameshima, S. Fukunaga, Seiichiro Isobe, Keizo Arihara, Makoto Itoh, "Damage of yeast cells induced by pulsed light irradiation," *International Journal of Food Microbiology* **85**, 151-158 (2003).

107. I. H. Chen, S. W. Chu, C. K. Sun, P. C. Cheng, B. L. Lin, "Wavelength dependent damage in biological multi-photon confocal microscopy: A micro-spectroscopic comparison between femtosecond Ti:sapphire and Cr:forsterite laser sources," *Optical and Quantum Electronics* **34**, 1251-1266 (2002).

108. J. F. Power, "Pulsed mode thermal lens effect detection in the near field via thermally induced probe beam spatial phase modulation: a theory," *Appl. Opt.* **29**, 52-63 (1990).

109. S. R. Erskine, D. R. Bobbitt, "Theoretical and experimental investigation of the relationship between aperture dimension and signal-to-noise optimization in thermal lens spectroscopy," *Applied Spectroscopy* **42**, 331-335 (1988).

110. M. A. Proskurnin, S. N. Bendrysheva, N. Ragozina, S. Heissler, W. Faubel, and U. Pyell, "Optimization of instrumental parameters of a near-field thermal-lens detector for capillary electrophoresis," *Applied Spectroscopy* **59**, 1470-1479 (2005).

111. M. Šikovec, M. Franko, M. Novič, M. Veber, "Effect of organic solvents in the on-line thermal lens spectrometric detection of chromium(III) and chromium(VI) after ion chromatographic separation," *J. Chrom. A* **920**, 119-125 (2001).

112. M. Franko, "Bioanalytical applications of thermal lens spectrometry," in Thermal Wave Physics and Related Photothermal Techniques: Basic Principles and Recent Developments, edited by E. M. Moares, Transworld Research Network, Kerala, India, 2009.

113. C. D. Tran, S. Challa, M. Franko, "Ionic liquids as an attractive alternative solvent for thermal lens measurements," *Anal. Chem.* **77**, 7442-7447 (2005).

114. C. D. Tran, T. A. Van Fleet, "Micellar induced simultaneous enhancement of fluorescence and thermal lensing," *Anal. Chem.* **60**, 2478-2482 (1988).

115. C. D. Tran, "Simultaneous enhancement of fluorescence and thermal lensing by reversed micelles," *Anal. Chem.* **60**, 182-185 (1988).

116. C. D. Tran, W. Zhang, "Thermal lensing detection of lanthanide ions by solvent extraction using crown ethers," *Anal. Chem.* **62**, 830-834 (1990).

117. M. Franko, C. D. Tran, "Water as a unique medium for thermal lens measurements," *Anal. Chem.* **61**, 1660-1666 (1989).

118. V. I. Grishko, C. D. Tran, and W. W. Duley, "Enhancement of the thermal lens signal induced by sample matrix absorption of the probe laser beam," *Appl. Opt.* **41**, 5814-5822 (2002).

119. D. A. Nedosekin, W. Faubel, M. A. Proskurnin, U. Pyell, "Sensitivity enhancement of thermal-lens spectrometry using laser-induced precipitation," *Anal. Sci.* **25**, 611-616 (2009).

120. M. J. Weber, *Handbook of Optical Materials*, CRC, Boca Raton, FL, 2003.

121. S. Luterotti, M. Šikovec, D. Bicanic, "Ultrasensitive determination of trans-β-carotene in rat and beef livers by means of high-performance liquid chromatography coupled with thermal lens detection," *Talanta* **53**, 103-113 (2000).

122. V. Guzsvány, A. Madžgalj, P. Trebše, F. Gaál, M. Franko, "Determination of some neonicotinoid insecticides by liquid chromatography with thermal lens spectrometric detection," *Environ. Chem. Lett.* **5**, 203-208 (2007).

123. I. Mejač, A. Madžgalj, V. Guszvany, F. Gaal, P. Trebše, M.Franko, "HPLC determination of neonicotinoid insecticides in honey and pollen," In 12th International Symposium on Separation Sciences, M. Strlič (ed.), Slovene Chemical Society: Lipica, Slovenia, pp. 160-162 (2006).

124. B. S. Seidel, W. Faubel, "Fiber optic modified thermal lens detector system for the determination of amino acids," *J. Chrom. A* **817**, 223-226 (1998).

125. N. Y. Ragozina, M. Pütz, S. Heissler, W. Faubel, U. Pyell, "Quantification of etoposide and etoposide phosphate in human plasma by micellar electrokinetic chromatography and near field thermal lens detection," *Anal. Chem.* **76**, 3804-3809 (2004).

126. R. A. Leach, J. M. Harris, "Real-time thermal lens absorption measurements with application to flow-injection systems," *Anal. Chim. Acta* **164**, 91-101 (1984).

127. L. Pogačnik, M. Franko, "Determination of organophosphate and carbamate pesticides in spiked samples of tap water and fruit juices by a biosensor with photothermal detection," *Biosens. Bioelectron.* **14**, 569-578 (1999).

128. M. Bavcon-Kralj, P. Trebše, M. Franko, "Applications of bioanalytical techniques in evaluating advanced oxidation processes in pesticide degradation," *Trends Anal. Chem.* **26**, 1020-1031 (2007).

129. M. Harada, K. Iwamoto, T. Kitamori, T. Sawada, "Photothermal microscopy with excitation and probe beams coaxial under the microscope and its application to microparticle analysis," *Anal. Chem.* **65**, 2938-2940 (1993).

130. S. Hiki, K. Mawatari, A. Hibara, M. Tokeshi, T. Kitamori, "UV excitation thermal lens microscope for sensitive and nonlabeled detection of nonfluorescent molecules," *Anal. Chem.* **78**, 2859-2863 (2006).

131. E. Tamaki, A. Hibara, M. Tokeshi, T. Kitamori, "Microchannel-assisted thermal-lens spectrometry for microchip analysis," *J. Chromatogr. A* **987**, 197-204 (2003).

132. E. Tamaki, A. Hibara, M. Tokeshi, T. Kitamori, "Tunable thermal lens spectrometry utilizing microchannel-assisted thermal lens spectrometry," *Lab Chip* **5**, 129-131 (2005).

133. A. Hibara, T. Saito, H. B. Kim, M. Tokeshi, T. Ooi, M. Nakao, T. Kitamori, "Nanochannels on a fused-silica microchip and liquid properties investigation by time-resolved fluorescence measurements," *Anal. Chem.* **74**, 6170-6176 (2002).

134. M. Yamauchi, M. Tokeshi, J. Yamaguchi, T. Fukuzawa, A. Hattori, A. Hibara, T. Kitamori, "Miniaturized thermal lens and fluorescence detection system for microchemical chips," *J. Chromatogr. A* **1106**, 89-93 (2006).

135. H. Shimizu, K. Mawatari, T. Kitamori, "Development of a differential interference contrast thermal lens microscope for sensitive individual nanoparticle detection in liquid," *Anal. Chem.* **81**, 9802-9806 (2009).

136. http://www.i-mt.co.jp/

137. M. Tokeshi, T. Minagawa, T. Kitamori, "Integration of a microextraction system on a glass chip: Ion-pair solvent extraction of Fe(II) with 4,7-diphenyl-1,10 phenanthrolinedisulfonic acid and tri-n-octylmethylammonium chloride," *Anal. Chem.* **72**, 1711-1714 (2000).

138. K. Sato, M. Tokeshi, T. Odake, H. Kimura, T. Ooi, M. Nakao, T. Kitamori, "Integration of an immunosorbent assay system: analysis of secretory human immunoglobulin A on polystyrene beads in a microchip," *Anal. Chem.* **72**, 1144-1147 (2000).

139. http://www.dolomite-microfluidics.com/

140. http://www.microliquid.com/

141. http://www.micronit.com/

142. M. Galloway, W. Stryjewski, A. Henry, S. M. Ford, S. Llopic, R. L. McCarley, S. A. Soper, "Contact conductivity detection in poly(methyl methacrylate)-based microfluidic devices for analysis of mono- and polyanionic molecules," *Anal. Chem.* **74**, 2407-2415 (2002).

143. E. S. Roddy, M. Price, A. G. Ewing, "Continuous monitoring of a restriction enzyme digest of DNA on a microchip with automated capillary sample introduction," *Anal. Chem.* **75**, 3704-3711 (2003).

144. Y. Tachibana, K. Otsuka, S. Terabe, A. Arai, K. Suzuki, S. Nakamura, " Robust and simple interface for microchip electrophoresis–mass spectrometry," *J. Chromatogr. A* **1011**, 181-192 (2003).

145. M. A. Proskurnin, M. N. Slyadnev, M. Tokeshi, T. Kitamori, "Optimisation of thermal lens microscopic measurements in a microchip," *Analytica Chimica Acta* **480**, 79-95 (2003).

146. F. Li, A. A. Kachanov, R. N. Zare, "Detection of separated analytes in subnanoliter volumes using coaxial thermal lensing," *Anal. Chem.* **79**, 5264-5271 (2007).

147. M. Tokeshi, T. Minagawa, K. Uchiyama, A. Hibara, K. Sato, H. Hisamoto, T. Kitamori, "Continuous flow chemical processing on a microchip by combining micro unit operations and a multiphase flow network," *Anal. Chem.* **74**, 1565-1571 (2002).

148. A. Smirnova, K. Mawatari, A. Hibara, M. A. Proskurnin, T. Kitamori, "Micro-multiphase laminar flows for the extraction and detection of carbaryl derivative," *Analytica Chimica Acta* **558**, 69-74 (2006).

149. M. Tokeshi, M. Uchida, A. Hibara, T. Sawada, T. Kitamori, "Determination of subyoctomole amounts of nonfluorescent molecules using a thermal lens microscope: Subsingle-molecule determination," *Anal. Chem.* **73**, 2112-2116 (2001).

150. K. Sato, M. Yamanaka, T. Hagino, M. Tokeshi, H. Kimura, T. Kitamori, "Microchip-based enzyme-linked immunosorbent assay (microELISA) system with thermal lens detection," *Lab Chip* **4**, 570-575 (2004).

151. K. Sato, A. Egami, T. Odake, M. Tokeshi, M. Aihara, T. Kitamori, "Monitoring of intercellular messengers released from neuron networks cultured in a microchip," *J. Chromatogr. A* **1111**, 228-232 (2006).

152. K. Sato, M. Tokeshi, T. Kitamori, T. Sawada, "Integration of flow injection analysis and zeptomole-level detection of the Fe(II)-o-phenanthroline complex," *Anal. Sci.* **15**, 641-645 (1999).

153. H. M. Sorouraddin, A. Hibara, M. A. Proskrunin, T. Kitamori, "Integrated FIA for the determination of ascorbic acid and dehydroascorbic acid in a microfabricated glass-channel by thermal-lens microscopy," *Anal. Sci.* **16**, 1033-1037 (2000).

154. H. M. Sorouraddin, A. Hibara, T. Kitamori, "Use of a thermal lens microscope in integrated catecholamine determination on a microchip," *Fresen. J. Anal. Chem.* **371**, 91-96 (2001).

155. S. Takayama, J. Chang, D. Huh, X. Zhu, B. Cho, G. D. Smith, Microfluidic gravity pump with constant flow rate, Patent No. US007704728B2, 2010.

156. D. A. Skoog, F. J. Holler and S. R. Crouch, *Principles of instrumental analysis*, six edition, Thomson Brooks/Cole, Belmont, CA, USA, p34.

157. T. Shigematsu, S. Gohda, H. Yamazaki, Y. Nishikawa, "Spectrophotometric determination of Chromium (III) and Chromium (VI) in sea water," *Bull. Inst. Chem. Res.* 55, 429-440 (1977).

158. M. A. Proskurnin, S. N. Bendrysheva, N. Ragozina, S. Heissler, W. Faubel, U. Pyell, "Optimization of instrumental parameters of a near-field thermal-lens detector for capillary electrophoresis," *Appl. Spectrosc.* **59**, 1470-1479 (2005).

159. J. Alda, "Laser and Gaussian beam propagation and transformation" in *Encyclopedia of Optical Engineering*, Marcel Dekker, Inc., New York, 2003.

160. Q. Yao, *Optics Tutorial*, Edition 3, Higher Education Press, Beijing, 2002.

161. S. E. Bialkowski, "Pulsed laser thermal lens spectrophotometry of liquid samples using an optical fiber beam guide with interference orthogonal signal processing," *Anal. Chem.* **58**, 1706-1710 (1986).

162. S. E. Bialkowski, *Photothermal spectroscopy methods for chemical analysis*, (Chemical Analysis, vol. 134, J. D. Winefordner, Ed.), John Whiley & Sons, Inc., New York, 1996, p360.

163. R. Anraku, K. Mawatari, M. Tokeshi, M. Nara, T. Asai, A. Hattori, T. Kitamori, "Numerical analysis of thermal lens effect for sensitive detection on microchip," *Electrophor.* **29**, 1895-1901 (2008).

164. Y. Peng, Z. Cheng, Y. Zhang, J. Qiu, "Temperature distributions and thermal deformations of mirror substrates in laser resonators," *Appl. Opt.* **40**, 4824-4830 (2001).

165. http://www.efm.leeds.ac.uk/CIVE/CIVE1400/Section4/laminar_turbulent.htm

166. A. Rose, R. Vyas, R. Gupta, "Pulsed photothermal deflection spectroscopy in a flowing medium: a quantitative investigation," *Appl. Opt.* **25**, 4626-4643 (1986).

167. B. Li, Y. Deng, J. Cheng, "Separation of optical thin film and substrate absorption by obliquely-crossed photothermal deflection: theory," *J. Mod. Optics* **42**, 1093-1107 (1995).

168. M. Soltanolkotabi, M. H. Naderi, "Three dimensional photothermal deflection and thermal lensing in solids: the effect of modulation frequency," *Jpn. J. Appl. Phys.* **43**, 611-620 (2004).

169. M. N. Özisik, *Heat conduction*, 2nd ed., Wiley, 1993, p312-314.

170. A. Madžgalj, M. L. Baesso, M. Franko, "Flow injection thermal lens spectrometric detection of hexavalent chromium," *Eur. Phys. J. Special Topics* **153**, 503-506 (2008).

171. J. Georges, "Advantages and limitations of thermal lens spectrometry over conventional spectrophotometry for absorbance measurements," *Talanta* **48**, 501-509 (1999).

172. K. Su, J. V. DeGroot, Jr., A. W. Norris and P. Y. Lo, "Siloxane materials for optical applications," *Proc. SPIE* **6029**, 60291C-1~8 (2005).

173. K. Mawatari, T. Tsukahara, Y. Sugii and T. Kitamori, "Extended-nano fluidic systems for analytical and chemical technologies," *Nanoscale* **2**, 1588-1595 (2010).